NASA/TM—2003-210803

Analysis of Plasma-Sprayed Thermal Barrier Coatings With Homogeneous and Heterogeneous Bond Coats Under Spatially Uniform Cyclic Thermal Loading

Marek-Jerzy Pindera
University of Virginia, Charlottesville, Virginia

Jacob Aboudi
Tel-Aviv University, Ramat-Aviv, Israel

Steven M. Arnold
Glenn Research Center, Cleveland, Ohio

December 2003

The NASA STI Program Office . . . in Profile

Since its founding, NASA has been dedicated to the advancement of aeronautics and space science. The NASA Scientific and Technical Information (STI) Program Office plays a key part in helping NASA maintain this important role.

The NASA STI Program Office is operated by Langley Research Center, the Lead Center for NASA's scientific and technical information. The NASA STI Program Office provides access to the NASA STI Database, the largest collection of aeronautical and space science STI in the world. The Program Office is also NASA's institutional mechanism for disseminating the results of its research and development activities. These results are published by NASA in the NASA STI Report Series, which includes the following report types:

- TECHNICAL PUBLICATION. Reports of completed research or a major significant phase of research that present the results of NASA programs and include extensive data or theoretical analysis. Includes compilations of significant scientific and technical data and information deemed to be of continuing reference value. NASA's counterpart of peer-reviewed formal professional papers but has less stringent limitations on manuscript length and extent of graphic presentations.

- TECHNICAL MEMORANDUM. Scientific and technical findings that are preliminary or of specialized interest, e.g., quick release reports, working papers, and bibliographies that contain minimal annotation. Does not contain extensive analysis.

- CONTRACTOR REPORT. Scientific and technical findings by NASA-sponsored contractors and grantees.

- CONFERENCE PUBLICATION. Collected papers from scientific and technical conferences, symposia, seminars, or other meetings sponsored or cosponsored by NASA.

- SPECIAL PUBLICATION. Scientific, technical, or historical information from NASA programs, projects, and missions, often concerned with subjects having substantial public interest.

- TECHNICAL TRANSLATION. English-language translations of foreign scientific and technical material pertinent to NASA's mission.

Specialized services that complement the STI Program Office's diverse offerings include creating custom thesauri, building customized databases, organizing and publishing research results . . . even providing videos.

For more information about the NASA STI Program Office, see the following:

- Access the NASA STI Program Home Page at ***http://www.sti.nasa.gov***

- E-mail your question via the Internet to help@sti.nasa.gov

- Fax your question to the NASA Access Help Desk at 301–621–0134

- Telephone the NASA Access Help Desk at 301–621–0390

- Write to:
  NASA Access Help Desk
  NASA Center for AeroSpace Information
  7121 Standard Drive
  Hanover, MD 21076

NASA/TM—2003-210803

Analysis of Plasma-Sprayed Thermal Barrier Coatings With Homogeneous and Heterogeneous Bond Coats Under Spatially Uniform Cyclic Thermal Loading

Marek-Jerzy Pindera
University of Virginia, Charlottesville, Virginia

Jacob Aboudi
Tel-Aviv University, Ramat-Aviv, Israel

Steven M. Arnold
Glenn Research Center, Cleveland, Ohio

National Aeronautics and
Space Administration

Glenn Research Center

December 2003

Acknowledgments

The Marek-Jerzy Pindera and Jacob Aboudi gratefully acknowledge the support provided by the NASA Glenn Research Center through the NASA Grant NAG3–2359.

This work was sponsored by the Low Emissions Alternative Power Project of the Vehicle Systems Program at the NASA Glenn Research Center.

Available from

NASA Center for Aerospace Information
7121 Standard Drive
Hanover, MD 21076

National Technical Information Service
5285 Port Royal Road
Springfield, VA 22100

Available electronically at http://gltrs.grc.nasa.gov

Analysis of Plasma-Sprayed Thermal Barrier Coatings with Homogeneous and Heterogeneous Bond Coats Under Spatially Uniform Cyclic Thermal Loading

Marek-Jerzy Pindera
University of Virginia
Charlottesville, Virginia 22904, USA

Jacob Aboudi
Tel-Aviv University
Ramat-Aviv 69978, ISRAEL

Steven M. Arnold
National Aeronautics and Space Administration
Glenn Research Center
Cleveland, Ohio, USA

Abstract. This report summarizes the results of a numerical investigation into a major failure mechanism in plasma-sprayed thermal barrier coatings observed under spatially-uniform cyclic thermal loading which mimics a furnace durability test. In particular, factors leading to spallation of the top coat caused by the top/bond coat thermal expansion mismatch concomitant with deposition-induced interfacial roughness, oxide film growth and creep-induced normal stress reversal at the rough interface's crest are analyzed. Further, recent attemps to increase coating durability through the reduction of the top/bond coat thermal expansion mismatch achieved by embedding alumina particles in the bond coat are also critically examined. The analysis focuses on the evolution of local stress and inelastic strain fields in the vicinity of the rough top/bond coat interface during thermal cycling, and how these fields are influenced by the presence of an oxide film and spatially uniform and nonuniform (graded) distributions of alumina particles in the metallic bond coat. The impact of these factors on the potential growth of a local horizontal delamination at the rough interface's crest, thought to initiate at this location, is included in the investigation. In particular, the feasibility of grading the bond coat properties to reduce horizontal delamination driving forces is critically examined. The analysis is conducted using the Higher-Order Theory for Functionally Graded Materials which accounts for the high-temperature creep/relaxation effects within the individual TBC constituents. In the presence of two-phase bond coat microstructures, both the actual and homogenized bond coat properties are employed in the analysis in order to highlight the limitations of the prevalent homogenization-based approach applied to graded materials. The results reveal the important contributions of both the normal and shear stress components to the delamination growth potential in the presence of an oxide film, and suggest mixed-mode crack propagation characterized by crack deflections. The use of heterogeneous, two-phase bond coats, with spatially uniform or graded microstructure, is shown to increase the potential for delamination growth by increasing the magnitude of the shear stress component ahead of the crack tip.

1 INTRODUCTION

Thermal barrier coatings (TBCs) are widely employed on nickel-based structural components in the hot section of aircraft gas turbine engines. They enable the structural component to operate at a higher gas temperature, thereby increasing engine efficiency, or to operate longer at a given service temperature, thereby increasing the component durability. Zirconia-based coatings are typically used due to the low thermal conductivity of zirconia and its chemical stability at elevated temperatures. To prevent oxidation of the structural component, and improve the thermomechanical compatibility between the coating (top coat or TC) and the substrate, an intermmediate layer of a nickel-based alloy (bond coat or BC) is first deposited onto the substrate material, followed by the top coat itself. In oxidizing environments at elevated temperatures, the bond coat alloy composition produces a thin oxide film (called thermally-grown oxide or TGO) at the top coat/bond coat interface which acts as a protective oxidation barrier.

There are two competing types of zirconia-based coatings currently in use [1,2]; plasma-sprayed TBCs and electron-beam physical vapor-deposited (EB PVD) TBCs, Table 1. As their names imply, they are deposited onto the bond coat in two different ways, resulting in different microstructures and therefore different thermomechanical properties. The plasma-spray deposition process produces a coating with microstructure characterized by porosities and microcracks, and a rough top/bond coat interface whose strength is relatively low due to primarily mechanical interlocking mechanism. The porous microstructure results in low thermal conductivity, inelastic creep-like behavior suggested to be due to sliding of the rough microcrack interfaces [3], and low out-of-plane mechanical moduli and strength. A major failure mechanism for plasma-sprayed coatings is the spallation of the top coat from the bond coat which generally initiates at or just above the top coat/TGO interface, as discussed in more detail in the following section.

In contrast with the plasma-sprayed TBCs, the microstructure of EB PVD TBCs is columnar which results in low in-plane mechanical moduli due to the presence of vertical boundaries between adjacent columns of deposited zirconia, and thus more compliant in-plane response more commensurate with the bond coat behavior. The dense columnar microstructure within the individual columns results in a relatively higher thermal conductivity exhibited by EB PVD coatings. However, current attempts to decrease the thermal conductivity of EB PVD coatings to the level of plasma-sprayed coatings using oblique deposition methods are showing promise [4]. The electron beam vapor deposition process produces a smoother top coat/bond coat interface characterized by a stronger (chemical rather than mechanical) bond. Top coat spallation in the EB PVD coatings is typically observed at the bond coat/TGO interface. Despite the fact that these coatings are more durable than plasma-sprayed coatings, the high cost associated with the electron beam vapor deposition process limits their use to state-of-the-art airfoil applications.

1.1 Spallation Mechanism in Plasma-Sprayed TBCs

Early experimental investigations into failure mechanisms of plasma-sprayed TBCs conducted by Miller and Lowell [5] identified delamination at (or just above) the top/bond coat interface as the primary failure mode, ultimately leading to spallation of the zirconia coating. The failure mechanism was hypothesized to involve residual stresses induced into the coating during the cooldown stage of a thermal cycle due to the thermal expansion mismatch between the top coat and the bond coat. The failure initiation process was shown to be substantially influenced by the oxide film formation at the top/bond coat interface during exposure to elevated temperatures and, based on the observed location of delamination, the interface's irregularity was hypothesized to play a role.

The influence of rough interface, oxide film, and thermomechanical property mismatch on the

spallation mechanism has been subsequently studied by a number of investigators (cf. Evans et al. [6], Chang et al. [7,8], Petrus and Ferguson [9], Freborg et al. [10], Pindera et al. [11], Ali et al. [12]. These studies demonstrated the evolution of a non-zero stress component normal to the interface during cyclic thermal loading. Due to stress relaxation during the hold period of a heatup-hold-cooldown thermal cycle, this stress component becomes tensile at the interface's crest upon cooldown, setting up a delamination initiation site at this location. In the trough region, the normal stress becomes compressive, due also to stress relaxation. The growth of the oxide film at the top coat/bond coat interface subsequently changes the normal stress sign in the trough region, facilitating horizontal delamination growth. This model has been proposed by a number of investigators to explain the initiation and growth of delamination at or just above the top coat/oxide film interface, which ultimately leads to spallation.

The above investigations also demonstrated that the top/bond coat thermal expansion mismatch has the greatest effect on the evolution of the normal stress at the rough top/bond coat interface. In order to reduce this mismatch, and thus increase coating durability, Brindley et al. [13] fabricated TBCs with heterogeneous bond coats consisting of a uniform dispersion of submicron alumina particles in the nickel-based alloy bond coats. Durability experiments subsequently demonstrated consistent doubling of TBC life with just a 5% alumina particle content. Bond coats with up to 20% alumina particle content were also fabricated and tested, but showed substantial variability in durability due to oxidation problems which currently are being addressed through improved deposition techniques. It must be noted that attempts to increase TBC durability through the use of graded top coat microstructures consisting of a dispersion of metallic particles in plasma-sprayed top coats failed due to oxidation of the metallic phase at elevated temperatures [5]. The problem arises due to the high diffusivity of oxygen in zirconia. In addition, embedding high-conductivity particles in a low-conductivity matrix increases the overall coating conductivity, requiring a thicker coating for the same temperature drop. Therefore, for gas turbine applications in the aerospace environment this approach to increasing coating durability has been abondoned, as reiterated recently by Lee et al. [14]. These authors suggest alternate means of grading that circumvent the oxidation problem while providing stress management capabilities at the interfaces of the TBC constituents. For example, Zhu et al. [15] demonstrated free-edge interfacial stress reduction due to layer-graded bond coats in TBCs with flat interfaces.

In this report, we summarize the results of our investigation into the combined effects of oxide film thickness and heterogeneous bond coat microstructures on the evolution of stress and inelastic strain fields in plasma-sprayed thermal barrier coatings with rough interfaces subjected to spatially uniform thermal cyclic loading that simulates furnace durability test. The consideration of heterogeneous bond coat microstructures is motivated by the aforementioned results of Brindley et al. [13]. The objective is to better understand the mechanical factors that affect the proposed spallation mechanism model described above in this type of coatings and to critically examine potential solutions leading to enhanced coating durability. In this regard, the investigation considers the impact of the oxide film thickness and heterogeneous bond coat microstructures not only on the evolution of the stress component normal to the top/bond coat interface. The remaining stress components in the plane of the analyzed TBC system described in Section 3 are also considered, as is the evolution of the inelastic strain field which may provide the means for estimating the evolution of horizontal delaminations at or just above the crest of the rough interface. The presence of these delaminations is also taken explicitly into account in order to investigate the effect of grading the bond coat with alumina particles in the vicinity of the rough interfacial region on the potential reduction of horizontal delamination driving forces.

As in our previous investigation [11], the analysis of thermally-induced stresses in TBCs with graded bond coats during a spatially-uniform thermal cycle simulating a furnace heating dura-

bility test is conducted using the *higher-order theory for functionally graded materials* [16,17,18]. The analysis, which accounts for the important creep/relaxation effects within the individual TBC constituents, is conducted in two distinct ways which reflect the present dichatomy in the modeling of functionally graded materials. The coupled approach explicitly accounts for the micro-macrostructural interaction arising from the heterogeneous bond coat microstructure and is an intrinsic feature of the higher-order theory. The uncoupled approach, which is the prevailing paradigm in the mechanics/materials communities, replaces the heterogeneous bond coat microstructure by fictitious homogenized properties determined locally using a micromechanics model. The feasibility of using graded bond coat microstructures to reduce horizontal delamination driving forces is critically examined and the limitations of the homogenization-based approach are highlighted.

2 OUTLINE OF THE HIGHER-ORDER THEORY FOR FGMs

The higher-order theory for functionally graded materials is an approximate analytical approach, demonstrated to be sufficiently accurate in comparison with results obtained from more detailed finite-element analyses, for modeling stress and deformation fields in spatially nonuniform heterogeneous materials with different microstructural details. It circumvents the yet-to-be resolved problem of local homogenization of the material's spatially-variable heterogeneous microstructure, based on the concept of a representative volume element, by explicitly accounting for the microstructural details and local particle-particle interactions in the course of obtaining approximate analytical solutions for the local field quantities. This is accomplished by discretizing the volume occupied by a functionally graded material into subvolumes in a manner that mimics the material's microstructure. The analytical solution for the local field quantities is subsequently obtained by satisfying the field equations, namely the heat conduction equation

$$\frac{\partial q_1}{\partial x_1} + \frac{\partial q_2}{\partial x_2} + \frac{\partial q_3}{\partial x_3} = 0 \tag{1}$$

and the equilibrium equations

$$\frac{\partial \sigma_{1j}}{\partial x_1} + \frac{\partial \sigma_{2j}}{\partial x_2} + \frac{\partial \sigma_{3j}}{\partial x_3} = 0, \qquad (j = 1, 2, 3) \tag{2}$$

in each subvolume of the discretized microstructure in a volumetric sense, subject to the continuity of temperatures, heat fluxes, displacements and tractions between the individual subvolumes, and the external thermomechanical boundary conditions, imposed in a surface-average sense. Assuming that the material within each subvolume is isotropic, the heat flux components q_i in the above equations are related to the temperature field T through Fourier's law

$$q_i = -k\frac{\partial T}{\partial x_i} \tag{3}$$

where k is the thermal conductivity, while the stress components σ_{ij} are related to the total strain components ε_{ij} through Hooke's law

$$\sigma_{ij} = 2\,\mu\varepsilon_{ij} + \lambda\varepsilon_{kk}\delta_{ij} - 2\,\mu\varepsilon_{ij}^{in} - \sigma_{ij}^{T} \tag{4}$$

where λ and μ are the Lamé's constants of the material filling the given subvolume, ε_{ij}^{in} are the inelastic strain components based on the chosen inelastic constitutive theory, and σ_{ij}^{T} are the thermal stress components consisting of the products of the stiffness tensor elements, thermal expansion

coefficients and the temperature change. The total strain components in the individual subvolumes are obtained from the strain-displacement relations

$$\varepsilon_{ij} = \frac{1}{2}(\frac{\partial u_i}{\partial x_j} + \frac{\partial u_j}{\partial x_i}) \tag{5}$$

The solution of eqns (1)-(2) in the manner discussed above is accomplished by approximating the temperature and displacement fields within each subvolume using a quadratic expansion of the Legendre type in terms of local coordinates, as discussed in the following section. This is in sharp contrast with the linear expansion employed in the *Generalized Method of Cells* (GMC) developed to model the response of homogenized periodic multiphase materials, in which a similar subvolume discretization was employed [19]. As demonstrated in our previous investigations (cf. references [16,17,18]), a higher-order representation of the temperature and displacement fields is necessary in the present case in order to accurately capture the local effects created by the thermomechanical field gradients, the material's microstructure and the finite dimensions in the functionally graded directions. Hence *higher-order* is used to describe the present approach in order to differentiate it from GMC.

The next section briefly outlines the manner of volume discretization of a heterogeneous material's microstructure employed in the higher-order theory for FGMs. This discretization provides the basis for the approximate analytical solution of the governing field equations (1)-(2), which is described in the subsequent sections. The description of the solution methodology is sufficiently concise to facilitate the interpretation of the presented results, but avoids the lengthy derivations of the equations that provide solutions for the local field variables within the subvolumes of the discretized microstructure described in detail in references [16,17,18].

2.1 Volume Discretization

The version of the higher-order theory employed in the present investigation is based on a geometric model of a heterogeneous composite that occupies the region bounded by $|x_1| < \infty$, $0 \le x_2 \le H$, and $0 \le x_3 \le L$, Fig. 1. The loading applied to the composite may involve an arbitrary temperature or heat flux distribution and mechanical effects represented by a combination of surface displacements and/or tractions in the x_2-x_3 plane, and a uniform strain in the x_1 direction. The composite may be reinforced by an arbitrary distribution of continuous fibers or finite-length inclusions in the x_2-x_3 plane, continuously or periodically arranged in the direction of the x_1 axis. The microstructure of the heterogeneous composite in the x_2-x_3 plane is modeled by discretizing the heterogeneous composite's cross section into N_q and N_r generic cells in the intervals $0 \le x_2 \le H$, $0 \le x_3 \le L$, respectively. The indices q and r, whose ranges are $q = 1, 2, ..., N_q$ and $r = 1, 2, ..., N_r$, identify the generic cell in the $x_2 - x_3$ plane. The generic cell (q, r) consists of eight subcells designated by the triplet $(\alpha\beta\gamma)$, where each index α, β, γ takes on the values 1 or 2 which indicate the relative position of the given subcell along the x_1, x_2 and x_3 axis, respectively. The dimensions of the generic cell along the periodic x_1 direction, d_1 and d_2 are fixed, whereas the dimensions along the functionally graded directions x_2 and x_3, $h_1^{(q)}$, $h_2^{(q)}$, and $l_1^{(r)}$, $l_2^{(r)}$, can vary arbitrarily such that

$$H = \sum_{q=1}^{N_q}(h_1^{(q)} + h_2^{(q)}) \qquad L = \sum_{r=1}^{N_r}(l_1^{(r)} + l_2^{(r)}) \tag{6}$$

Given the applied thermomechanical loading, an approximate solution for the temperature and displacement fields within each $(\alpha\beta\gamma)$ subcell, referred to the local coordinate system $\bar{x}_1^{(\alpha)} - \bar{x}_2^{(\beta)} - \bar{x}_3^{(\gamma)}$ placed at the subcell's centroid, is constructed in two steps as described next.

2.2 Thermal Analysis

Let the functionally graded cross section shown in Fig. 1 be subjected to steady-state temperature or heat flux distributions on its bounding surfaces in the $x_2 - x_3$ plane. Under these circumstances, the heat flux field in the material occupying the subcell $(\alpha\beta\gamma)$ of the $(q,r)th$ generic cell, in the region $\left|\bar{x}_1^{(\alpha)}\right| \leq \frac{1}{2}d_\alpha$, $\left|\bar{x}_2^{(\beta)}\right| \leq \frac{1}{2}h_\beta^{(q)}$, $\left|\bar{x}_3^{(\gamma)}\right| \leq \frac{1}{2}l_\gamma^{(r)}$, must satisfy the heat conduction equation, eqn (1), expressed in the local subcell coordinate system,

$$\frac{\partial q_1^{(\alpha\beta\gamma)}}{\partial \bar{x}_1^{(\alpha)}} + \frac{\partial q_2^{(\alpha\beta\gamma)}}{\partial \bar{x}_2^{(\beta)}} + \frac{\partial q_3^{(\alpha\beta\gamma)}}{\partial \bar{x}_3^{(\gamma)}} = 0, \quad (\alpha,\beta,\gamma = 1,2) \tag{7}$$

The subcell heat flux components $q_i^{(\alpha\beta\gamma)}$ are obtained from the temperature field using the local version of eqn (3),

$$q_i^{(\alpha\beta\gamma)} = -k^{(\alpha\beta\gamma)} \frac{\partial T^{(\alpha\beta\gamma)}}{\partial \bar{x}_i^{(\cdot)}} \tag{8}$$

where $k^{(\alpha\beta\gamma)}$ are the coefficients of heat conductivity of the material in the subcell $(\alpha\beta\gamma)$, and no summation is implied by repeated Greek letters in the above and henceforth.

The temperature distribution in the subcell $(\alpha\beta\gamma)$ of the $(q,r)th$ generic cell, measured with respect to a reference temperature T_{ref}, is denoted by $T^{(\alpha\beta\gamma)}$. This temperature field is approximated by a second-order expansion in the local coordinates $\bar{x}_1^{(\alpha)}$, $\bar{x}_2^{(\beta)}$, $\bar{x}_3^{(\gamma)}$ as follows:

$$\begin{aligned} T^{(\alpha\beta\gamma)} &= T_{(000)}^{(\alpha\beta\gamma)} + \bar{x}_2^{(\beta)} T_{(010)}^{(\alpha\beta\gamma)} + \bar{x}_3^{(\gamma)} T_{(001)}^{(\alpha\beta\gamma)} + \frac{1}{2}(3\bar{x}_1^{(\alpha)2} - \frac{d_\alpha^2}{4}) T_{(200)}^{(\alpha\beta\gamma)} + \\ &\quad \frac{1}{2}(3\bar{x}_2^{(\beta)2} - \frac{h_\beta^{(q)2}}{4}) T_{(020)}^{(\alpha\beta\gamma)} + \frac{1}{2}(3\bar{x}_3^{(\gamma)2} - \frac{l_\gamma^{(r)2}}{4}) T_{(002)}^{(\alpha\beta\gamma)} \end{aligned} \tag{9}$$

where the unknown volume-averaged temperature $T_{(000)}^{(\alpha\beta\gamma)}$, and the higher-order coefficients $T_{(lmn)}^{(\alpha\beta\gamma)}$ $(l,m,n = 0,1,$ or 2 with $l+m+n \leq 2)$, are determined in the manner described below.

Given the six unknown quantities associated with each subcell (i.e., $T_{(000)}^{(\alpha\beta\gamma)}$, ..., $T_{(002)}^{(\alpha\beta\gamma)}$) and eight subcells within each generic cell, $48N_qN_r$ unknown quantities must be determined for a composite with N_q, and N_r rows and columns of cells containing arbitrarily specified materials. These quantities are determined by first satisfying the local heat conduction equation (7) in each subcell in a volumetric sense in view of the employed temperature field approximation. Subsequently, continuity of heat flux and temperature is imposed in a surface-average sense at the interfaces separating adjacent subcells, as well as neighboring cells. Fulfillment of these field equations and continuity conditions, together with the imposed thermal boundary conditions on the bounding surfaces of the composite, provides the necessary $48N_qN_r$ equations for the $48N_qN_r$ unknown coefficients $T_{(lmn)}^{(\alpha\beta\gamma)}$ in the temperature field expansion in each $(\alpha\beta\gamma)$ subcell. The final form of this system of equations can be symbolically written as

$$\boldsymbol{\kappa}\mathbf{T} = \mathbf{t} \tag{10}$$

where the structural thermal conductivity matrix $\boldsymbol{\kappa}$ contains information on the geometry and thermal conductivities of the individual subcells $(\alpha\beta\gamma)$ in the N_qN_r cells spanning the x_2 and x_3 directions, the thermal coefficient vector $\mathbf{T}$ contains the unknown coefficients that describe the temperature field in each subcell, i.e.,

$$\mathbf{T} = [\mathbf{T}_{11}^{(111)}, ..., \mathbf{T}_{N_qN_r}^{(222)}]$$

where

$$\mathbf{T}_{qr}^{(\alpha\beta\gamma)} = [T_{(000)}, T_{(010)}, T_{(001)}, T_{(200)}, T_{(020)}, T_{(002)}]_{qr}^{(\alpha\beta\gamma)}$$

and the thermal force vector $\mathbf{t}$ contains information on the thermal boundary conditions.

2.3 Mechanical Analysis

Given the temperature field generated by the applied surface temperatures and/or heat fluxes obtained in the preceding section, the resulting displacement and stress fields are then determined. This is carried out for arbitrary mechanical loading, consistent with global equilibrium requirements, applied to the surfaces of the composite.

The stress field in the subcell $(\alpha\beta\gamma)$ of the $(q,r)th$ generic cell generated by the given temperature field must satisfy the equilibrium equations, eqn (2), expressed in the local coordinate system

$$\frac{\partial \sigma_{1j}^{(\alpha\beta\gamma)}}{\partial \bar{x}_1^{(\alpha)}} + \frac{\partial \sigma_{2j}^{(\alpha\beta\gamma)}}{\partial \bar{x}_2^{(\beta)}} + \frac{\partial \sigma_{3j}^{(\alpha\beta\gamma)}}{\partial \bar{x}_3^{(\gamma)}} = 0, \ (j = 1, 2, 3) \tag{11}$$

The subcell stress components $\sigma_{ij}^{(\alpha\beta\gamma)}$ are obtained from the local version of eqn (4)

$$\sigma_{ij}^{(\alpha\beta\gamma)} = 2\,\mu^{(\alpha\beta\gamma)} \varepsilon_{ij}^{(\alpha\beta\gamma)} + \lambda^{(\alpha\beta\gamma)} \varepsilon_{kk}^{(\alpha\beta\gamma)} \delta_{ij} - 2\,\mu^{(\alpha\beta\gamma)} \varepsilon_{ij}^{in(\alpha\beta\gamma)} - \sigma_{ij}^{T(\alpha\beta\gamma)} \tag{12}$$

where $\lambda^{(\alpha\beta\gamma)}$ and $\mu^{(\alpha\beta\gamma)}$ are the Lamé's constants of the material filling the given subcell $(\alpha\beta\gamma)$, $\varepsilon_{ij}^{in(\alpha\beta\gamma)}$ are the inelastic strain components, and $\sigma_{ij}^{T(\alpha\beta\gamma)}$ is the thermal stress consisting of the products of the stiffness tensor components, thermal expansion coefficients and the temperature change. The subcell strain components are then obtained from the strain-displacement relations (5) expressed in the local coordinate system.

The displacement field in the subcell $(\alpha\beta\gamma)$ of the $(q,r)th$ generic cell is approximated by a second-order expansion in the local coordinates $\bar{x}_1^{(\alpha)}$, $\bar{x}_2^{(\beta)}$, and $\bar{x}_3^{(\gamma)}$ as follows:

$$u_1^{(\alpha\beta\gamma)} = \bar{x}_1^{(\alpha)} W_{1(100)}^{(\alpha\beta\gamma)} \tag{13}$$

$$\begin{aligned} u_2^{(\alpha\beta\gamma)} &= W_{2(000)}^{(\alpha\beta\gamma)} + \bar{x}_2^{(\beta)} W_{2(010)}^{(\alpha\beta\gamma)} + \bar{x}_3^{(\gamma)} W_{2(001)}^{(\alpha\beta\gamma)} + \frac{1}{2}(3\bar{x}_1^{(\alpha)2} - \frac{d_\alpha^2}{4}) W_{2(200)}^{(\alpha\beta\gamma)} + \\ &\quad \frac{1}{2}(3\bar{x}_2^{(\beta)2} - \frac{h_\beta^{(q)2}}{4}) W_{2(020)}^{(\alpha\beta\gamma)} + \frac{1}{2}(3\bar{x}_3^{(\gamma)2} - \frac{l_\gamma^{(r)2}}{4}) W_{2(002)}^{(\alpha\beta\gamma)} \end{aligned} \tag{14}$$

$$\begin{aligned} u_3^{(\alpha\beta\gamma)} &= W_{3(000)}^{(\alpha\beta\gamma)} + \bar{x}_2^{(\beta)} W_{3(010)}^{(\alpha\beta\gamma)} + \bar{x}_3^{(\gamma)} W_{3(001)}^{(\alpha\beta\gamma)} + \frac{1}{2}(3\bar{x}_1^{(\alpha)2} - \frac{d_\alpha^2}{4}) W_{3(200)}^{(\alpha\beta\gamma)} + \\ &\quad \frac{1}{2}(3\bar{x}_2^{(\beta)2} - \frac{h_\beta^{(q)2}}{4}) W_{3(020)}^{(\alpha\beta\gamma)} + \frac{1}{2}(3\bar{x}_3^{(\gamma)2} - \frac{l_\gamma^{(r)2}}{4}) W_{3(002)}^{(\alpha\beta\gamma)} \end{aligned} \tag{15}$$

where $W_{i(000)}^{(\alpha\beta\gamma)}$, which are the volume-averaged displacements, and the higher-order terms $W_{i(lmn)}^{(\alpha\beta\gamma)}$ $(i = 1, 2, 3)$ must be determined from conditions similar to those employed in the thermal problem. In this case, there are 104 unknown coefficients $W_{i(lmn)}^{(\alpha\beta\gamma)}$ in a generic cell (q,r), accounting for the periodicity in the x_1 direction using a homogenization procedure (cf. Aboudi et al. [18]). The determination of these coefficients parallels that of the thermal problem. Here, the heat

conduction equation is replaced by the equilibrium equations (11), and the continuity of tractions and displacements at the various interfaces replaces the continuity of heat fluxes and temperature. Finally, the boundary conditions involve the appropriate mechanical quantities.

Application of the above equations and conditions in a volumetric and a surface-average sense, respectively, produces a system of $104N_qN_r$ algebraic equations in the unknown coefficients $W_{i(lmn)}^{(\alpha\beta\gamma)}$. The final form of this system of equations is symbolically represented by

$$\mathbf{KU} = \mathbf{f} + \mathbf{g} \tag{16}$$

where the structural stiffness matrix $\mathbf{K}$ contains information on the geometry and thermomechanical properties of the individual subcells $(\alpha\beta\gamma)$ within the cells comprising the functionally graded composite, the displacement coefficient vector $\mathbf{U}$ contains the unknown coefficients that describe the displacement field in each subcell, i.e.,

$$\mathbf{U} = [\mathbf{U}_{11}^{(111)}, ..., \mathbf{U}_{N_qN_r}^{(222)}]$$

where

$$\mathbf{U}_{qr}^{(\alpha\beta\gamma)} = [W_{1(100)}, ..., W_{3(002)}]_{qr}^{(\alpha\beta\gamma)}$$

and the thermomechanical force vector $\mathbf{f}$ contains information on the mechanical boundary conditions and the thermal loading effects generated by the applied temperature. In addition, the inelastic force vector $\mathbf{g}$ appearing on the right hand side of eqn (16) contains inelastic effects given in terms of the integrals of the inelastic strain distributions that are represented by the coefficients $R_{ij(lm,n)}^{(\alpha\beta\gamma)}$ defined below

$$R_{ij(l,m,n)}^{(\alpha\beta\gamma)} = \mu^{(\alpha\beta\gamma)}\Lambda_{(lmn)} \int_{-1}^{+1}\int_{-1}^{+1}\int_{-1}^{+1} \varepsilon_{ij}^{in(\alpha\beta\gamma)} P_l(\zeta_1^{(\alpha)}) P_m(\zeta_2^{(\beta)}) P_n(\zeta_3^{(\gamma)})\, d\zeta_1^{(\alpha)} d\zeta_2^{(\beta)} d\zeta_3^{(\gamma)} \tag{17}$$

where

$$\Lambda_{(lmn)} = \frac{1}{4}\sqrt{(1+2l)(1+2m)(1+2n)}$$

and the Legandre polynomials $P.(\zeta_i^{(\cdot)})$ are functions of the non-dimensionalized variables $\zeta_i^{(\cdot)}$'s, defined in the interval $-1 \le \zeta_i^{(\cdot)} \le +1$, which are given in terms of the local subcell coordinates as follows: $\zeta_1^{(\alpha)} = \bar{x}_1^{(\alpha)}/(d_\alpha/2)$, $\zeta_2^{(\beta)} = \bar{x}_2^{(\beta)}/(h_\beta^{(q)}/2)$, and $\zeta_3^{(\gamma)} = \bar{x}_3^{(\gamma)}/(l_\gamma^{(r)}/2)$. These integrals depend implicitly on the elements of the displacement coefficient vector $\mathbf{U}$, requiring an incremental solution of eqn (16) at each point along the loading path.

Similarities and differences between the higher-order theory and standard displacement-based finite-element formulations have been described elsewhere [20]. An important advantage of the present approach is the simultaneous satisfaction of displacement and traction continuity conditions between the different subvolumes of the spatially variable microstructure. This facilitates the determination of thermally-induced stresses across the top/bond coat interface in the present application which cannot be easily captured due to very localized and very steep gradients in the thickness direction.

3 PROBLEM DEFINITION

3.1 TBC System Geometry

We consider a flat TBC system shown in Fig. 2 that remains in a generalized plane strain state under the imposed spatially uniform thermal loading which simulates furnace thermal cycling used

for durability testing, Fig. 3. The rough interface between the top and bond coats is modeled by a periodically-varying sine form located at the mean elevation of 630 μm from the substrate's bottom, with the wavelength of 25 μm and total (crest-to-trough) amplitude of 10 μm. These are representative values employed by previous investogators in modeling surface roughness of plasma-sprayed coatings (cf. Freborg et al. [10]). An oxide film with three different thicknesses (1, 2 and 3 μm) is introduced into the bond coat at the top/bond coat interface to simulate progressive bond coat oxidation. In the present analysis, the actual oxide film growth (and the accompanying stress) is not modeled as it occurs primarily at the elevated temperature during the hold portion of the heating cycle where relaxation rates, which control the oxide growth-induced stress, are much greater than the film growth itself, as will be demonstrated in Section 4.

Due to the periodic nature of the modeled TBC's geometry, the analysis of thermally-induced stress and inelastic strain fields is performed on the repeating cross-section element bounded by two vertical planes passing through the crest and trough of the sinusoidally-varying interface. Symmetry boundary conditions on the deformation of these planes are imposed consistent with the modeled geometry and the generalized plane strain state (namely, $\bar{\sigma}_{11} = \bar{\sigma}_{33} = 0$, where the bars denote average values of the normal stresses in the $x_2 - x_3$ and $x_1 - x_2$ planes). The repeating cross-section element of the TBC system is discretized into generic cells and subcells in order to approximate the geometry of the sinusiodally-varying interface with sufficient accuracy. Figure 4 illustrates the employed volume discretization in the region containing the wavy interface for the investigated TBCs in the absence of horizontal delamination above the interface's crest. The stress and inelastic strain fields will be presented in this region in the Results section. The discretized regions of the pure TBC systems (consisting of the top coat, bond coat and substrate only) with different oxide film thicknesses, and heterogeneous bond coat TBC systems containing uniform dispersions of aluminum oxide inclusions with 20% and 40% content in the vicinity of the top/bond coat interface within the bond coat, are shown in Fig. 4(a). The TBC systems with the actual and homogenized graded bond coat microstructures are shown in Fig. 4(b). The alumina particle in-plane dimensions are typically 0.5×0.5 μm. The grading is accomplished by gradually decreasing the alumina particle content from 40% at the wavy interface's crest to 0% below the trough. The homogenized microstructure of the graded bond coat consists of eight layers, with progressively decreasing uniform alumina particle content in increments of 5%, whose average or macroscopic properties have been calculated using the Generalized Method of Cells, as discussed in the following section.

In addition, several configurations are analyzed in the presence of a horizontal crack of total length 4.25 μm introduced at a distance of 0.5 μm above the interface's crest within the top coat, with traction-free boundary conditions imposed on the subcell faces separated by the crack. Such crack may arise upon cooldown due to the high normal stress in the crest region relative to the low transverse strength of the plasma-sprayed top coat. In order to capture the large stress gradients in the vicinity of the crack tip, the mesh in this region for the affected TBC configurations was further refined as shown in Fig. 5 for the pure TBC, showing the region in which the stress and inelastic strain fields will be presented in the Results section in the presence of the horizontal delamination. The same mesh refinement was employed for the graded bond coat TBCs, with and without an oxide film, containing horizontal delaminations (not included in the figure).

We note that the higher-order theory cannot capture the singular behavior at the crack tip as it is an approximate analysis based on volume-averaging of the field equations within discretized subvolumes of the material. Therefore, the present approach cannot be used to calculate the critical stress intensity factors and energy release rates which are employed in classical fracture mechanics analyses to predict crack initiation and propagation. However, we point out that these fracture mechanics parameters are yet to be determined for plasma-sprayed zirconia coatings. Further, it is

not clear that the classical fracture mechanics approach can be used to predict crack growth given the porous and pancake-like microstructure of the top coat. On the other hand, by discretizing the region in the vicinity of the crack tip sufficiently well, the higher-order theory is capable of capturing the high stress gradients, as well as high magnitudes of the stress field, with sufficient accuracy. This has been demonstrated previously in the context of the free-edge problem in the case of a laminated composite plate [16,17]. Our objective is to investigate the relative effect of grading on the stress gradients and stress magnitudes in the presence of a horizontal crack in order to determine the feasibility of using this approach to reduce the crack driving forces leading to top coat delamination and ultimately spallation.

3.2 Constituents' Material Response

The material thermoelastic and viscoplastic parameters that govern the response of the individual TBC constituents are given in Tables 2-5. These are the same as the parameters used in our previous investigation dealing with the effects of interfacial roughness and oxide film thickness on the inelastic response of TBCs with homogeneous bond coats [11], and are based on the properties employed by Freborg et al. [10]. The viscoplastic response of the zirconia top coat, NiCr-based bond coat, and Ni-based substrate is modeled by a power-law creep equation, generalized to multi-axial loading situations as follows,

$$\dot{\varepsilon}^c_{ij} = \frac{3F(\sigma_e, T)}{2\sigma_e}\sigma'_{ij} \tag{18}$$

where σ'_{ij} are the components of the stress deviator, $\sigma_e = \sqrt{3/2\,\sigma'_{ij}\sigma'_{ij}}$, and

$$F(\sigma_e, T) = A(T)\sigma_e^{n(T)} \tag{19}$$

where the temperature-dependent parameters A, n are listed in the tables in the range $10 - 1200^\circ$ C.

The alumina particles and TGO film are assumed to be elastic since their creep response is small for the employed thermal loading compared with the other materials. Further, the pronounced inelastic response of plasma-sprayed zirconia compared to fully densified zirconia is due to the local deformation mechanisms activated by porosities and microcracks introduced during the plasma-sprayed process, not modeled in this investigation, as discussed by DiMassi-Marcin et al. [3]. The power-law creep model for the inelastic response of zirconia has been shown to model the overall effect of these mechanisms with sufficient accuracy.

The Generalized Method of Cells micromechanics model was employed to calculate the macroscopic thermoelastic and creep parammeters of the homogenized NiCrAlY+Al_2O_3 layers. The homogenized Young's moduli, Poisson's ratios, and thermal expansion coefficients as a function of the alumina inclusion content at different temperatures are given in Tables 6-8, respectively. Figure 6 illustrates graphically the reduction of the top/bond coat thermal expansion coefficient mismatch as a function of temperature for different alumina particle content in the homogenized bond coat layers. This mismatch is typically thought to be important in controling the evolution of residual stresses in TBCs.

In order to determine the macroscopic creep response of the homogenized layers, creep experiments were simulated for different volume fractions of the Al_2O_3 inclusions in the NiCrAlY matrix at different temperatures using the Generalized Method of Cells. This was accomplished by imposing a very rapid rate of uniaxial loading up to a pre-determined load level, applied to the representative volume element for the particular NiCrAlY+Al_2O_3 microstructure, and then holding that load level constant for a fixed period of time. The resulting macroscopic strain was

then monitored as a function of time to determine the functional form of the macroscopic creep model. These numerical simulations, or experiments, revealed that the creep response for the homogenized layers exhibits very little primary creep, with the strain rate of the homogenized layers quickly becoming constant over the period of numerical simulations which was chosen to be on the order of the employed thermal loading history shown in Fig. 3. That is, the functional form of the multi-axial creep model for the homogenized layers remains the same as that of the NiCrAlY matrix given by Eqs. (18) and (19), with the creep parameters A and n modified by the Al_2O_3 inclusion presence. These parameters depend on the alumina particle content at different temperatures and are given in Tables 9 and 10. Examination of these tables reveals that of the two creep parameters in the power-law creep model for the homogenized NiCrAlY+Al_2O_3 layers, the power-law creep coefficient is the parameter most affected by the Al_2O_3 inclusion presence, with the power-law creep exponent generally unaffected by the microstructural effects for this particular material system in the given Al_2O_3 volume fraction range.

The above numerical results which indicate that the functional form of the power-law creep response at the constituent level retains the same form at the homogenized composite level, although somewhat surprising, is not new. This finding for our material system is consistent with the results reported by Crossman et al. [21] and Crossman and Karlak [22] in the context of the creep response of metal matrix composites.

4 RESULTS

In this report, we focus on the three stress components in the vicinity of the wavy interface in the $x_2 - x_3$ plane, namely the two normal stresses σ_{22} and σ_{33} and the shear stress σ_{23}. The influence of the normal stress σ_{22} on top coat delamination leading to spallation has been extensively investigated for pure TBCs with evolving oxide film (albeit without explicitly incorporating the crack's presence). The role that the inplane shear stress plays in the delamination process, on the other hand, has not been extensively discussed. The regions of interest are the top coat just above the wavy interface where the spallation process is generally assumed to initiate, as well as the oxide film where all the stress components may play a significant role in the oxide film's degradation.

In addition, two measures of inelastic strain accumulation during thermal cycling are also included in the results as they may provide important information useful in fatigue life calculations. The integrated effective inelastic strain measure is defined in the standard way as

$$\varepsilon_{eff}^{int} = \int d\varepsilon_{eff}^{c} \tag{20}$$

where $d\varepsilon_{eff}^{c} = \sqrt{2/3 d\varepsilon_{ij}^{c} d\varepsilon_{ij}^{c}}$. It is always positive and cannot decrease. In the presence of cyclic loading where inelastic strain reversal occurs, this measure gives us the total inelastic strain that a material experiences at a given point. It will increase monotonically during the evolution of inelastic strain even when inelastic strain reversal occurs due to the way it has been defined, tending asymptotically to a certain limit in those situations when the evolution of inelastic strains tends to zero. In order to ascertain the possibility of inelastic strain reversal, the residual inelastic effective strain measure is defined in terms of the total creep strain components ε_{ij}^{c}

$$\varepsilon_{eff}^{res} = \sqrt{2/3[(\varepsilon_{11}^{c})^2 + (\varepsilon_{22}^{c})^2 + (\varepsilon_{22}^{c})^2 + 2(\varepsilon_{23}^{c})^2 + 2(\varepsilon_{12}^{c})^2 + 2(\varepsilon_{13}^{c})^2} \tag{21}$$

This measure gives us the instantaneous value of the effective inelastic strain, and upon comparison with the integrated measure, provides information on the inelastic strain reversal. Clearly, the two

measures will produce the same value when the inelastic strain components increase or decrease monotonically and proportionally. During non-proportional and non-monotonic inelastic strain evolution, the two values generally will be different. In particular, when inelastic strain reversal occurs during cyclic loading, ε_{eff}^{int} will be greater than ε_{eff}^{res}, with the difference providing a measure of inelastic strain reversal.

4.1 Baseline Results for a Homogeneous TBC without an Oxide Film

As the first step, we establish the baseline results for the response of a pure TBC system without an oxide film subjected to the thermal cycle illustrated in Fig. 3 applied successively three times. Figure 7 illustrates the evolution of the three stress components, Fig. 7(a,b,c), and two measures of the effective plastic strain, Fig. 7(d,e), during the first cycle at $t = 30s$, $360s$, and $630s$, and at the corresponding times during the third cycle, namely at $t = 1290s$, $1620s$, and $1890s$. These times correspond to points along the thermal history during the initial heating period, end of the hold period, and end of the entire cycle. During the first cycle, the normal stress σ_{22} attains maximum and minimum values at the crest and trough of the wavy interface at these times.

The normal stress σ_{22} distributions in the vicinity of the wavy interface (in the same region as shown in Fig. 4) at the six times are shown in Fig. 7(a). During the initial heating period in the first cycle, the normal stress σ_{22} is compressive in the crest region and tensile in the trough region. This stress component relaxes to nearly zero during the hold period of the thermal cycle, thereby becoming tensile in the crest region and compressive in the trough region upon cooldown. This is consistent with the previously reported results discussed earlier. During subsequent cycles, the σ_{22} distribution decreases upon heatup, relaxes to nearly zero during the hold period, and returns to essentially the same state upon cooldown as at the end of the first cycle. The maximum magnitudes occur in the crest and trough regions.

Similar relaxation effects are observed in the distributions of the remaining two stress components. In the case of the normal stress σ_{33}, Fig. 7(b), the tensile distribution in the entire wavy interface region during the heatup portion of the first cycle relaxes to nearly zero during the hold period and becomes compressive upon cooldown. During subsequent cycles, the stress distribution decreases in magnitude during the heating portion, remains small during the hold period, and upon cooling returns to its previous state achieved at the end of the first cycle as observed in the bottom portion of Fig. 7(b) at the end of the third cycle. The maximum magnitudes of the normal stress σ_{33} in the vicinity of the wavy interface occur within the bond coat in the trough region.

In the case of the shear stress σ_{23}, Fig. 7(c), the stress distributions are characterized by a sign change across the wavy interface and the maximum stress magnitudes occur somewhat off the crest and trough locations. During the initial heatup period in the first cycle, the shear stress changes from positive to negative as the interface is traversed from the bond coat to the top coat regions almost along the entire interface. Stress relaxation during the hold period produces a reversal in the shear stress sign along the entire interface upon cooldown. As in the case of the two normal stresses, during subsequent cycles the shear stress decreases during the heatup stage and returns to the state attained after completion of the first cycle upon cooldown.

The two measures of the effective inelastic strain distributions are shown in Figs. 7(d) and 7(e). In the case of the integrated strain measure, Fig. 7(d), we observe continuous inelastic strain growth which initiates at the wavy interface's crest and eventually spreads to the bond coat during subsequent cycles, with the maximum magnitudes occuring along the wavy interface on the bond coat side. The distributions of the residual effective inelastic strain, Fig. 7(e), indicate that substantial plastic strain accumulation occurs during the hold period of the first cycle and actually decreases upon cooldown, with the maximum magnitude of this strain measure occuring at the

wavy interface's crest. During subsequent cycles, this strain increases during the hold period and subsequently decreases upon cooldown. An increase in the strain magnitude is observed at the wavy interface's crest at the end of the third cycle relative to the first cycle. These results indicate that inelastic strain reversal occurs during thermal cycling which could potentially produce fatigue-like failures in the top and bond coats.

4.2 Effect of Oxide Film Thickness in a Homogeneous TBC

The presence of the oxide film substantially modifies the stress and inelastic strain distributions throughout the thermal loading history. One common feature with the baseline results, however, is the near stabilization of the stress field at the end of each thermal cycle. In view of this, only the results at the end of the third cycle will be presented.

Figure 8(a) compares the normal σ_{22} stress distributions in the vicinity of the wavy interfacial region that arise in TBCs with an oxide film of increasing thickness (1, 2, and 3 μm) at $t = 1890s$. In the top portion of this figure, the colorbar scale has been adjusted to shown the effect of the oxide film thickness on the stress field in the top coat region in the vicinity of the wavy interface. As observed, the normal stress σ_{22} at the crest decreases with increasing film thickness. This is accompanied by the spread of the tensile value of this stress component into the trough region. Concurrently, the normal stress in the bond coat in the crest region becomes more tensile, and more compressive in the trough region. In the oxide film itself, the normal stress becomes initially more compressive away from the crest with increasing film thickness, attaining very large magnitudes. The largest compressive stress occurs in the 2 μm oxide film. This is illustrated more clearly in the bottom portion of Fig. 8(a) where the colorbar scale has been adjusted accordingly.

The normal σ_{33} stress distributions for different oxide film thicknesses are presented in Fig. 8(b). In this case, increasing the film thickness has a relatively small effect in the top coat. Specifically, the magnitude of the compressive normal stress increases in the top coat region above the trough, and decreases at the crest to the point where σ_{33} becomes slightly tensile as the film thickness increases. The greatest effect, however, occurs in the bond coat and the oxide film itself. In particular, σ_{33} becomes tensile in the bond coat at the crest and trough of the oxide film/bond coat interface, and more compressive away from these locations due to the oxide film presence and the required traction continuity in the x_3 direction. The large compressive normal stress that arises within the oxide film in the trough region decreases somewhat with increasing film thickness, as illustrated more clearly in the bottom portion of Fig. 8(b).

The presence of the oxide film changes the sign of the shear stress in the top coat just to the right of the wavy interface's crest at the end of the cycle from positive to negative, upon comparison of Fig. 8(c) with the results presented in Fig. 7(c). The magnitude of this negative shear stress increases with increasing oxide film thickness, as does its penetration into the region above the trough. Similarly, the magnitude of the negative shear stress in the bond coat in the region to the left of the interface's trough increases with increasing film thickness. In the oxide film itself, large positive shear stress is present resulting in large shear stress gradient across the interfaces on either face of the film.

The presence of the oxide film changes the locations where the integrated effective inelastic strain tends to concentrate, Fig. 8(d). Specifically, the growth of this inelastic strain measure is suppressed at the crest location in the immediate vicinity of the top coat/oxide film and oxide film/bond coat interface, but enhanced deeper within the bond coat itself. The growth of this inelastic strain is also enhanced in the top coat in the region above the trough. The magnitude of the integrated inelastic effective strain and its spread in these regions increases with increasing oxide film thickness. Similar behavior is observed in the case of the residual effective inelastic strain

measure, with one important exception. In this case, the residual inelastic strain is substantially more pronounced in the top coat than the bond coat, Fig. 8(e). The location where it is maximum changes from just to the right of the crest for the thinnest oxide film to the location along the oxide film/top coat interface halfway between the crest and trough. The crest and trough regions above and below the oxide film are sheltered from residual strain accumulation, as suggested by the results presented in Fig. 8(d).

4.3 Effect of Spatially Uniform Bond Coat Microstructure

The experimental results of Brindley et al. [13] suggest that the reduction of the top/bond coat thermal expansion mismatch may potentially improve the TBC durability. In this section, we examine the effect of a uniform dispersion of alumina inclusions in the vicinity of the wavy interface on the three stress components in the $x_2 - x_3$ plane and the two effective inelastic strain measures. Figure 6 indicates that a relatively large alumina inclusion content is required to attain an appreciable reduction in the thermal expansion mismatch, which is substantially greater than the 5% and even 20% alumina particle content employed by Brindley and co-workers. This suggests that another mechanism may have been operative that improved the durability of TBCs investigated by these authors. Nevertheless, we employ 20% and 40% volume fractions of the alumina particles in the NiCrAlY matrix in the interfacial region to investigate the thus-far unquantified effect of the thermal expansion mismatch reduction on the evolution of stress and inelastic strain fields in the considered model TBC system.

In view of the preceding results which demonstrated stress field's stabilization after cooldown with subsequent cycles, the results are presented at $t = 630s$, or at the end of the first cycle. The field quantities were generated in two distinct ways that reflect the present dichotomy of modeling microstructural effects in heterogeneous materials. First, the bond coat microstructure was homogenized in the manner described earlier, and the homogenized effective properties were employed in the analysis. Subsequently, the analysis was repeated with the actual bond coat microstructure explicitly taken into account.

Figure 9(a) compares the effect of the alumina inclusion content on the normal σ_{22} stress distributions. The stress distributions in a TBC with homogeneous bond coat are included for comparison. The results indicate that when the actual bond coat microstructure is homogenized (top portion of Fig. 9(a)), reduction in the normal stress at the crest of the wavy interface is achieved which increases with increasing alumina inclusion content. At 40% of the alumina volume content, the reduction in the normal stress at the wavy interface's crest is substantial. This, however, is obtained at the expense of an increase in the magnitude of the compressive normal stress at the interface's trough, as well as increased magnitude of the normal stress in the bond coat below the wavy interface's crest. Alternatively, when the analysis is based on the actual bond coat microstructure, the extent of the normal stress reduction at the wavy interface's crest is not as substantial (bottom portion of Fig. 9(a)).

Figure 9(b) illustrates that the normal stress σ_{33} is affected to a relatively small extent by the heterogeneous bond coat microstructure in the top coat in the vicinity of the wavy interface. Specifically, some reduction in this normal stress component is observed in the crest region, which becomes less compressive with increasing alumina volume content. In the top coat's trough region the normal stress σ_{33} becomes more compressive with increasing alumina content. The greatest effect is observed in the bond coat itself, in particular just below the trough, where the normal stress becomes more compressive as the alumina content increases. The analysis based on the actual bond coat microstructure indicates that the normal stress in the pure matrix of the bond coat directly at the crest of the top/bond coat interface actually becomes tensile in the presence

of alumina inclusions (whose magnitude increases with increasing alumina content), which is not captured by the homogenized bond coat microstructure analysis.

Figure 9(c) illustrates that the effect of alumina content on the shear stress distribution is *in principle* similar to what was observed in the case of the normal stress σ_{22}. That is, increasing the alumina content decreases the shear stress in the top coat's crest region and increases it in the bond coat's trough region. However, the significant difference in this case is the change of the shear stress sign in the crest region with increasing alumina content. This results in an increase of the shear stress *magnitude* with increasing alumina content. In the trough region, the sign of the shear stress is not affected. The analysis based on the homogenized bond coat properties tends to underestimate the increase in the shear stress magnitude on the top coat side of the interface relative to the analysis based on the actual bond coat microstructure. However, the extent of the spread of the shear stress into the trough region is overestimated.

The effect of the bond coat microstructure on the integrated effective inelastic strain is demonstrated in Fig. 9(d). The homogenized analysis predicts an initial decrease in this inelastic strain measure on the top coat side of the wavy interface's crest relative to the homogeneous bond coat results, which subsequently increases with increasing alumina content. However, continuous increase is observed in the trough region of the top coat. In the bond coat itself, the growth of the integrated effective inelastic strain is suppressed directly below the crest of the wavy interface and shifts further down into the bond coat region with increasing alumina content. The analysis based on the actual bond coat microstructure indicates that the magnitude of the integrated effective inelastic strain is substantially underpredicted and overpredicted by the homogenized analysis in the crest and trough regions of the top coat, respectively. Further, channeling effects are observed in the bond coat itself, where distinct paths of intensive inelastic strain localization are observed. Similar effects are observed in the case of the residual effective inelastic strain distributions, Fig. (9e), with the differences between the two types of analysis somewhat magnified in the crest and trough regions of the top coat.

4.4 Combined Effects of Graded Bond Coat Microstructure and Oxide Film Thickness

The results of the preceding section indicate that the potentially beneficial effect of spatially uniform heterogeneous bond coat microstructure on the normal σ_{22} stress distribution in the top coat at the wavy interface's crest is offset by increased magnitude of this stress component in the trough region. This suggests that the normal stress σ_{22} at both locations can be managed by grading the bond coat microstructure from a high content in the crest region to a low content in the trough region. The effect of such grading strategy on all the stress and effective inelastic strain components is discussed in this section as a function of the oxide film thickness.

Figure 10(a) presents the combined effect of grading and oxide film thickness on the normal σ_{22} stress distributions at the end of the first thermal cycle. In the absence of the oxide film, it is observed that the normal stress σ_{22} at the crest of the wavy interface is very nearly the same as for the spatially uniform bond coat microstructures discussed earlier, while the magnitude of this stress component in the trough region is reduced. The presence of the oxide film further reduces the normal stress σ_{22} at the crest location, while enhancing it at the trough. These effects increase with increasing oxide film thickness as suggested by the results of Section 4.2. As in the previous cases, the analysis based on the homogenized bond coat microstructure overestimates the normal stress reduction at the wavy interface's crest and the oxide film-driven spread of the tensile zone into the trough region, relative to the analysis based on the actual bond coat microstructure. The differences in the normal stress distributions in the top coat obtained from these two types of

analyses decrease with increasing oxide film thickness. This suggests that the oxide film thickness effects dominate beyond a certain critical thickness.

The normal σ_{33} stress distributions shown in Fig. 10(b) indicate that the effect of the oxide film thickness is rather small in the top coat. Some reduction of this normal stress component occurs at the crest with increasing oxide thickness as previously observed in the Section 4.2 results. Comparing the results of Section 4.2 with the present ones indicates that the effect of the heterogeneous bond coat microstructure in the crest region is of secondary importance. Grading reduces the magnitude of the compressive stress σ_{33} in the lower region of the bond coat, including the trough, and the presence of the oxide film further reduces it in the trough region. The analysis based on the heterogeneous bond coat microstructure indicates that small matrix islands of the bond coat adjacent to the alumina particles directly below the wavy interface's crest experience tensile normal stress due to the thermal expansion mismatch. This is not captured by the analysis based on the homogenized bond coat properties, and has been observed previously.

While grading does reduce the magnitude of the shear stress σ_{23} in the bond coat's trough region, relative to the spatially uniform bond coat microstructure result, without affecting the shear stress in the top coat's crest region, this effect is overshadowed by the presence of the oxide film, Fig. 10(c). As suggested by the results of Section 4.2, increasing the film thickness increases the magnitude of σ_{23} in the crest region of the top coat, and accelerates its spread into the region above the trough. This is accompanied by increased magnitudes of the compressive shear stress in the trough region of the bond coat, and reduction of the zone along the top/bond coat interface where this stress component is tensile. As expected, the greatest differences in the shear stress distributions predicted by the two types of analysis are observed in the heterogeneous bond coat where the highly localized areas of positive shear stress are not well captured by the analysis based on the homogenized bond coat microstructure.

In the absence of the oxide film, grading suppresses the evolution of the integrated effective inelastic strain in the trough region of the top coat, Fig. 10(d), relative to the spatially uniform bond coat microstructure, Fig. 9(d). This is also observed at the wavy interface's crest region in the top coat, and also within the bond coat, according to the analysis based on the homogenized bond coat propertes, in contrast with the analysis based on the actual microstructure where little change is seen in the top coat at the crest. Increasing the oxide film thickness increases the integrated effective inelastic strain in the top coat's trough region, as well as in the bond coat itself, and decreases it above the crest of the wavy interface, according to both types of analysis. The differences between the analyses based on the homogenized and actual bond coat microstructure observed in the top coat region disappear with increasing oxide film thickness. Similar observations hold in the case of the residual effective inelastic strain, Fig. 10(e), whose magnitude in the affected regions is now much smaller as in the previously discussed cases. The primary difference between the integrated and residual effective inelastic strain distributions lies in the bond coat, where the differences between the two types of analysis are now more pronounced due to the lower magnitudes of the residual effective inelastic strain.

4.5 Combined Effects of Grading and Oxide Film Thickness on Delamination Driving Forces

Here, we focus on the normal stress σ_{22} and the inplane shear stress σ_{23} in the top coat itself in the vicinity of the horizontal crack above the rough top/bond coat interface's crest, Fig. 5, after one thermal cycle ($t = 630s$), as well as on the two measures of the inelastic effective strain. The influence of the normal stress on top coat delamination leading to spallation has been extensively investigated for pure TBCs with evolving oxide film (albeit without explicitly incorporating the

crack's presence). The role that the inplane shear stress plays in the delamination process, on the other hand, has not been extensively discussed. As noted previously, due to the pronounced stress relaxation during the hold period of the thermal cycle, these stress components do not change significantly at the end of subsequent thermal cycles for the chosen spatially uniform loading. Therefore one thermal cycle is sufficient to delineate the trends. As also noted previously, the horizontal crack may arise due to the relatively large normal stress σ_{22} that develops at the crest of the top/bond coat interface during the cooldown portion of the thermal cycle in the absence of an oxide film. We reiterate that during the first thermal cycle, this stress component is initially compressive at the crest of the interface during heating, but relaxes to nearly zero during the hold period. Hence, stress relaxation produces a sign reversal of the normal stress at the crest location upon cooldown. The same effect changes the sign of the normal stress in the trough region, from tensile during heating to compressive upon cooldown. During subsequent cycling, the residual stresses decrease to nearly zero during the heating and hold portions of the thermal cycle, assuming the same values upon cooldown as after the first cycle.

The normal and shear stress fields illustrating the differences that arise due to oxide film thickness and grading have been generated in the region shown in Fig. 5. The color scale in the contour plots that follow has been adjusted to clearly delineate the impact of these two effects on the crack-tip stress field in the top coat itself. Since the Young's modulus of the top coat is substantially smaller than that of the bond coat and oxide film/particles due to the coating's porous microstructure created by the plasma-spray deposition process, the stress field in the top coat is generally significantly smaller in magnitude than in the bond coat and oxide film regions. In some areas of these regions, therefore, the stress fields fall outside of the employed color scale.

Figure 11(a) presents comparison of the σ_{22} stress distributions in pure and graded TBCs in the absence of an oxide film. The large stress concentration at the crack tip in the pure TBC, Fig. 11(a) top left, is substantially reduced by grading the bond coat according to the analysis based on the graded bond coat's homogenized properties, Fig. 11(a) top right. This would appear to make a strong case for grading the bond coat. However, examination of the results based on the actual (or nonhomogenized) bond coat microstructure shown in the bottom portion of Fig. 11(a) indicates that the stress concentration reduction at the crack tip is not as substantial. Further, grading accelerates the spread of the tensile normal stress in the trough region which has been hypothesized to provide the driving force for horizontal crack growth during thermal cycling.

The oxide film presence reduces the crack-tip normal stress field for the pure and graded TBCs. Relative reductions for the TBCs with 1 μm film (not shown) follow the same trends as those shown in Fig. 11(a). That is, the analysis based on the homogenized graded bond coat microstructure produces a greater reduction relative to the pure TBC result than the analysis based on the actual microstructure. The results for the TBCs with 2 μm oxide film shown in Fig. 11(b) indicate that at this film thickness the crack-driving force due to σ_{22} has virtually disappeared for the pure TBC. Grading, however, now produces an increase in the normal stress concentration at the crack tip as will be more clearly shown subsequently. The relative increases predicted by the actual and homogenized bond coat microstructure analyses follow the same trend as in the preceding case. In addition, grading accelerates the spread of the tensile normal stress in the trough region.

Figures 11(c) and 11(d) quantify the effects of grading and oxide film's thickness on the normal stress distribution in the vicinity of the crack tip along the line coincident with the crack. The normal stress concentration *reduction* due to grading in the oxide film's absence is clearly observed in Fig. 11(c). In contrast, normal stress concentration *increase* in the presence of a 2 μm oxide film is seen in Fig. 11(d). Further, the dramatic effect of oxide film thickness, which overshadows the grading effect, is clearly observed upon comparison of Fig. 11(c) and 11(d). These results support the hypothesis that the normal stress by itself is not sufficient to provide the necessary

crack-driving force with increasing oxide film thickness during the initial crack extension stage. It is possible that TBC curvature, taken into account in previous investigations, increases the size of the tensile normal stress zone in the trough region, providing the necessary crack-driving force. However, examination of the inplane shear stress σ_{23} reveals an interesting, rarely discussed influence on the spallation mechanism as illustrated next.

Comparison of the σ_{23} stress distributions in pure and graded TBCs in the absence of an oxide film is presented in Fig. 12(a). In contrast with the normal stress results, the magnitude of the crack-tip shear stress concentration in the pure TBC, Fig. 12(a) top left, is now enhanced by grading according to the analysis based on the homogenized graded bond coat microstructure, Fig.12(a) top right. Further, the sign of the shear stress ahead of the crack tip is changed from positive to negative due to grading. The analysis based on the actual graded bond coat microstructure, Fig. 12(a) bottom, also predicts shear stress sign reversal in the crack-tip region, but the extent of the affected zone is smaller. Ahead of the crack tip, the magnitude of the shear stress is quite small, although the stress concentration directly at the crack tip is greater relative to the pure TBC result, as will be more clearly illustrated below.

The deleterious effect of grading on the enhancement of the shear stress field zone ahead of the crack tip is also evident in the presence of the 2 μm oxide film. Figure 12(b) presents comparison of the σ_{23} stress distributions in pure and graded TBCs in this case. The presence of the oxide film changes the sign of the shear stress field at the crack tip in the pure TBC, Fig. 12(b) top left (compare with Fig.12(a) top left). The size of the affected shear stress zone ahead of the crack tip is further magnified by grading. However, as will be seen below, the shear stress concentration directly at the crack tip is only slightly affected by grading. The analysis based on the homogenized graded bond coat microstructure, Fig. 12(b) top right, predicts a small increase in the magnitude of the shear stress concentration relative to the pure TBC case, while the analysis based on the actual graded bond coat microstructure, Fig. 12(b) bottom, predicts a slight decrease. Nevertheless, the deleterious effect of grading on the size of the shear stress field zone ahead of the crack tip is clear.

Figure 12(c) and 12(d) quantify the effects of grading and oxide film's presence on the shear stress distribution in the vicinity of the crack tip along the line coincident with the crack. The shear stress concentration *increase* directly at the crack tip due to grading is clearly observed in Fig. 12(c) in the oxide film's absence. The effect of grading on the crack-tip shear stress concentration virtually disappears with increasing oxide film thickness as seen in Fig. 12(d) for the 2 μm oxide film, in contrast with the enhancement of the shear stress-affected zone size observed in Fig. 12(b). These results support the hypothesis that the shear stress is an important component of the crack-driving force with increasing oxide film thickness during the initial crack extension stage. They also indicate that the grading-induced enhancement of the shear stress zone size ahead of the crack tip provides additional energy for crack extension.

The effects of grading and oxide film presence on the integrated inelastic strain distributions are illustrated in Fig. 13. In the absence of the oxide film, Fig. 13(a), the analysis based on the homogenized bond coat microstructure indicates a strain concentration reduction at the crack-tip relative to the strain concentration in the pure bond coat TBC. This is not predicted by the analysis based on the actual bond coat microstructure which, in fact, indicates an increase in the crack-tip inelastic strain concentration. The presence of the oxide film tends to decrease the evolution of the integrated inelastic strain at the crack tip, Fig. 13(b). This is predicted by both types of analysis. The residual inelastic strain distributions presented in Fig. 14 indicate inelastic strain reversal at the crack tip upon comparison with the results of Fig. 13. Such reversal may be important in the context of the top coat deformation model proposed by DiMassi-Marcin et al. [3]. The crack-tip residual strain concentration magnitude substantially decreases in the oxide film's presence.

5 SUMMARY OF RESULTS

The evolution of stress and strain fields in pure and heterogenous bond coat TBCs, with an oxide film at the top coat/bond coat interface, during spatially uniform cycling thermal loading generated using the Higher-Order Theory for Functionally Graded Materials is summarized below. In particular, the effects of oxide film thickness, and spatially uniform and graded microstructures are discussed in this order for each stress component.

5.1 Normal stress σ_{22}

- in a pure bond coat TBC without an oxide film, the crest and trough of the wavy interface experience compression and tension, respectively, during initial heating; stress relaxation during the hold period produces stress reversal upon cooldown, resulting in tension and compression stress at the crest and trough

- in a pure bond coat TBC with an oxide film, increasing the film thickness reduces this stress component at the top coat/oxide film interface's crest upon cooldown until it becomes compressive beyond a certain film thickness; in the trough region this stress is reversed upon cooldown from compression to tension with increasing film thickness; further, large and generally compressive magnitudes of this stress component develop within the oxide film itself, with maximum values occuring along the film's inclined planes

- in a heterogeneous bond coat TBC without an oxide film and with spatially uniform microstructure in the top coat/bond coat interfacial region, increasing the alumina particle content of the bond coat decreases this stress component at the wavy interface's crest at the expense of increased magnitude in the trough

- grading the heterogeneous bond coat microstructure from a high alumina content at the wavy interface's crest to low in the trough region makes it possible to manage stress magnitudes at both the crest and trough locations in the absence of an oxide film; in the presence of an oxide film increasing the film's thickness further reduces this stress component at the top coat/oxide film interface's crest but accelerates its sign reversal in the trough region from compression to tension; in addition, homogenized analysis overestimates stress reduction at the crest due to grading

5.2 Normal stress σ_{33}

- in a pure bond coat TBC without an oxide film, this stress component becomes tensile everywhere in the top and bond coat regions during initial heating, and compressive upon cooldown due to stress relaxation during the hold period

- in a pure bond coat TBC with an oxide film, the film presence has a relatively small effect on this stress component in the top coat; specifically, increasing the film thickness reduces the magnitude of this stress at the crest on the top coat side and at the trough on the bond coat side until it becomes tensile with sufficient thickness; away from the crest, however, the magnitude of this compressive stress in the top coat is somewhat increased; further, very large magnitudes of this compressive stress develop within the oxide film itself, with maximum values occuring in the oxide film's trough region

- in a heterogeneous bond coat TBC without an oxide film and with spatially uniform microstructure in the top coat/bond coat interfacial region, increasing the alumina particle

content of the bond coat has a small effect on this stress component in the top coat; specifically, this stress component decreases at the wavy interface's crest at the expense of somewhat increased magnitude in the trough; the greatest effect occurs in the heterogeneous bond coat itself where this stress component becomes locally tensile in the matrix phase below the crest

- grading the heterogeneous bond coat microstructure from a high alumina content at the wavy interface to low in the trough region has a small impact on the local stress distributions, and follows the same trend as for the spatially uniform microstructures, with increasing oxide film thickness contributing in a cumulative manner

5.3 Shear stress σ_{23}

- in a pure bond coat TBC without an oxide film, negative shear stress evolves in the top coat during initial heating, changing to positive upon cooldown due to relaxation during the hold period

- in a pure bond coat TBC with an oxide film, increasing the oxide film thickness reverses the shear stress from positive to negative in the off-crest region and increases its magnitude and growth into the trough region; further, large magnitudes of this stress component develop within the oxide film itself, with maximum values occuring along the oxide film's inclined planes

- in a heterogeneous bond coat TBC with spatially uniform microstructure in the top coat/bond coat interfacial region, increasing the alumina particle content of the bond coat has a similar effect as increasing the oxide film thickness in a pure bond coat TBC

- increasing the oxide film thickness in a graded bond coat TBC has a dramatic effect on this stress component by further increasing its magnitude at the top coat/oxide film interface's crest and above the trough region; in addition, homogenized analysis overestimates the extent of this increase

5.4 Effective inelastic strains ε_{eff}^{int} and ε_{eff}^{res}

- in a pure bond coat TBC without an oxide film, substantial inelastic strain reversal occurs in the top and bond coats during thermal cycling

- in a pure bond coat TBC with an oxide film, increasing the oxide film thickness suppresses the inelastic strain growth at the top/oxide film interface's crest and trough, while enhancing it in the top coat's trough region and within the bond coat below the crest

- in a heterogeneous bond coat TBC with spatially uniform microstructure in the top coat/bond coat interfacial region, increasing the alumina particle content of the bond coat localizes the inelastic strain at the crest and increases the inelastic strain accumulation in the trough region; these effects are not predicted accurately by the homogenized analysis

- increasing the oxide film thickness in a graded bond coast TBC reduces the inelastic strain accumulation at the crest at the expense of increasing it in the trough

The above results for the pure bond coat TBCs without an axide film are consistent with previous numerical studies reported in the literature. Similarly, the obtained results in the presence

of an oxide film at the top/bond coat interface are also consistent with the numerical results reported in the literature, however the focus in previous studies has been primarily on the normal stress component σ_{22} in view of the hypothesized failure mode. The results of this investigation, on the other hand, point to the important role of the shear stress component σ_{23} with increasing oxide film thickness thus far not extensively discussed.

The results obtained for TBCs with spatially uniform bond coat microstructures, also thus far not investigated, indicate that some management of the normal stress component σ_{22} is possible at the wavy interface's crest, albeit at the expense of increased stress magnitudes in the trough location. A potential way of managing the normal stress fields at both locations is by grading the alumina inclusion content from a high concentration at the crest to a low concentration at the trough. However, the use of both spatially uniform and graded bond coat microstructures enhances the magnitude of the shear stress component in the off-crest location. These results suggest that the combined effect of grading the bond coat and the presence of oxide film, while initially suppressing the σ_{22} component of the delamination driving stress field, will enhance the σ_{23} component of this field. This is indeed the case as demonstrated herein in the presence of a horizontal crack above the wavy interface's crest. Specifically, grading the bond coat:

- initially decreases the crack-tip stress concentration due to σ_{22} upon cooldown, however this effect is overshadowed by increasing oxide film thickness which reduces the crack-tip stress concentration to a substantially greater extent; at sufficiently large oxide film thickness grading actually enhances the crack-tip stress concentration somewhat
- increases the crack-tip stress concentration due to σ_{23} upon cooldown, which is further increased by increasing oxide film thickness

6 DISCUSSION

The mechanism for top coat delamination leading to spallation in pure plasma-sprayed TBCs proposed by a number of researchers [7-10] is primarily based on the stress component normal to the rough top/bond coat interface, which is modified in the trough region by the growth of an oxide film and stress relaxation effects, thereby providing the necessary driving force for horizontal delamination growth. This model is based on finite-element analyses of TBCs on curved substrates (without explicitly accounting for the presence of a local delamination), and is consistent with experimentally observed coating failure by spallation. Alternatively, our analysis of TBCs on flat substrates with no overall curvature indicates that in the presence of a horizontal delamination just above the crest of a rough top/bond coat interface, the crack-tip normal stress field actually decreases with increasing oxide film thickness, thereby decreasing the crack-driving force. Increasing oxide film thickness does change the sign of the normal stress from compression to tension in the trough region, however the extent of the tensile zone is not sufficient to provide the necessary crack-extension force for the investigated crack length and oxide film thicknesses. In contrast, the shear stress field at the crack tip increases with increasing oxide film thickness in the range considered. It is hypothesized, therefore, that this stress component provides the necessary driving force for crack extension during at least the initial delamination growth when the oxide film thickness is relatively small. Models for delamination growth based on mixed-mode fracture mechanics may, therefore, be more appropriate than just Mode I considerations. However, such models must take into account the inelastic behavior of the porous ceramic top coat characterized by the presence of dispersed microcracks. These microcracks appear to provide the mechanism by which inelastic effects occur due to sliding of the microcrack interfaces. The substantial inelastic strain accumulation and

reversal observed in our results would provide the mechanism by which a crack may grow in the presence of increasing shear stress field with increasing oxide film thickness. We note, in support of the shear stress contribution to the spallation mechanism, that experimental evidence exists which suggests that delamination growth in the top coat is not self-similar, i.e. it is not exclusively governed by Mode I consideration, but proceeds along a path characterized by deflections which conform to the overall shape of the rough interface [23].

The analysis of the use of heterogeneous bond coat microstructures indicates that, while grading the bond coat initially decreases the normal stress field at the crack tip, this reduction is overestimated by the analysis based on homogenized bond coat microstructure relative to the analysis based on the actual microstructure. The effect of grading on the crack-tip normal stress field becomes less important with increasing oxide film thickness (at least up to 2 μm). In addition, grading promotes the growth of the tensile normal stress zone in the rough interface's trough region, and has a similar effect, but a smaller impact, as increasing oxide film thickness in pure TBCs. Perhaps more significantly, grading increases the shear stress field at the crack tip, *which is further magnified by the presence of the oxide film.* This magnification is overestimated by the analysis based on homogenized bond coat microstructure relative to the actual microstructure. However, the differences become smaller with increasing film thickness. Therefore, under conditions of a spatially uniform temperature field which simulates furnace heating durability test, grading is likely to accelerate delamination growth based on our hypothesis regarding the importance of the shear stress component. The assessment of the desirability of grading the bond coat under conditions of gradient heating remains to be addressed, however.

It is important to note that the differences predicted by the homogenized and non-homogenized higher-order theory analyses occur in the top coat which has been modeled as *homogeneous.* The two approches are expected to produce different results in the graded region, as readily observed in the preceding contour plots. The differences observed within the homogeneous top coat point to the micro-macrostructural interaction which is not explicitly taken into account in the analysis based on the homogenized bond coat microstructure.

We end this section by pointing out that in addition to the top/bond coat interface roughness, thermoinelastic parameter mismatch (i.e., thermal expansion, moduli and creep parameter mismatch), and oxide film thickness, additional factors that may affect the spallation mechanism and ultimate failure modes of plasma-sprayed TBCs must be considered. These include top coat porosity [24]; sintering of the top coat during exposure to high temperatures [25], which affects the thermomechanical coating properties [26]; phase transitions occuring in the top and bond coat as well as in the thermally-grown oxide film [27], leading to potential local degradation in the presence of large stresses that develop within the film itself [28]. The effect of the TBC constituent chemical composition on the oxide film adhesion is also an important consideration [29]. Further, the magnitude of the applied thermal gradient and the coating surface temperature, not considered herein, has been demonstrated to have a direct influence on the TBC's durability [30,31]. For example, localized cracks in the top coat's trough region are often present which do not always propagate due to the geometric constraint [23], but may interact with the main crack. Localized damage in the alumina film has also been observed which is consistent with the very high residual stresses induced during the thermal cooldown predicted by our analysis [32]. The above observations make it difficult to conclude with a good measure of confidence that the ultimate spallation of the top coat is exclusively governed by a critical thickness of the thermally grown oxide film, as pointed out by some investigators [33]. In view of the complex state of stress induced by the oxide film, it is very likely that the critical spallation event depends on the particular material system in which a particular failure event becomes dominant.

7 CONCLUSIONS

The results generated using the Higher-Order Theory for Functionally Graded Materials indicate that, under spatially-uniform cyclic heating, the use of heterogeneous, two-phase bond coats to reduce the top/bond coat thermal expansion mismatch in plasma-sprayed TBCs is likely to accelerate the growth of horizontal cracks in the top coat at, or just above, the rough interface's crests. These cracks are thought to be initiated by the relatively large normal stress at the crests of the rough top/bond coat interface which becomes tensile upon cooldown due to stress relaxation at elevated temperatures. According to a proposed model, the growth of these cracks, which is driven by the change in the sign of the normal through-thickness stress in the trough region of the top/bond coat interface caused by an evolving interfacial oxide film, ultimately leads to top coat spallation. Our analysis predicts that the use of heterogeneous bond coats, while *initially reducing* the normal stress field at the tip of a horizontal crack above the rough interface's crest, *increases* the thus-far neglected shear stress field at the crack tip, thereby providing the necessary force for mixed-mode crack growth. This is further amplified by the oxide film. Heterogeneous bond coats also accelerate the evolution of the tensile normal stress in the rough interface's trough region, thereby potentially providing additional energy for crack extension with sufficient oxide film thickness. The overall effect of bond coat heterogeneity is similar to that of the oxide film in pure bond coat TBCs, albeit not as dramatic. Our results also suggest that the actual mechanism of crack growth will likely involve inelastic deformation of the top coat which experiences inelastic strain reversal during thermal cycling, potentially facilitating crack growth and microcrack coalescence.

In addition, the results indicate that micro-macrostructural coupling which explicitly accounts for particle-particle and particle-interface interactions, and which is an intrinsic feature of the higher-order theory, is important in the analysis of plasma-sprayed TBCs with graded bond coat microstructures. In particular, the extent of the crack-tip normal stress field reduction was overestimated by the analysis based on the homogenized properties of the graded bond coat microstructure relative to the actual microstructure. The extent of the shear stress magnification was also overestimated by the analysis based on the homogenized properties. The micro-macrostructural coupling effects propagate sufficiently far into the top coat, modeled here as homogeneous, to affect the crack-tip stress fields in the immediate vicinity of the top/graded bond coat interface. These results suggest that the porous microstructure of plasma-sprayed coatings, characterized by microcracks and splats of specific size, should be explicitly taken into account in order to gain a better understanding of the horizontal delamination growth.

8 REFERENCES

1. Strangman, T. E. (1985). Thermal Barrier Coatings for Turbine Airfoils, *Thin Solid Films*, **127**, 93-105.

2. Sheffler, K. D. and Gupta, D. K. (1988). Current Status and Future Trends in Turbine Application of Thermal Barrier Coatings, *ASME J. Engineering For Gas Turbines and Power*, **110**, 605-609.

3. DeMassi-Marcin, J. T., Sheffler, K. D., and Bose, S. (1990). Mechanisms of Degradation and Failure in a Plasma-Deposited Thermal Barrier Coating, *J. Engineering for Gas Turbines and Power*, **112**, 521-526.

4. Hass, D. D., Slifka, A. J., and Wadley, H. N. G. (2001). Low Thermal Conductivity Vapor Deposited Zirconia Microstructures, *Acta Materialia,* **49**, 973-983..

5. Miller, R. A. and Lowell, C. E. (1982). Failure Mechanisms of Thermal Barrier Coatings Exposed to Elevated Temperatures, *Thin Solid Films*, **95**, 265-273.

6. Evans, A. G., Crumley, G. B., and Demaray, R. R. (1983). On the Mechanical Behavior of Brittle Coatings and Layers, *Oxidation of Metals*, **20**(5/6), 193-216.

7. Chang, G.C., Phucharoen, W., and Miller, R. A. (1987). Behavior of Thermal Barrier Coatings for Advanced Gas Turbine Blades, *Surface and Coatings Technology,* **30**, 13-28.

8. Chang, G.C., Phucharoen, W., and Miller, R. A. (1987). Thermal Expansion Mismatch and Plasticity in Thermal Barrier Coatings, *Turbine Engine Hot Section Technology 1987, NASA CP 2493*, 357-368.

9. Petrus, G. J. and Ferguson, B. L. (1997). A Software Tool to Design Thermal Barrier Coatings: A Technical Note, *J. Thermal Spray Technology*, **6**(1), 29-34. See also: NASA Phase I Final Report, Project No. 93-1-04-23-8477.

10. Freborg, A. M., Ferguson, B. L., Brindley, W. J., and Petrus, G. J. (1998). Modeling Oxidation Induced Stresses in Thermal Barrier Coatings, *Materials Science & Engineering*, **A245**, 182-190.

11. Pindera, M-J., Aboudi, J., and Arnold, S. M. (2000). The Effect of Interface Roughness and Oxide Film Thickness on the Inelastic Response of Thermal Barrier Coatings to Thermal Cycling, *Materials Science and Engineering*, **A284**, 158-175.

12. Ali, M. Y., Nusier, S. Q., and Newaz, G. M. (2001). Mechanics of Damage Initiation and Growth in a TBC/Superalloy System, *Int. J. Solids & Structures*, 38, 3329-3340.

13. Brindley, W. J., Miller, R. A., and Aikin, B. J. (1998). Improved Bond-Coat Layers for Thermal-Barrier Coatings, *NASA Tech Briefs*, August 1998, 63-65.

14. Lee, W. Y., Stinton, D. P., Berndt, C. C., Erdogan, F., Lee, Y-D., and Mutasim, Z. (1996). Concept of Functionally Graded Materials for Advanced Thermal Barrier Coating Applications, *J. Amer. Ceram. Soc.* **79**(12), 3003-3012.

15. Zhu, D., Ghosn, L. J., and Miller, R. A. (1998). Effects of Layer-Graded Bond Coats on Edge Stress Concentration and Oxidation Behavior of Thermal Barrier Coatings, *NASA TM 1998-208505*, Lewis Research Center, Cleveland, OH.

16. Aboudi, J., Pindera, M-J., and Arnold, S. M. (1996). Thermoelastic Theory for the Response of Materials Functionally Graded in Two Directions, *Int. J. Solids & Structures*, **33**(7), 931-966.

17. Aboudi, J., Pindera, M-J., and Arnold, S. M. (1996). Thermoplasticity Theory for Bidirectionally Functionally Graded Materials, *J. Thermal Stresses*, **19**, 809-861.

18. Aboudi, J., Pindera, M-J., and Arnold, S. M. (1999). Higher-Order Theory for Functionally Graded Materials, *Composites: Part B (Engineering)*, **30**(8), 777-832.

19. Aboudi, J. (1995). Micromechanical Analysis of Thermo-Inelastic Multiphase Short-Fiber Composites, *Composites Engineering*, **5**(7), 839-850.

20. Pindera, M-J., Aboudi, J., and Arnold, S. M. (1998). Thermomechanical Analysis of Functionally Graded Thermal Barrier Coatings with Different Microstructural Scales, *J. American Ceramics Society,* **81**(6), 1525-36.

21. Crossman, F. W., Karlak, R. K., and Barnett, D. M. (1974). Creep of B/Al Composites as Influenced by Residual Stress, Bond Strength, and Fiber Packing Geometry, in *Failure Modes in Composites II*, pp. 8-31, TMS of AIME Publication, New York.

22. Crossman, F. W. and Karlak, R. K. (1976). Multiaxial Creep of Metal Matrix Fiber Reinforced Composites, in *Failure Modes in Composites III*, pp. 260-287, TMS of AIME Publication, New York.

23. Singh, J. P., Nair, B. G., Renusch, D. P., Sutaria, M. P., and Grimsditch., M. H. (2001). Damage Evolution and Stress Analysis in Zirconia Thermal Barrier Coatings During Cyclic and Isothermal Oxidation, *J. Amer. Ceram. Soc.* **84**(10), 2385-2393.

24. Funke, C., Mailand, J. C., Siebert, B., Vassen, R., and Stover, D. (1997). Characterization of ZrO_2-7 wt. % Thermal Barrier Coatings with Different Porosities and FEM Analysis of Stress Redistribution During Thermal Cycling of TBCs, *Surface and Coatings Technology*, **94/95**, 106-11.

25. Zhu, D. and Miller, R. A. (1998). Sintering and Creep Behavior of Plasma-Sprayed Zirconia and Hafnia Based Thermal Barrier Coatings, *NASA TM 1998-208406*, NASA Glenn Research Center, Cleveland, OH. August 1998.

26. Zhu, D. and Miller, R. A. (2000). Thermal Conductivity and Elastic Modulus Evolution of Thermal Barrier Coatings Under High Heat Flux Conditions, *J. Thermal Spray Technology*, **9**(2), 175-180.

27. Alperine, S. and Lelait, L. (1994). Microstructural Investigations of Plasma-Sprayed Yttria Partially Stabilized Zirconia TBC, *ASME J. Engineering for Gas Turbines and Power*, **116**, 258-265.

28. Christensen, R. J., Lipkin, D. M., and Clarke, D. R. (1996). Nondestructive Evaluation of the Oxidation Stresses Through Thermal Barrier Coatings Using Cr^{3+} Piezospectroscopy, *Appl. Phys. Letters*, **69**(24), 3754-3756.

29. Pint, B. A., Wright, I. G., Lee, W. Y., Zhang, Y., Prussner, K., and Alexander, K. B. (1998). Substrate and Bond Coat Compositions: Factors Affecting Alumina Scale Adhesion, *Materials Science and Engineering*, **A245**, 201-211.

30. Koolloos, M. F., Liempd, G. G., and Houben, J. M. (1998). Effect of Local Thermal Shock Load on Plasma Sprayed Thermal Barrier Coatings, *Surface Engineering*, **14**(2), 144-148.

31. Koolloos, M. F. and Houben, J. M. (1998). Failure Mechanisms During Thermal Cycling and the Effect of a Pre-Oxidized NiCrAlY Bond Coat, in *Proceedings of ASM International Materials Solutions 98*, Rosemont, Illinois, 12-15, October, 1998.

32. Haynes, J. A., Ferber, M. K., and Porter, W. D. (2000). Thermal Cycling Behavior of Plasma-Sprayed Thermal Barrier Coatings with Various MCrAlX Bond Coats, *J. Thermal Spray Technology*, **9**(1), pp. 38-48.

33. Thompson, J. A. and Clyne, T. W. (2001). The Effect of Heat Treatment on the Stiffness of Zirconia Top Coats in Plasam-Sprayed TBCs, *Acta Materialia*, **49**, pp. 1565-1575.

Table 1. Two competing thermal barrier coatings for gas turbine applications.

Characteristics	**Plasma-Sprayed TBCs**	**EB PVD TBCs**
TC microstructure	pancake-like: splats, porosities	columnar
Conductivity	low: 0.8-1.0 W/mK	higher: 1.6-1.8 W/mk
Elastic moduli	anisotropic: out-of-plane compliant	anisotropic: in-plane compliant
TC/BC interface	rough	smoother
TC/BC bond	weak	stronger
Spallation location	at or above TC/TGO film interface within TGO film (?)	at BC/TGO film interface

Table 2. Thermoelastic and creep material parameters of the zirconia top coat (after Petrus and Ferguson [5]).

Temperature	**E** (GPa)	$\boldsymbol{\nu}$	$\boldsymbol{\alpha}$ (10^{-6}/°C)	**A** (MPa$^{-n}/s$)	**n**
1200°C	25.4	0.33	12.5	1.85×10^{-7}	3.0
1100°C	25.4	0.33	12.1	7.40×10^{-8}	3.0
1000°C	25.4	0.33	11.8	2.57×10^{-8}	3.0
900°C	25.4	0.33	11.4	7.42×10^{-9}	2.0
800°C	25.4	0.33	11.0	1.70×10^{-9}	2.0
700°C	25.4	0.33	10.6	2.89×10^{-10}	1.0
500°C	25.4	0.33	9.8	2.10×10^{-12}	1.0
10°C	25.4	0.33	7.6	2.01×10^{-30}	1.0

Table 3. Thermoelastic and creep material parameters of the NiCrAlY bond coat (after Petrus and Ferguson [5]).

Temperature	**E** (GPa)	$\boldsymbol{\nu}$	$\boldsymbol{\alpha}$ (10^{-6}/°C)	**A** (MPa$^{-n}/s$)	**n**
1200°C	156.0	0.27	14.4	7.40×10^{-6}	3.0
1100°C	156.0	0.27	14.2	1.17×10^{-6}	3.0
1000°C	156.0	0.27	14.0	1.37×10^{-7}	3.0
900°C	156.0	0.27	13.8	1.14×10^{-8}	2.0
800°C	156.0	0.27	13.6	5.90×10^{-10}	2.0
700°C	156.0	0.27	13.4	1.66×10^{-11}	1.0
500°C	156.0	0.27	13.0	8.20×10^{-16}	1.0
10°C	156.0	0.27	12.0	4.39×10^{-40}	1.0

Table 4. Thermoelastic and creep material parameters of the Ni substrate (after Petrus and Ferguson [5]).

Temperature	**E** (GPa)	$\boldsymbol{\nu}$	$\boldsymbol{\alpha}$ (10^{-6}/°C)	**A** (MPa^{-n}/s)	**n**
1200°C	156.0	0.27	19.3	2.25×10^{-9}	3.0
1100°C	156.0	0.27	18.8	4.36×10^{-10}	3.0
1000°C	156.0	0.27	17.8	3.08×10^{-10}	3.0
900°C	156.0	0.27	16.9	1.79×10^{-10}	2.0
800°C	156.0	0.27	15.9	5.13×10^{-11}	2.0
700°C	156.0	0.27	15.2	2.28×10^{-29}	1.0
500°C	156.0	0.27	14.4	1.00×10^{-34}	1.0
10°C	156.0	0.27	12.0	4.85×10^{-36}	1.0

Table 5. Thermoelastic material parameters of the Al_3O_2 film/particles.

Temperature	**E** (GPa)	$\boldsymbol{\nu}$	$\boldsymbol{\alpha}$ (10^{-6}/°C)	**A** (MPa^{-n}/s)	**n**
1200°C → 0°C	380.0	0.26	8.6	–	–

Table 6. Homogenized Young's moduli of the heterogeneous bond coat as a function of the alumina inclusion volume content and temperature.

E (GPa)					
Temperature	$v_f = 0.10$	$v_f = 0.20$	$v_f = 0.30$	$v_f = 0.40$	$v_f = 0.50$
1200°C → 10°C	169.9	187.1	206.7	228.5	252.2

Table 7. Homogenized Poisson's ratios of the heterogeneous bond coat as a function of the alumina inclusion volume content and temperature.

$\boldsymbol{\nu}$					
Temperature	$v_f = 0.10$	$v_f = 0.20$	$v_f = 0.30$	$v_f = 0.40$	$v_f = 0.50$
1200°C → 10°C	0.266	0.262	0.258	0.254	0.251

Table 8. Homogenized thermal expansion coefficients of the heterogeneous bond coat as a function of the alumina inclusion volume content and temperature.

$\boldsymbol{\alpha}$ (10^{-6}/°C)					
Temperature	$v_f = 0.10$	$v_f = 0.20$	$v_f = 0.30$	$v_f = 0.40$	$v_f = 0.50$
1200°C	13.67	12.92	12.19	11.49	10.82
1100°C	13.49	12.77	12.06	11.38	10.73
1000°C	13.32	12.61	11.93	11.27	10.64
900°C	13.14	12.46	11.80	11.16	10.55
800°C	12.96	12.31	11.67	11.05	10.47
700°C	12.78	12.15	11.54	10.94	10.38
500°C	12.43	11.85	11.27	10.73	10.20
10°C	11.54	11.08	10.62	10.18	9.76

Table 9. Homogenized power-law creep exponents of the heterogeneous bond coat as a function of the alumina inclusion volume content and temperature.

n					
Temperature	$v_f = 0.10$	$v_f = 0.20$	$v_f = 0.30$	$v_f = 0.40$	$v_f = 0.50$
1200°C → 1000°C	3.0	3.0	3.0	3.0	3.0
900°C	2.0	2.0	2.0	2.0	2.0
800°C	1.97	1.95	1.88	1.82	1.86
700°C → 10°C	1.0	1.0	1.0	1.0	1.0

Table 10. Homogenized power-law creep coefficients of the heterogeneous bond coat as a function of the alumina inclusion volume content and temperature.

A (MPa$^{-n}/s$)					
Temperature	$v_f = 0.10$	$v_f = 0.20$	$v_f = 0.30$	$v_f = 0.40$	$v_f = 0.50$
1200°C	5.11×10^{-6}	3.24×10^{-6}	1.87×10^{-6}	5.02×10^{-7}	2.94×10^{-7}
1100°C	8.09×10^{-7}	5.13×10^{-7}	2.96×10^{-7}	7.92×10^{-8}	4.65×10^{-8}
1000°C	9.61×10^{-8}	6.10×10^{-8}	3.52×10^{-8}	9.45×10^{-9}	5.55×10^{-9}
900°C	8.20×10^{-9}	5.59×10^{-9}	3.45×10^{-9}	1.30×10^{-9}	7.99×10^{-10}
800°C	5.05×10^{-10}	4.35×10^{-10}	3.76×10^{-10}	3.17×10^{-10}	1.77×10^{-10}
700°C	1.36×10^{-11}	1.11×10^{-11}	8.78×10^{-12}	6.46×10^{-12}	4.88×10^{-12}
500°C	6.70×10^{-16}	5.48×10^{-16}	4.34×10^{-16}	3.19×10^{-16}	2.41×10^{-16}
10°C	3.59×10^{-40}	2.94×10^{-40}	2.33×10^{-40}	1.71×10^{-40}	1.29×10^{-40}

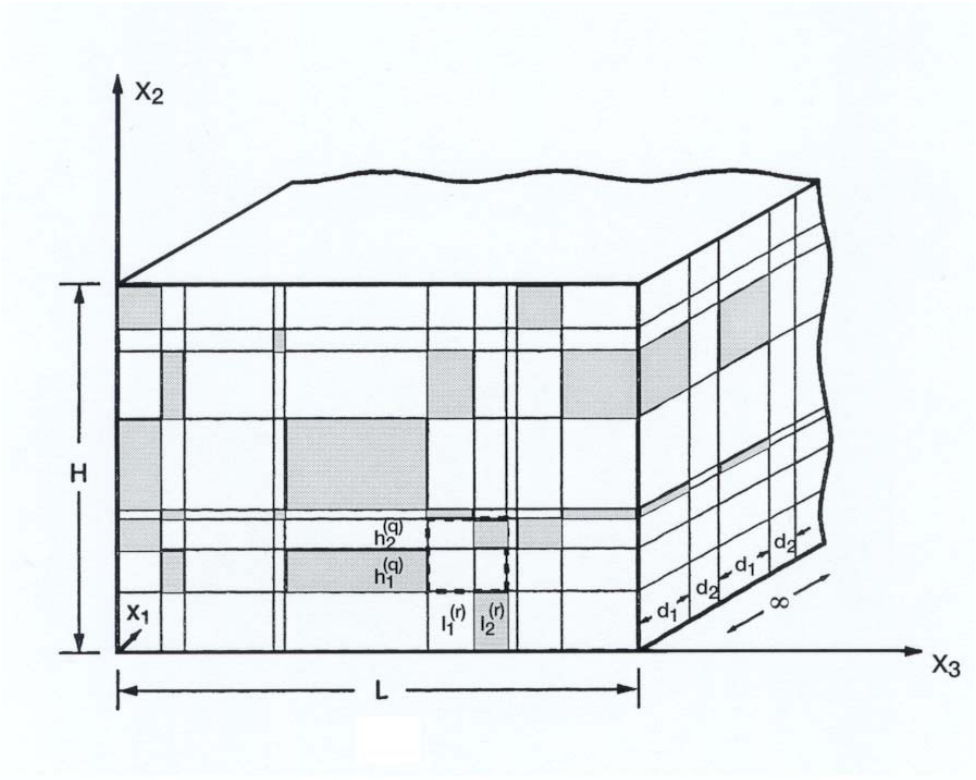

Figure 1. A geometric model of a material functionally graded material in the $x_2 - x_3$ plane with periodicity in the x_1 direction, illustrating the volume discretization employed in the higher-order theory.

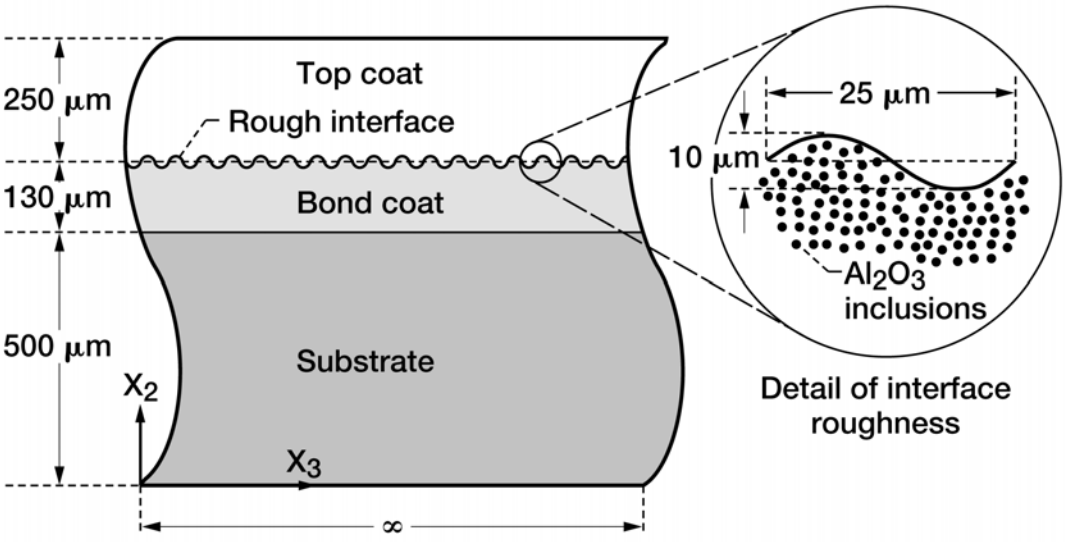

(a) Bond coat with spatially uniform heterogeneous microstructure in the interfacial region.

Figure 2. A TBC system with a sinusoidally-varying top coat/bond coat interface and a heterogeneous bond coat in the interfacial region.

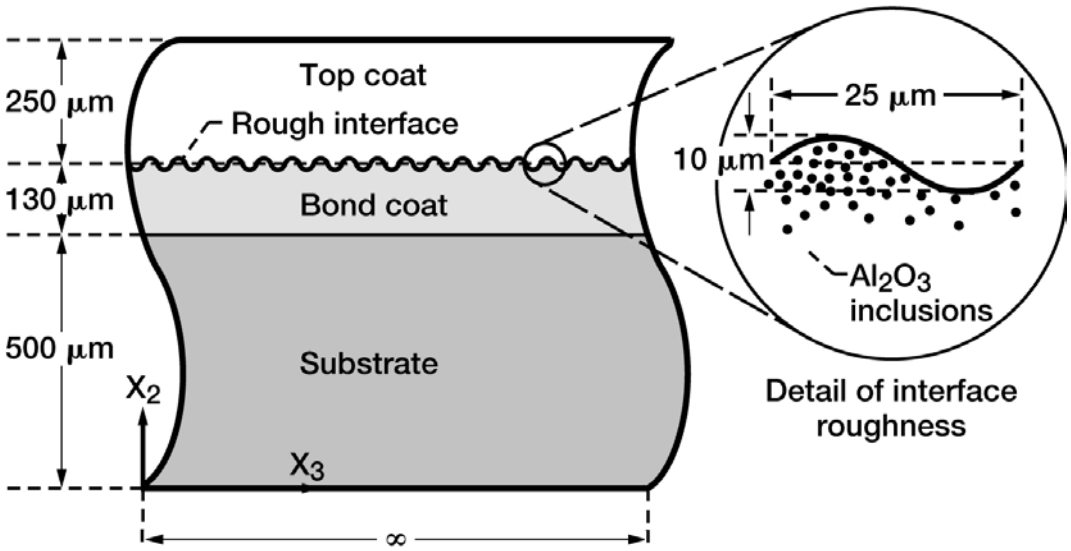

(b) Bond coat with functionally graded heterogenous microstructure in the interfacial region.

Figure 2, cont'd. A TBC system with a sinusoidally-varying top coat/bond coat interface and a heterogeneous bond coat in the interfacial region.

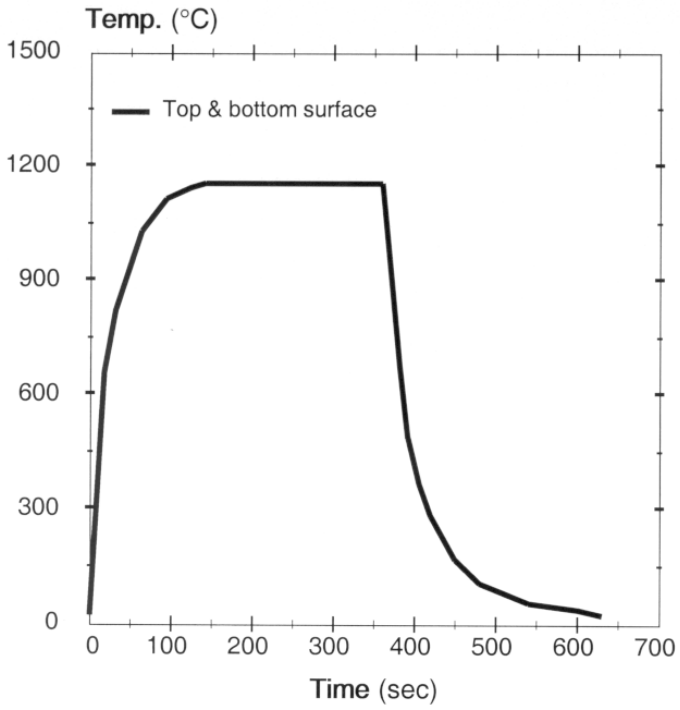

Figure 3. Thermal loading history.

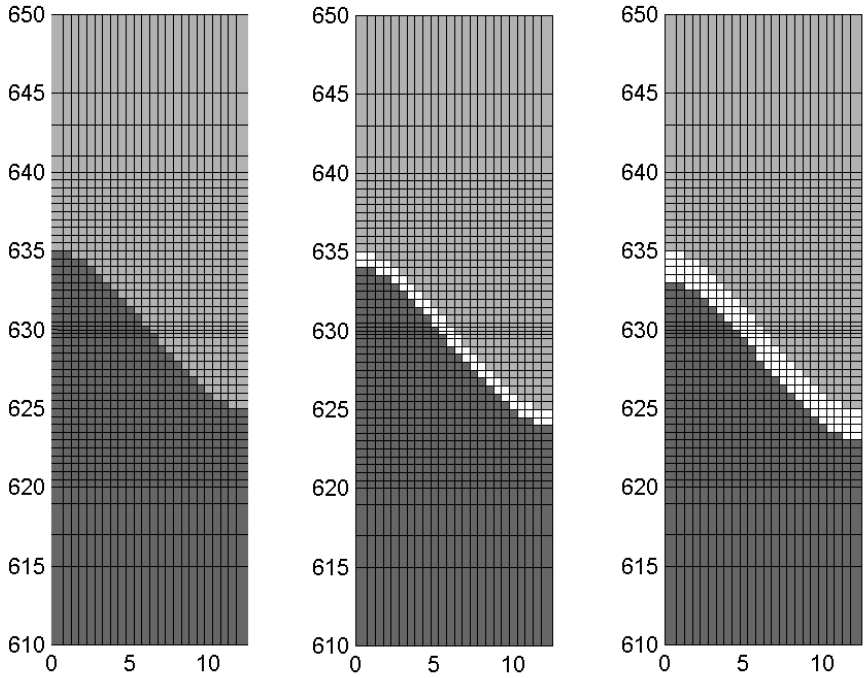

No oxide film (left), 1 micron oxide film (middle), 2 micron oxide film (right)

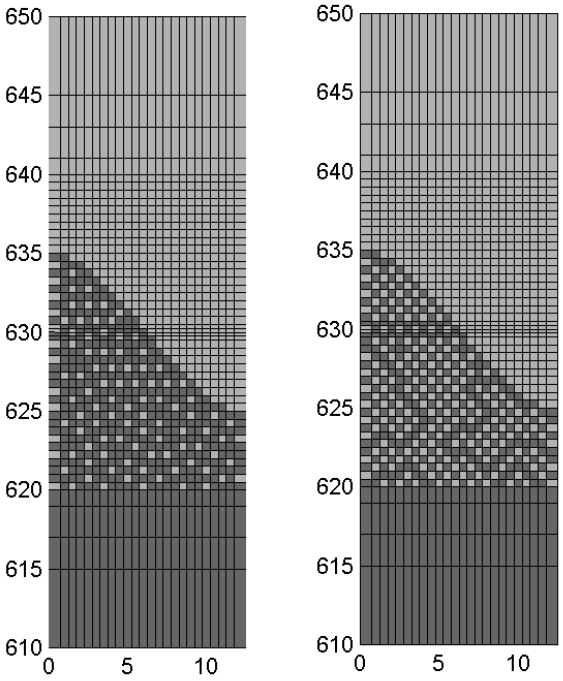

20% alumina content BC (left), 40% alumina content BC (right)

Figure 4(a). Volume discretization of the sinusoidally-varying interface region: pure TBCs with different oxide film thicknesses (top) and TBCs with spatially uniform dispersions of alumina inclusions within the bond coat in the interfacial region (bottom).

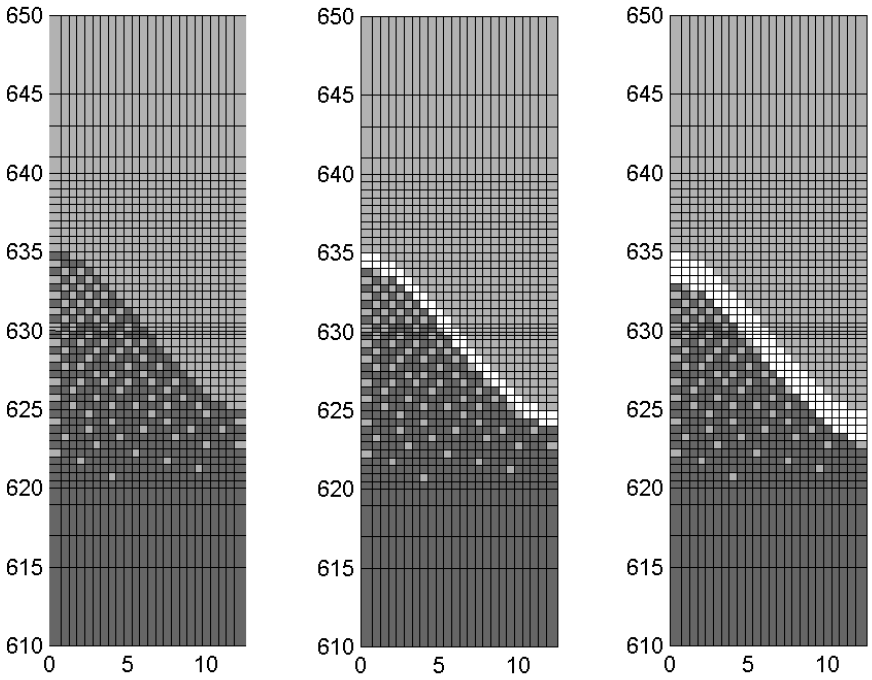

Graded, unhomogenized BCs with 0 (left), 1 (middle), and 2 (right) micron oxide film

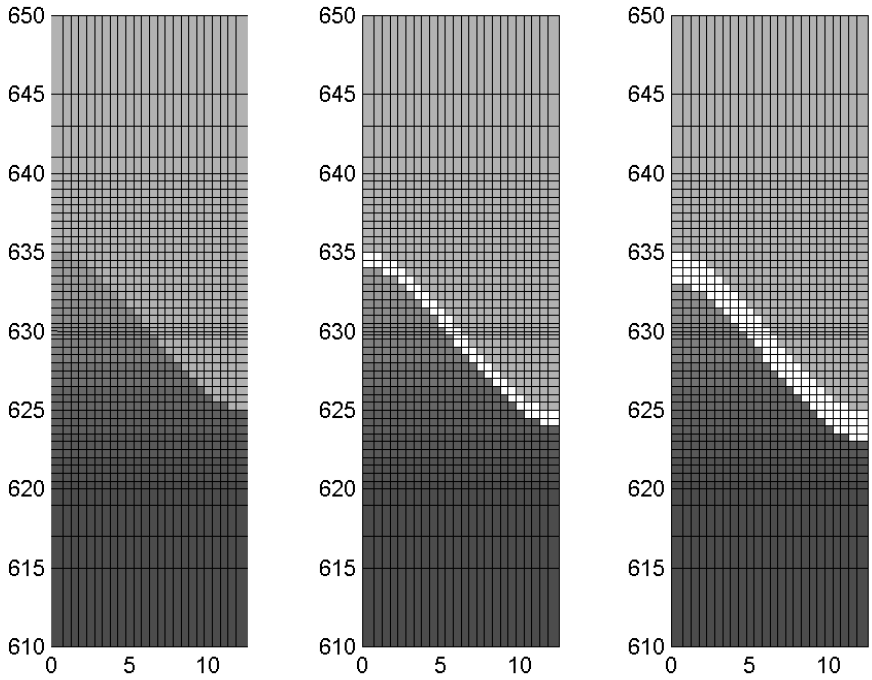

Graded, homogenized BCs with 0 (left), 1 (middle), and 2 (right) micron oxide film

Figure 4(b). Volume discretization of the sinusoidally-varying interface region: TBCs with actual (top) and homogenized (bottom) graded bond coat microstructures and different oxide film thicknesses.

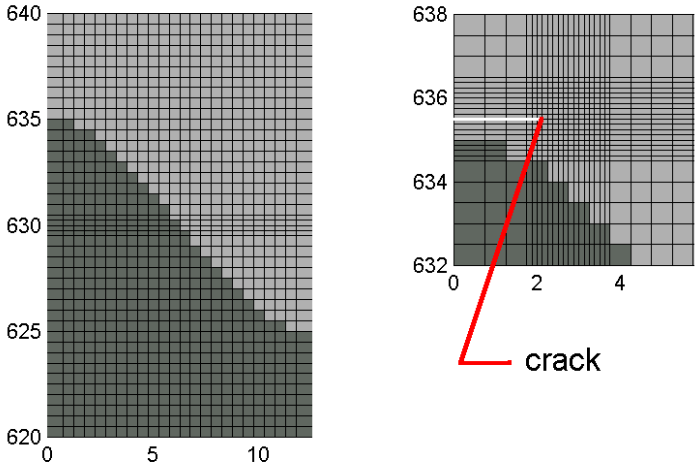

Figure 5. Volume discretization of the sinusoidally-varying interface region in a pure TBC with a horizontal delamination above the interface's crest: pure TBC (left) and a magnified region (right) showing refined mesh around the horizontal crack in the top coat above the crest of the top/bond coat interface.

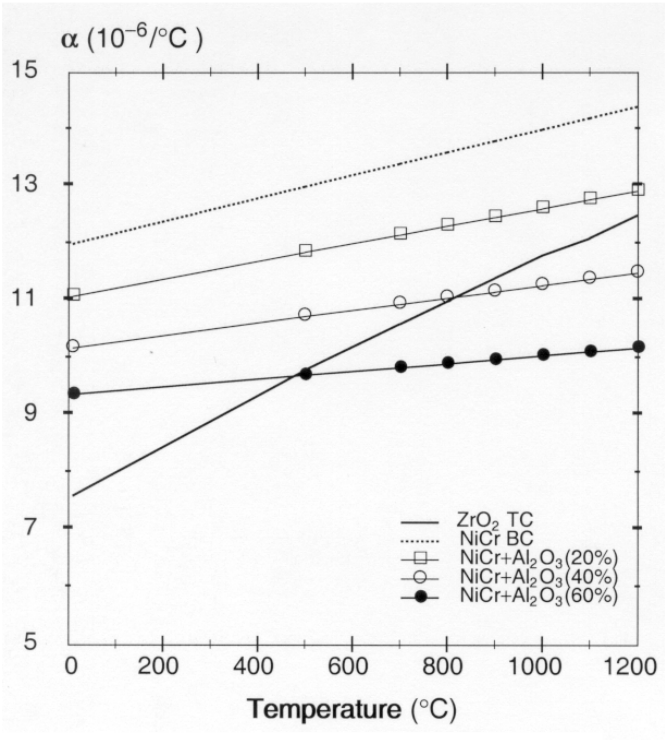

Figure 6. Thermal expansion coefficient vs temperature of pure zirconia, and pure and heterogeneous NiCr-based bond coat material with different alumina particle content.

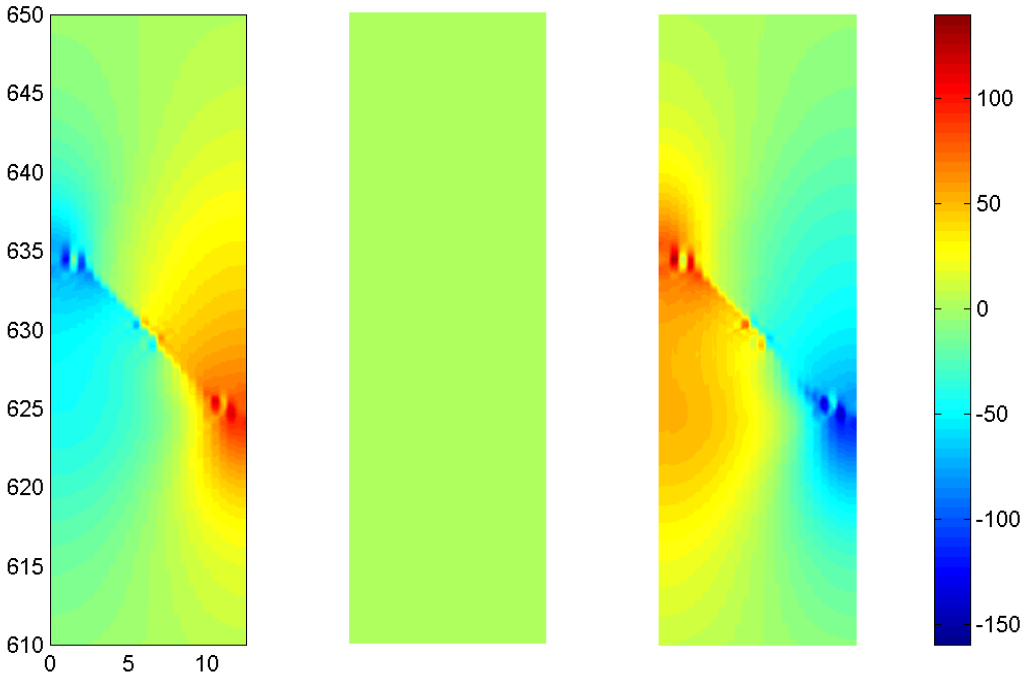

Time = 30 (left), 360 (middle), 630 (right) seconds

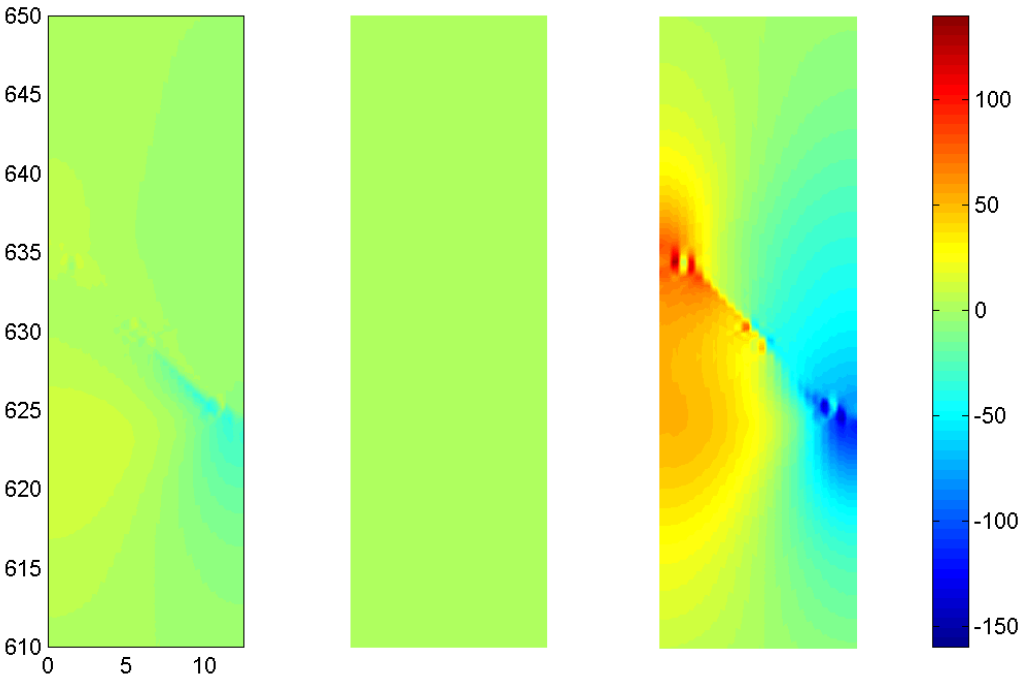

Time = 1290 (left), 1620 (middle), 1890 (right) seconds

Figure 7(a). Evolution of σ_{22} stress distributions with time in the interfacial region of a pure TBC without an oxide film during the first (top) and third (bottom) thermal cycle (colorbar scale in MPa).

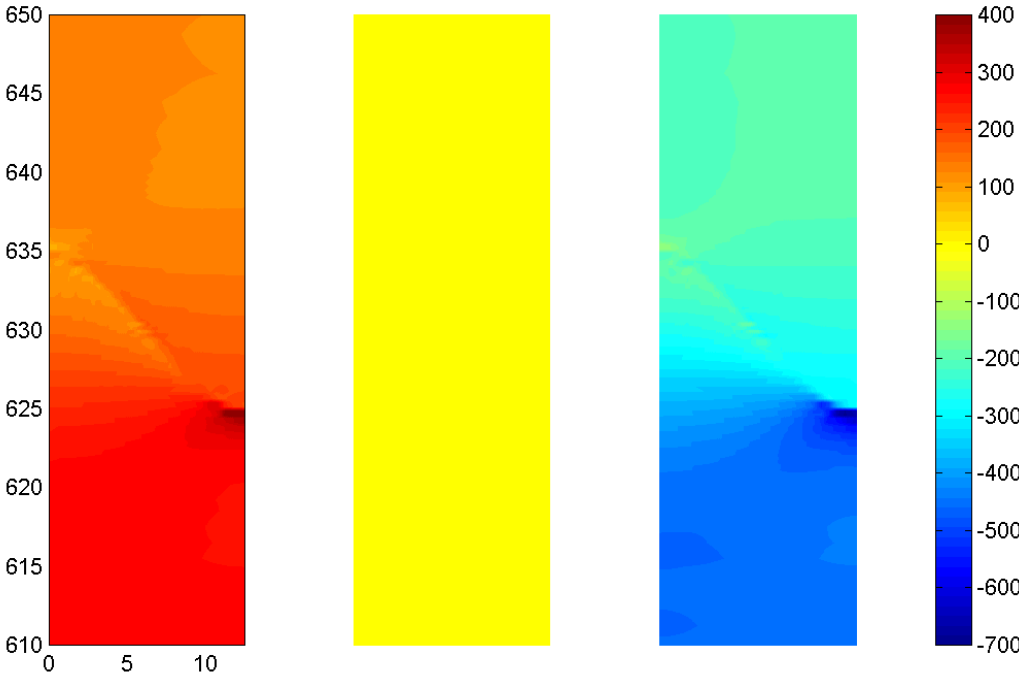

Time = 30 (left), 360 (middle), 630 (right) seconds

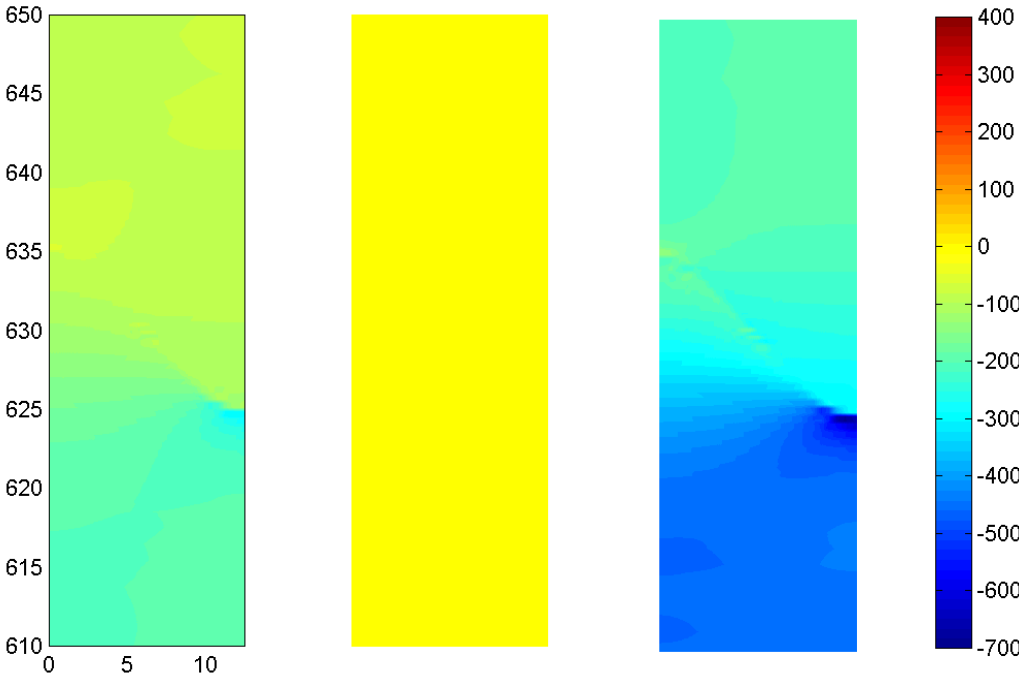

Time = 1290 (left), 1620 (middle), 1890 (right) seconds

Figure 7(b). Evolution of σ_{33} stress distributions with time in the interfacial region of a pure TBC without an oxide film during the first (top) and third (bottom) thermal cycle: (colorbar scale in MPa).

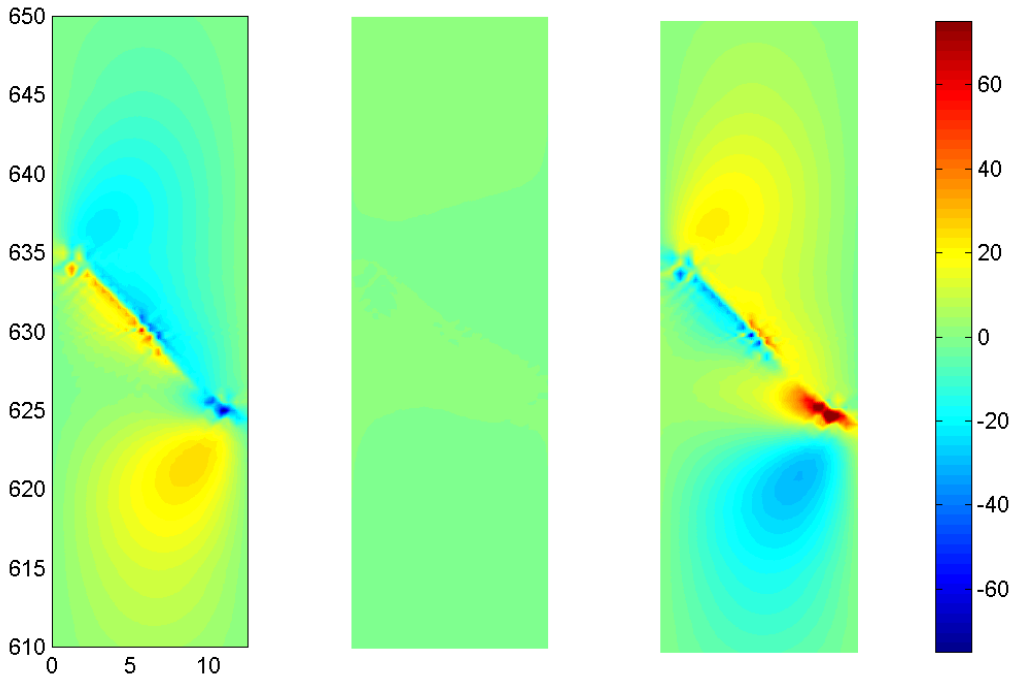

Time = 30 (left), 360 (middle), 630 (right) seconds

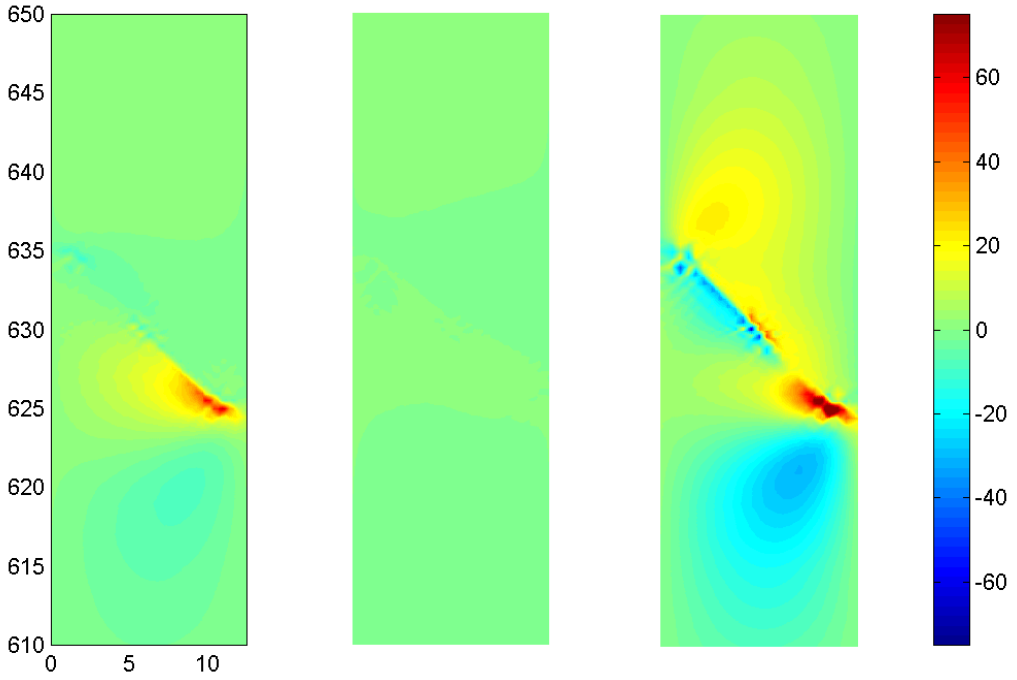

Time = 1290 (left), 1620 (middle), 1890 (right) seconds

Figure 7(c). Evolution of σ_{23} stress distributions with time in the interfacial region of a pure TBC without an oxide film during the first (top) and third (bottom) thermal cycle: (colorbar scale in MPa).

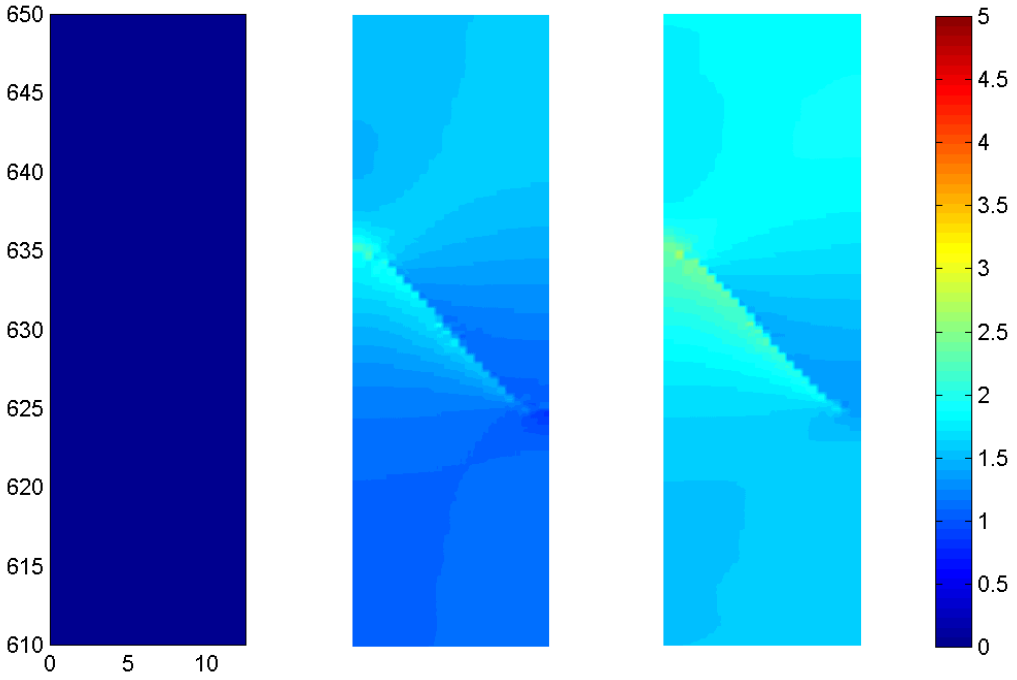

Time = 30 (left), 360 (middle), 630 (right) seconds

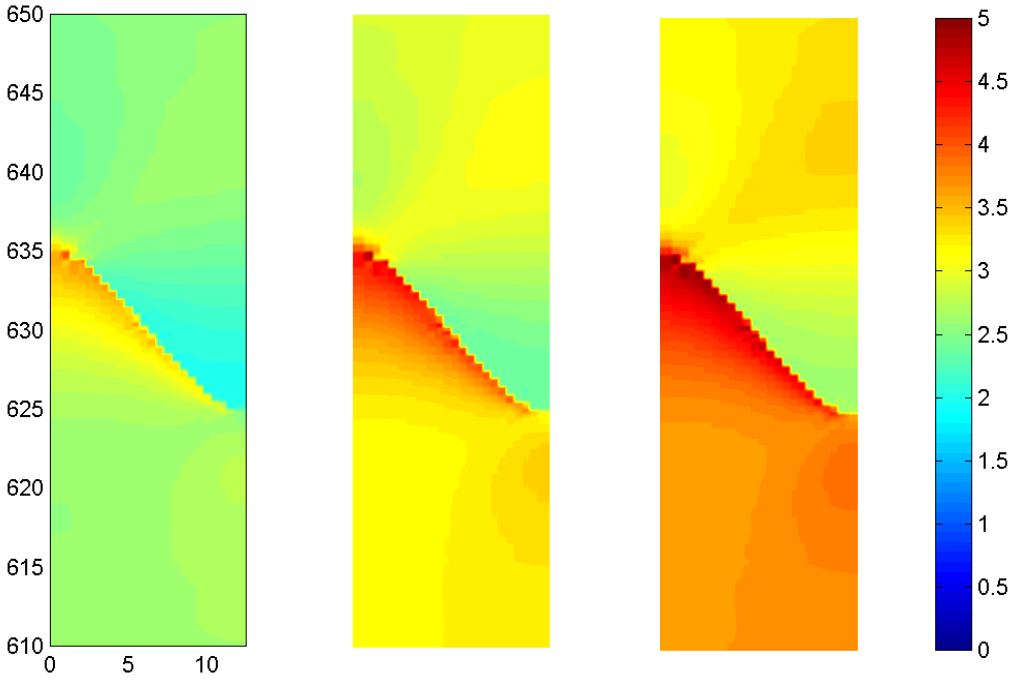

Time = 1290 (left), 1620 (middle), 1890 (right) seconds

Figure 7(d). Evolution of ε_{eff}^{int} inelastic strain distributions with time in the interfacial region of a pure TBC without an oxide film during the first (top) and third (bottom) thermal cycle (colorbar scale in % strain).

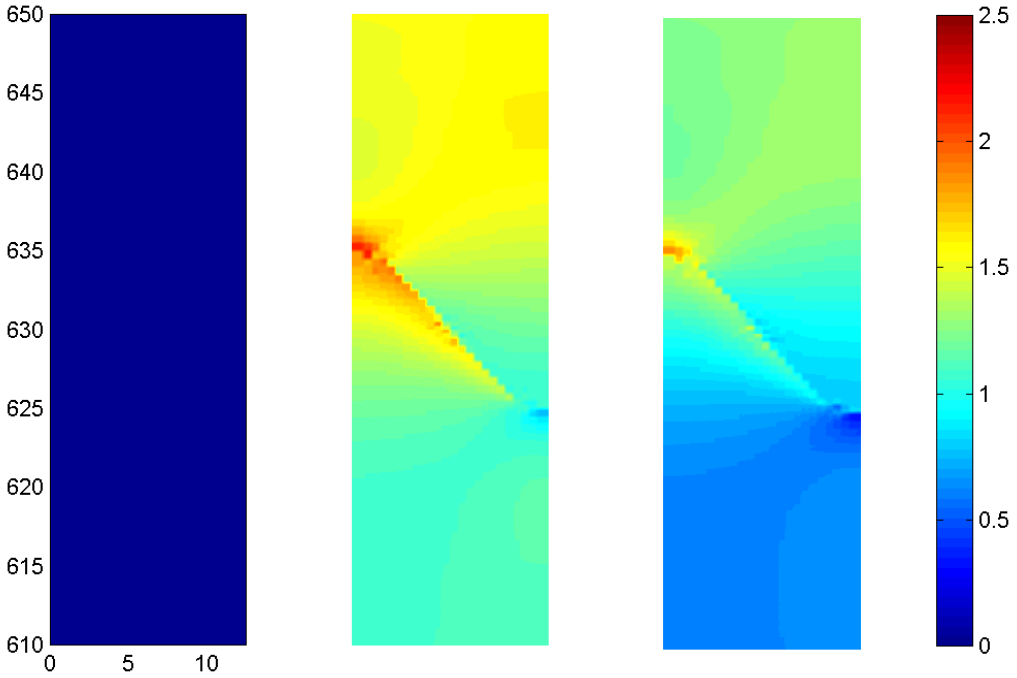

Time = 30 (left), 360 (middle), 630 (right) seconds

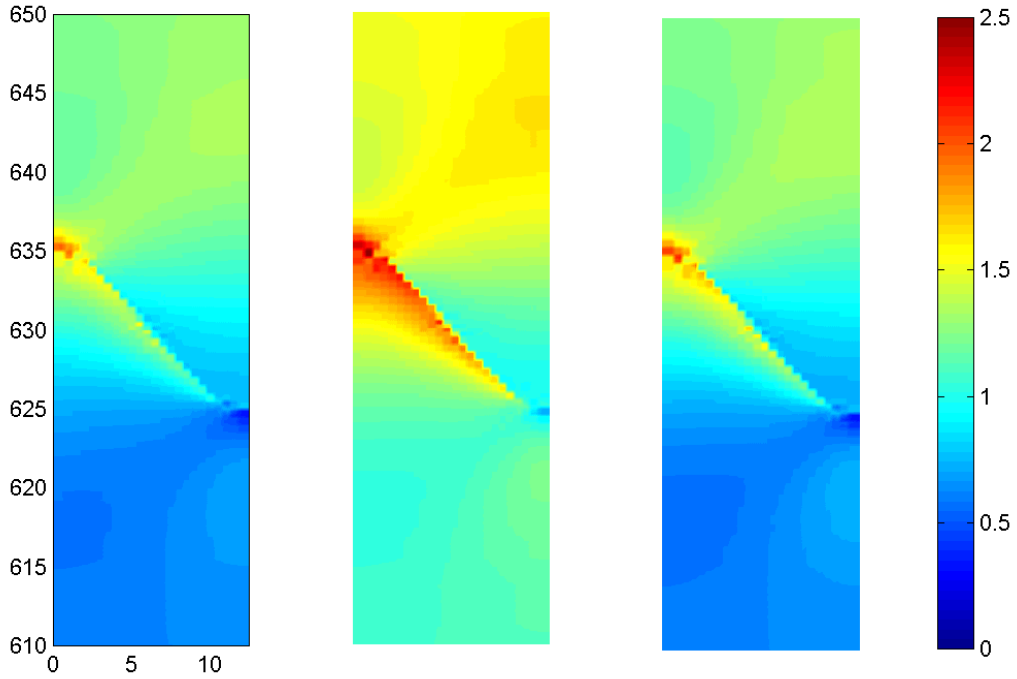

Time = 1290 (left), 1620 (middle), 1890 (right) seconds

Figure 7(e). Evolution of ε_{eff}^{res} inelastic strain distributions with time in the interfacial region of a pure TBC without an oxide film during the first (top) and third (bottom) thermal cycle (colorbar scale in % strain).

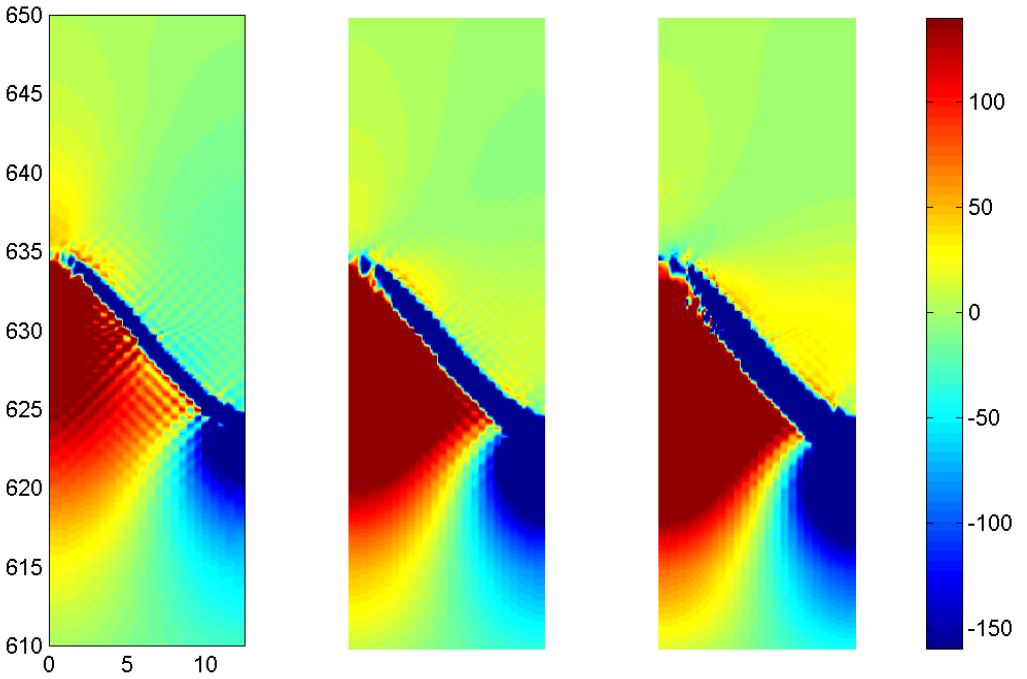

Oxide film thickness = 1 (left), 2 (middle), 3 (right) microns

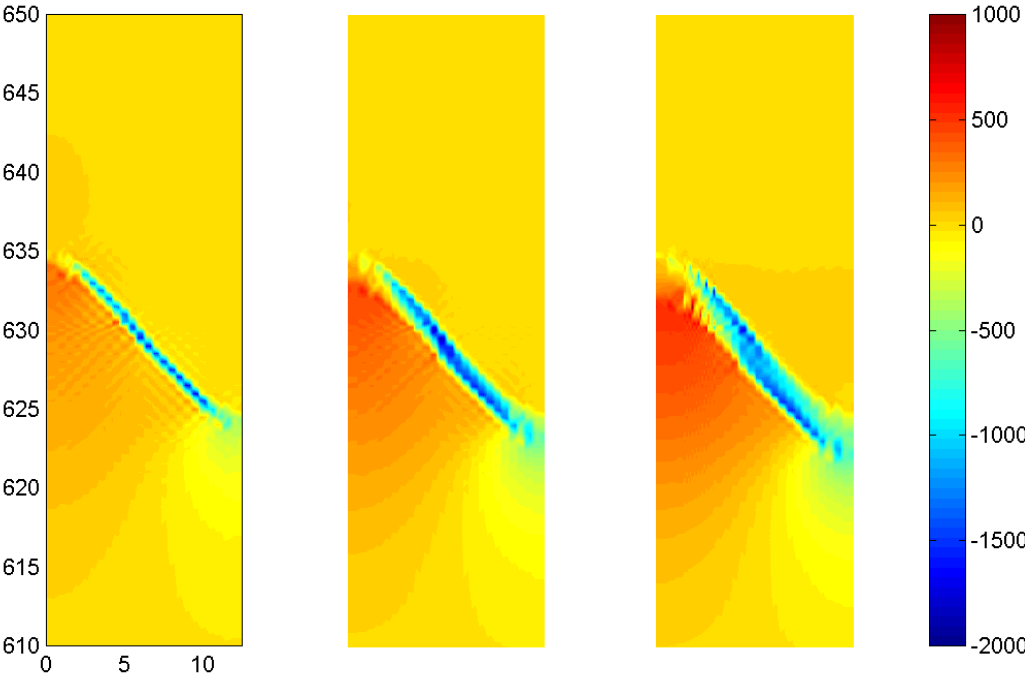

Oxide film thickness = 1 (left), 2 (middle), 3 (right) microns

Figure 8(a). Normal stress σ_{22} distributions in the interfacial region of a pure TBC at the end of the third thermal cycle, illustrating the oxide film thickness influence (colorbar scale in MPa).

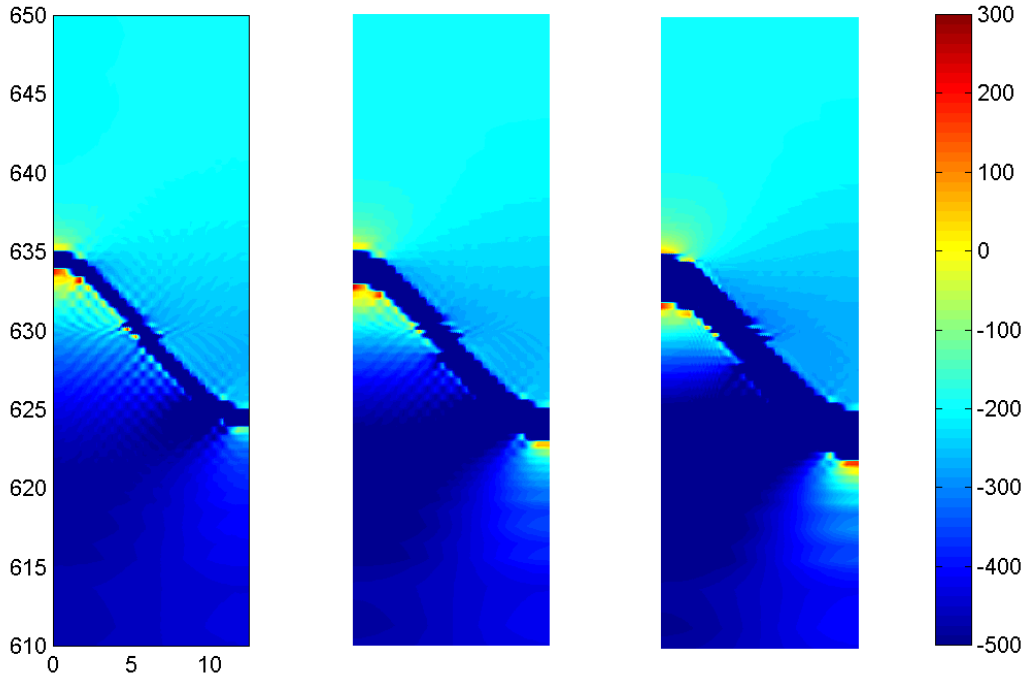

Oxide film thickness = 1 (left), 2 (middle), 3 (right) microns

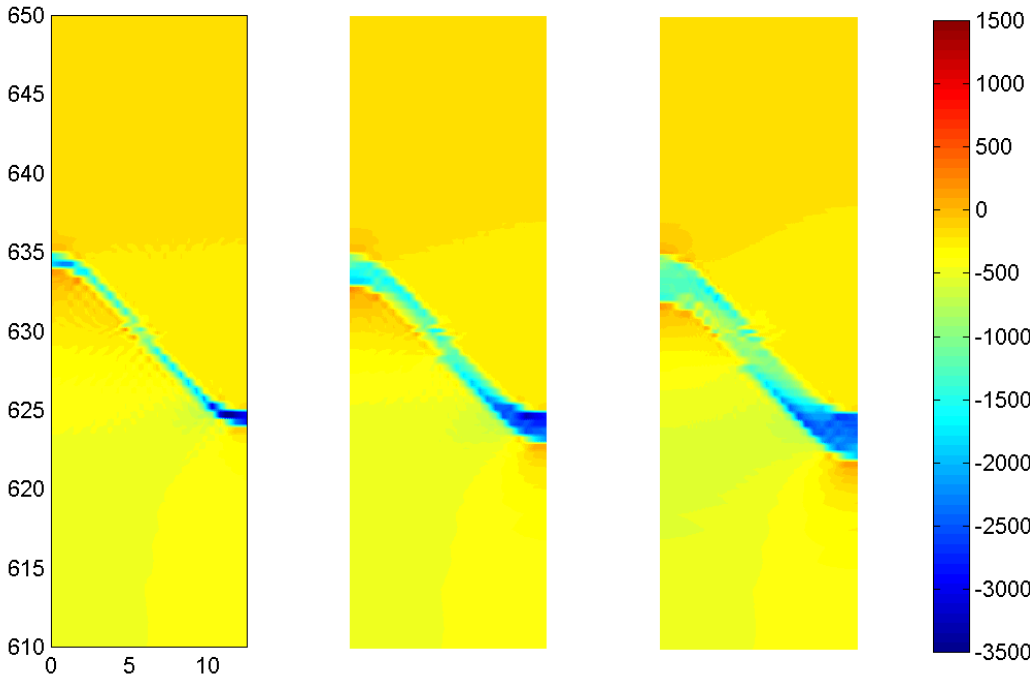

Oxide film thickness = 1 (left), 2 (middle), 3 (right) microns

Figure 8(b). Normal stress σ_{33} distributions in the interfacial region of a pure TBC at the end of the third thermal cycle, illustrating the oxide film thickness influence (colorbar scale in MPa).

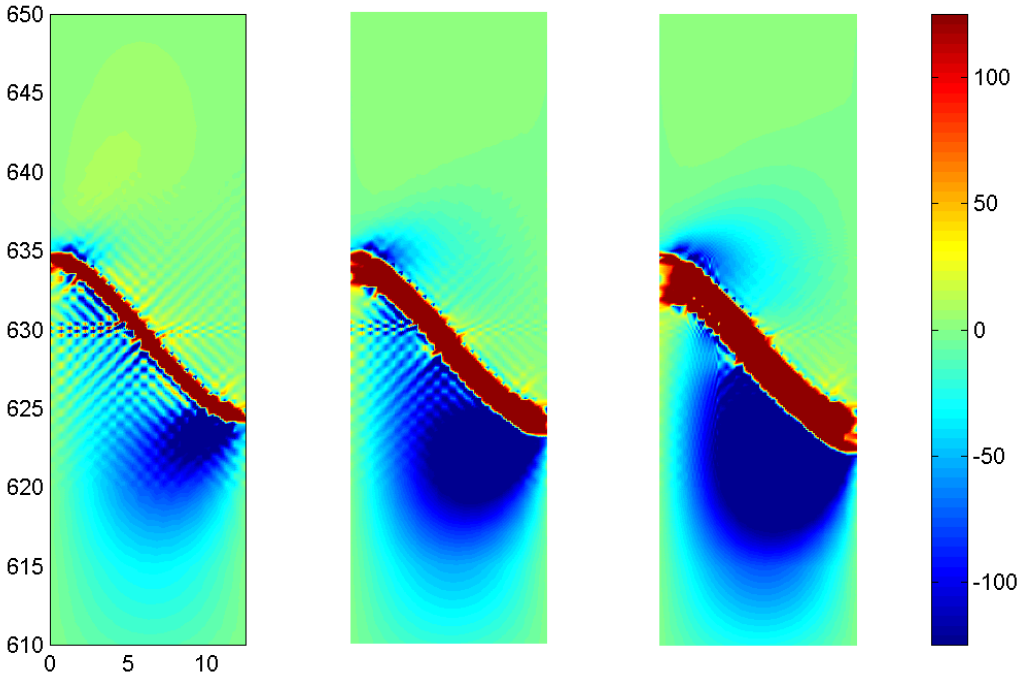

Oxide film thickness = 1 (left), 2 (middle), 3 (right) microns

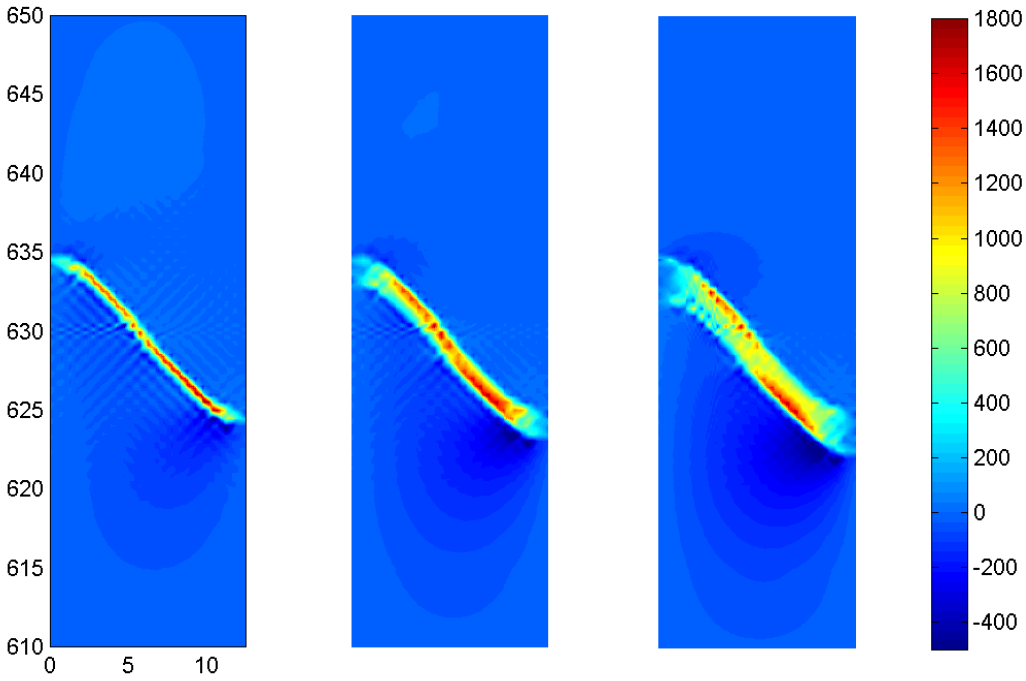

Oxide film thickness = 1 (left), 2 (middle), 3 (right) microns

Figure 8(c). Shear stress σ_{23} distributions in the interfacial region of a pure TBC at the end of the third thermal cycle, illustrating the oxide film thickness influence (colorbar scale in MPa).

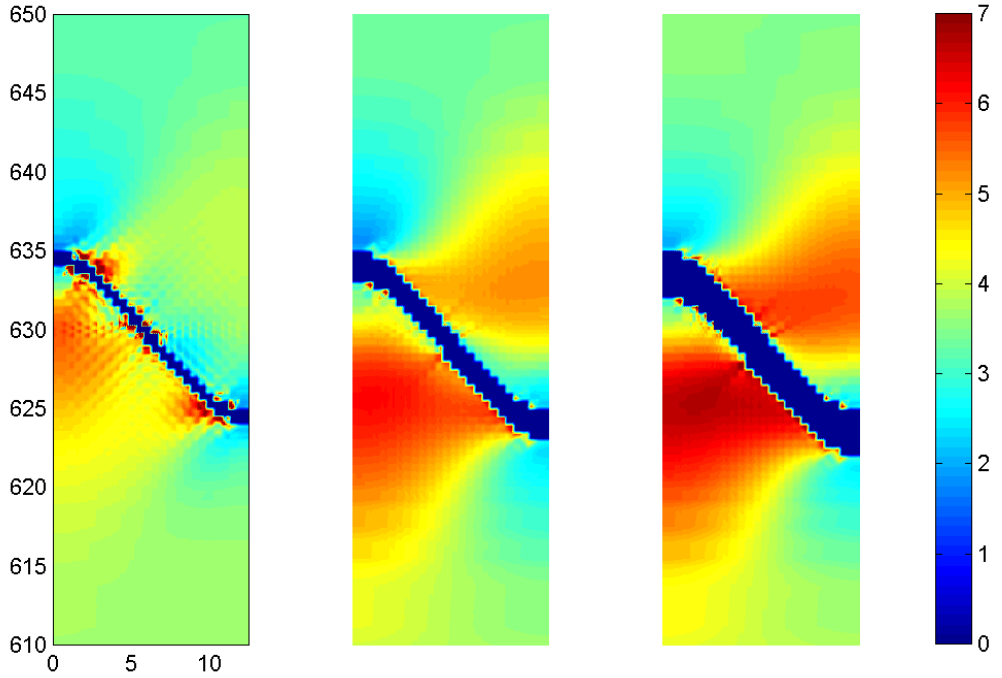

Oxide film thickness = 1 (left), 2 (middle), 3 (right) microns

Figure 8(d). Inelastic strain ε_{eff}^{int} distributions in the interfacial region of a pure TBC at the end of the third thermal cycle, illustrating the oxide film thickness influence (colorbar scale in % strain).

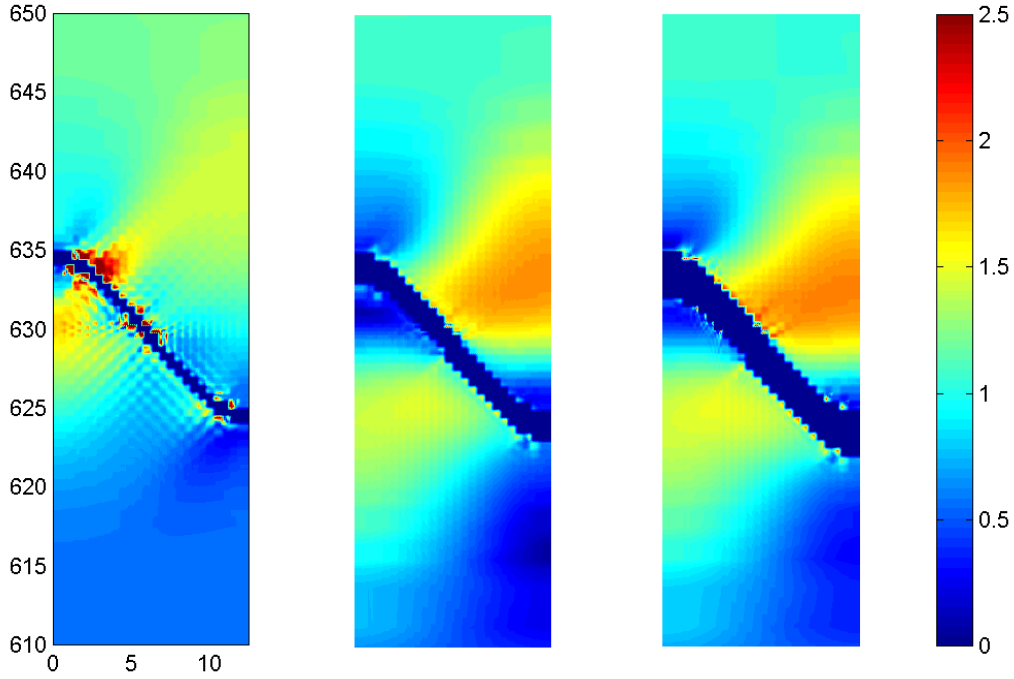

Oxide film thickness = 1 (left), 2 (middle), 3 (right) microns

Figure 8(e). Inelastic strain ε_{eff}^{res} distributions in the interfacial region of a pure TBC at the end of the third thermal cycle, illustrating the oxide film thickness influence (colorbar scale in % strain).

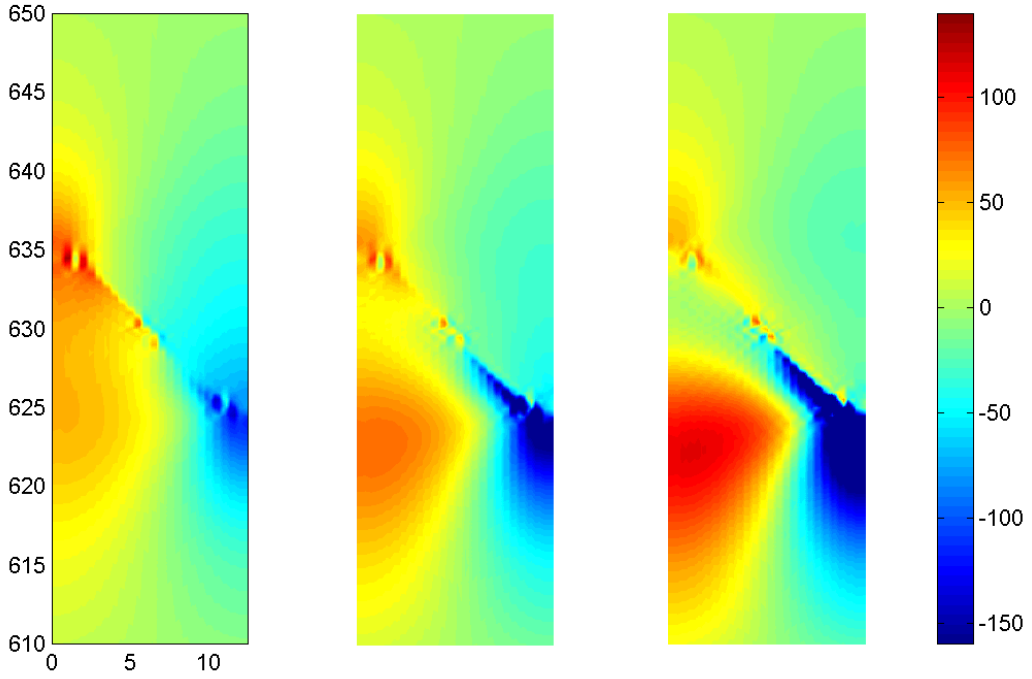

Homogeneous BC (left), 20% alumina BC (middle), 40% alumina BC (right)

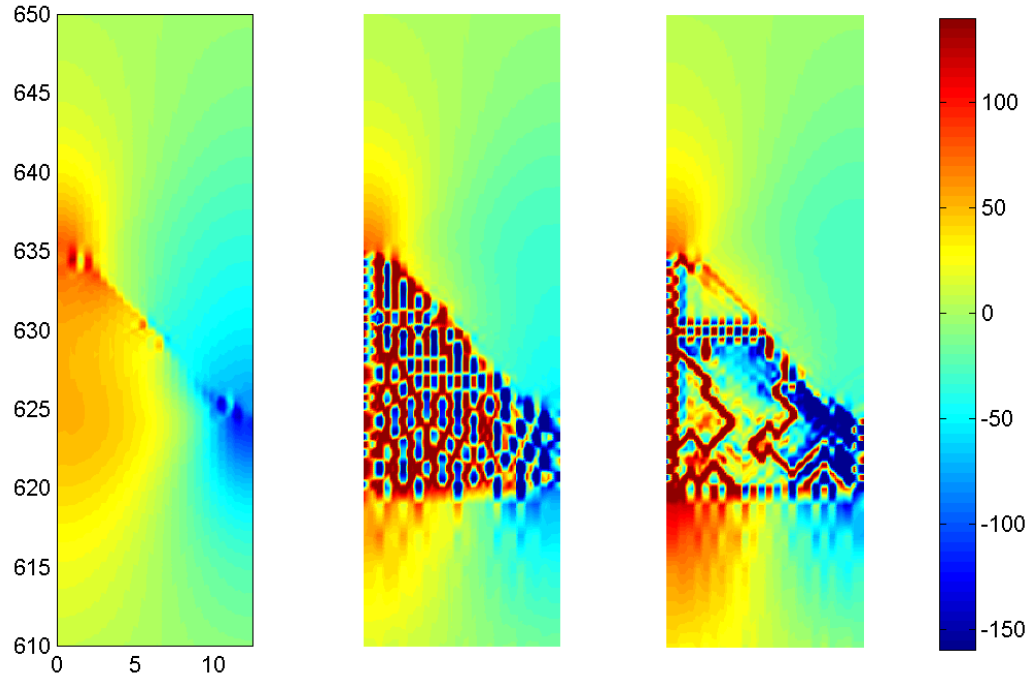

Homogeneous BC (left), 20% alumina BC (middle), 40% alumina BC (right)

Figure 9(a). Normal stress σ_{22} distributions in the interfacial region of a spatially uniform heterogeneous bond coat TBC without an oxide film, with homogenized (top) and actual (bottom) microstructures, at the end of the first thermal cycle illustrating the alumina particle content influence (colorbar scale in MPa).

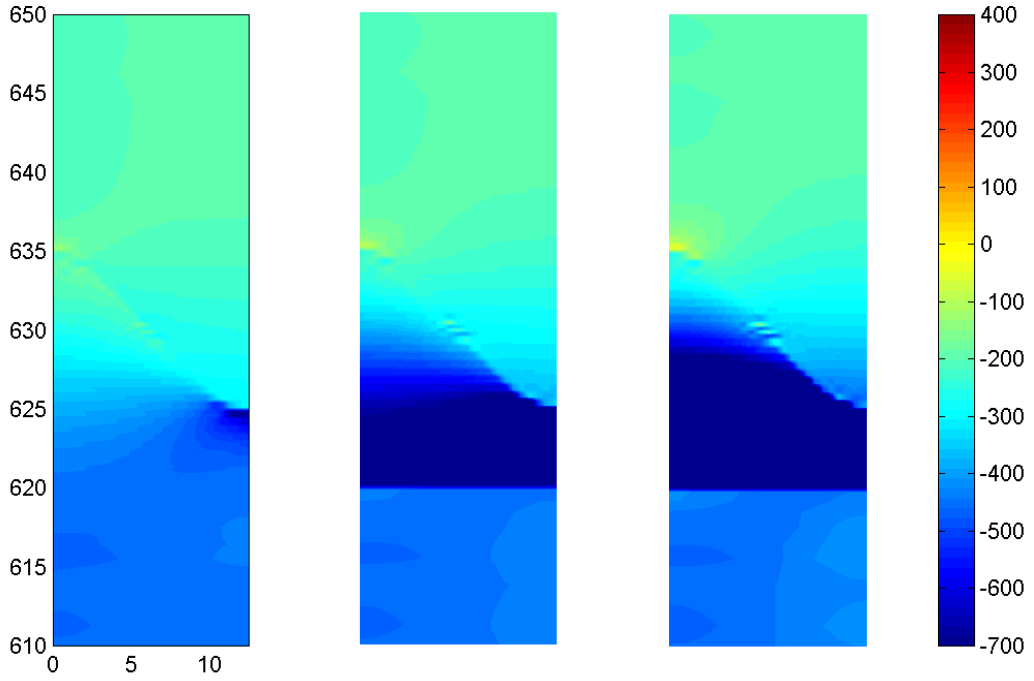

Homogeneous BC (left), 20% alumina BC (middle), 40% alumina BC (right)

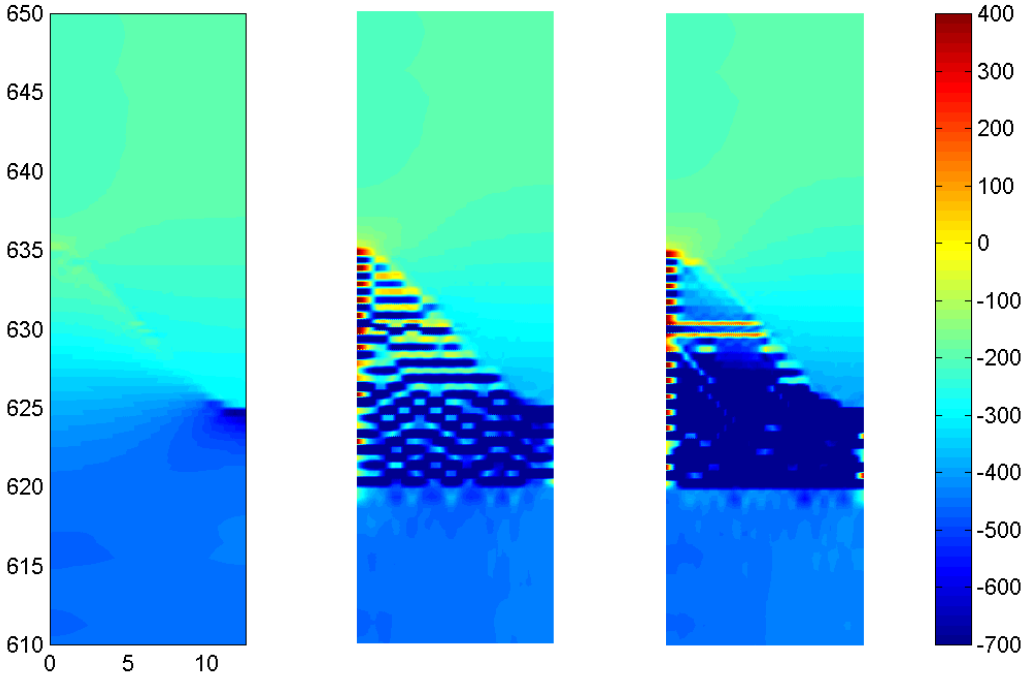

Homogeneous BC (left), 20% alumina BC (middle), 40% alumina BC (right)

Figure 9(b). Normal stress σ_{33} distributions in the interfacial region of a spatially uniform heterogeneous bond coat TBC without an oxide film, with homogenized (top) and actual (bottom) microstructures, at the end of the first thermal cycle illustrating the alumina particle content influence (colorbar scale in MPa).

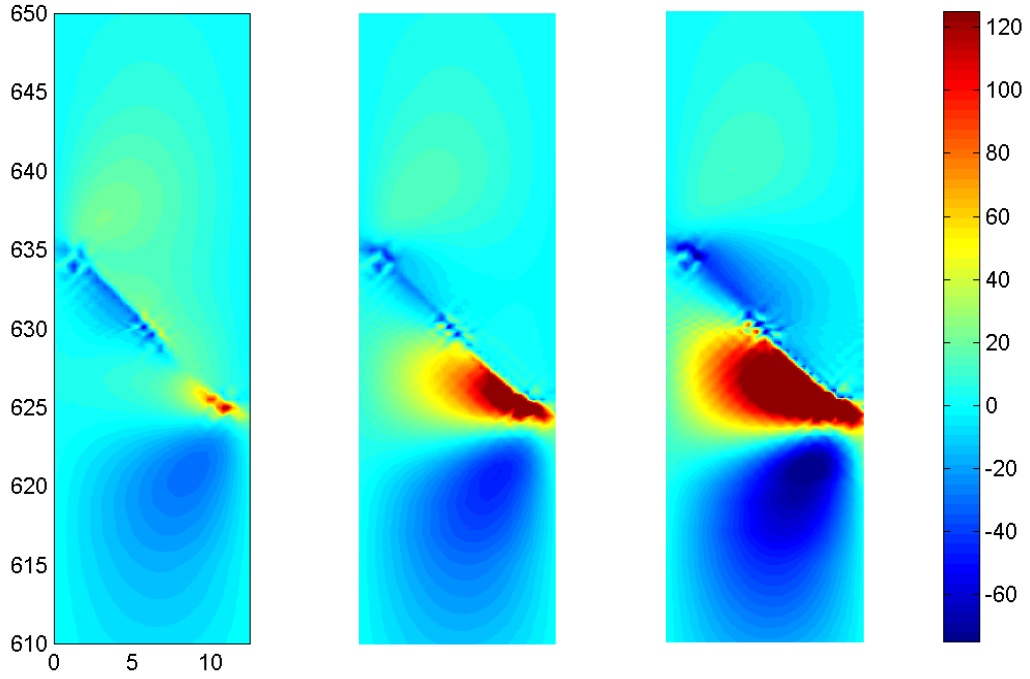

Homogeneous BC (left), 20% alumina BC (middle), 40% alumina BC (right)

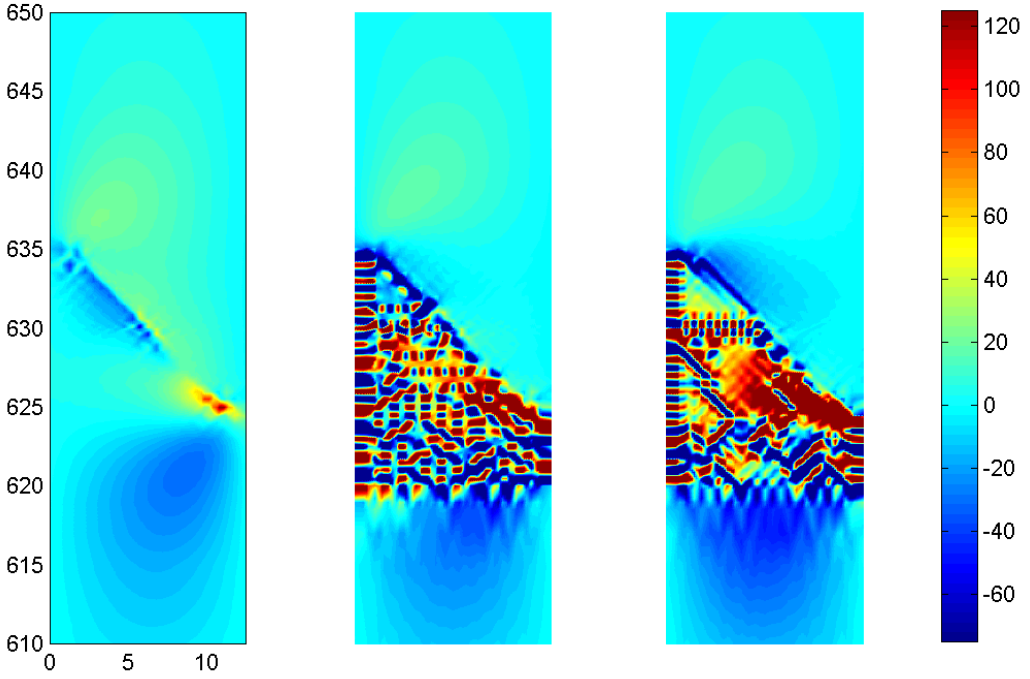

Homogeneous BC (left), 20% alumina BC (middle), 40% alumina BC (right)

Figure 9(c). Shear stress σ_{23} distributions in the interfacial region of a spatially uniform heterogeneous bond coat TBC without an oxide film, with homogenized (top) and actual (bottom) microstructures, at the end of the first thermal cycle illustrating the alumina particle content influence (colorbar scale in MPa).

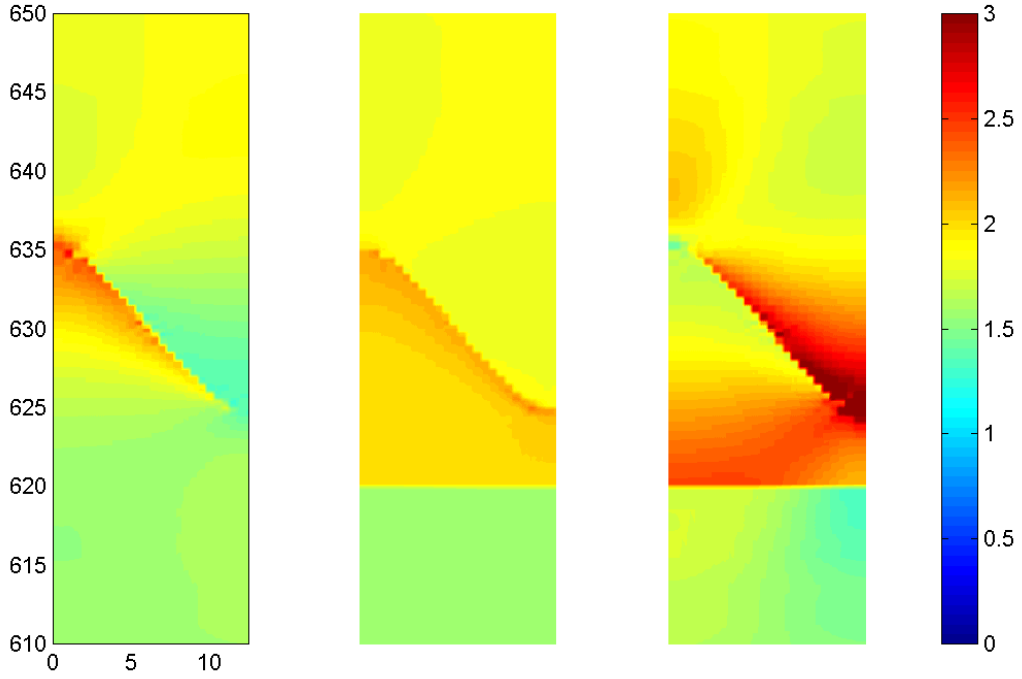

Homogeneous BC (left), 20% alumina BC (middle), 40% alumina BC (right)

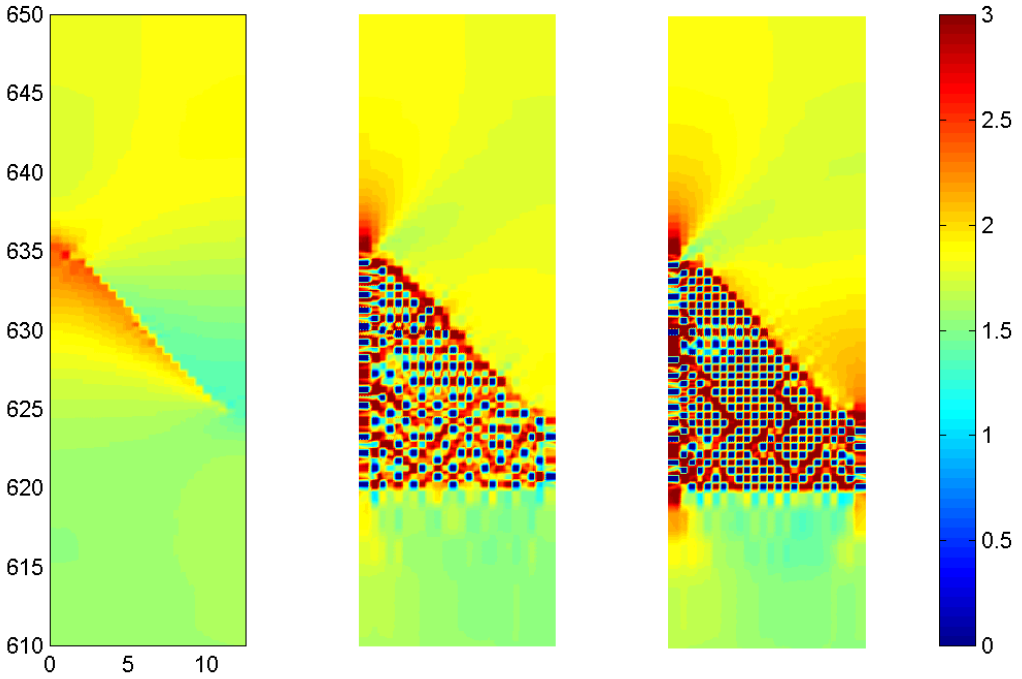

Homogeneous BC (left), 20% alumina BC (middle), 40% alumina BC (right)

Figure 9(d). Inelastic strain ε_{eff}^{int} distributions in the interfacial region of a spatially uniform heterogeneous bond coat TBC without an oxide film, with homogenized (top) and actual (bottom) microstructures, at the end of the first thermal cycle illustrating the alumina particle content influence (colorbar scale in % strain).

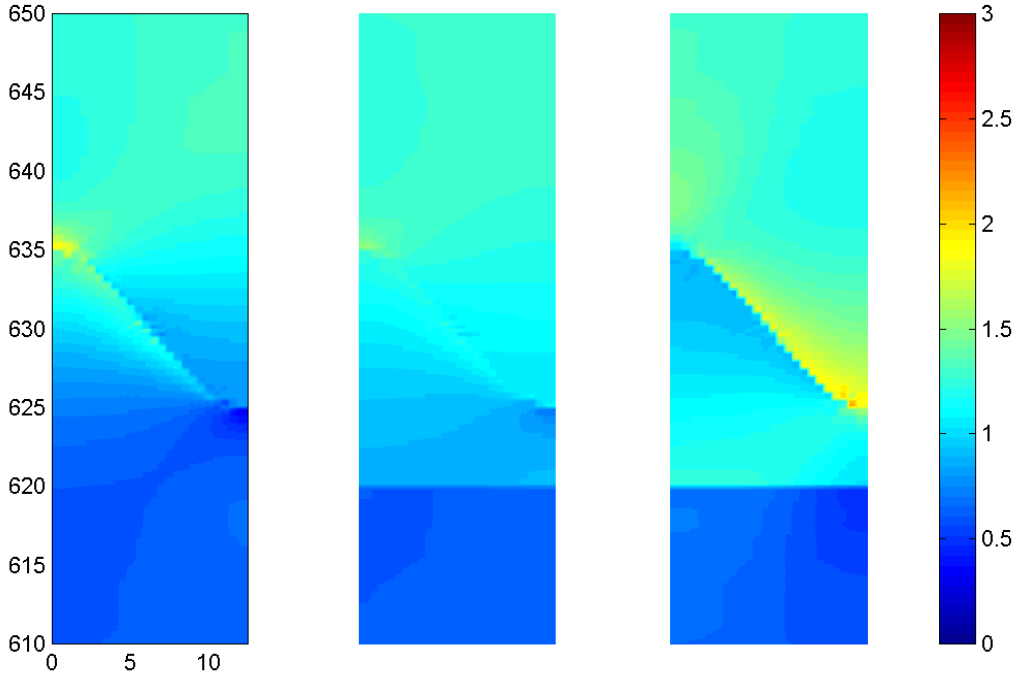

Homogeneous BC (left), 20% alumina BC (middle), 40% alumina BC (right)

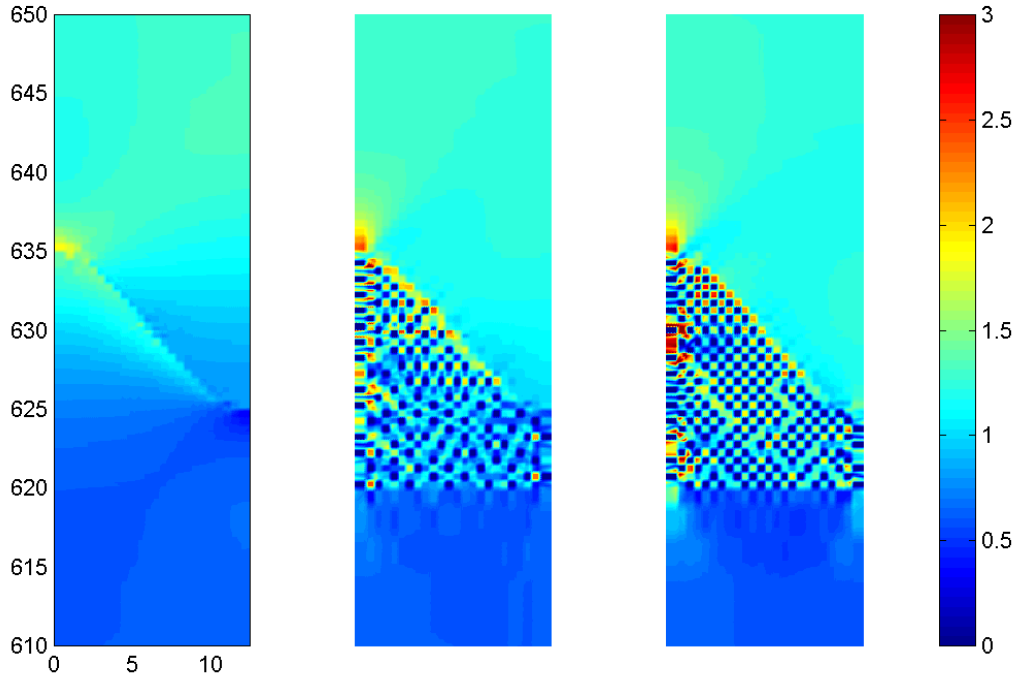

Homogeneous BC (left), 20% alumina BC (middle), 40% alumina BC (right)

Figure 9(e). Inelastic strain ε_{eff}^{res} distributions in the interfacial region of a spatially uniform heterogeneous bond coat TBC without an oxide film, with homogenized (top) and actual (bottom) microstructures, at the end of the first thermal cycle illustrating the alumina particle content influence (colorbar scale in % strain).

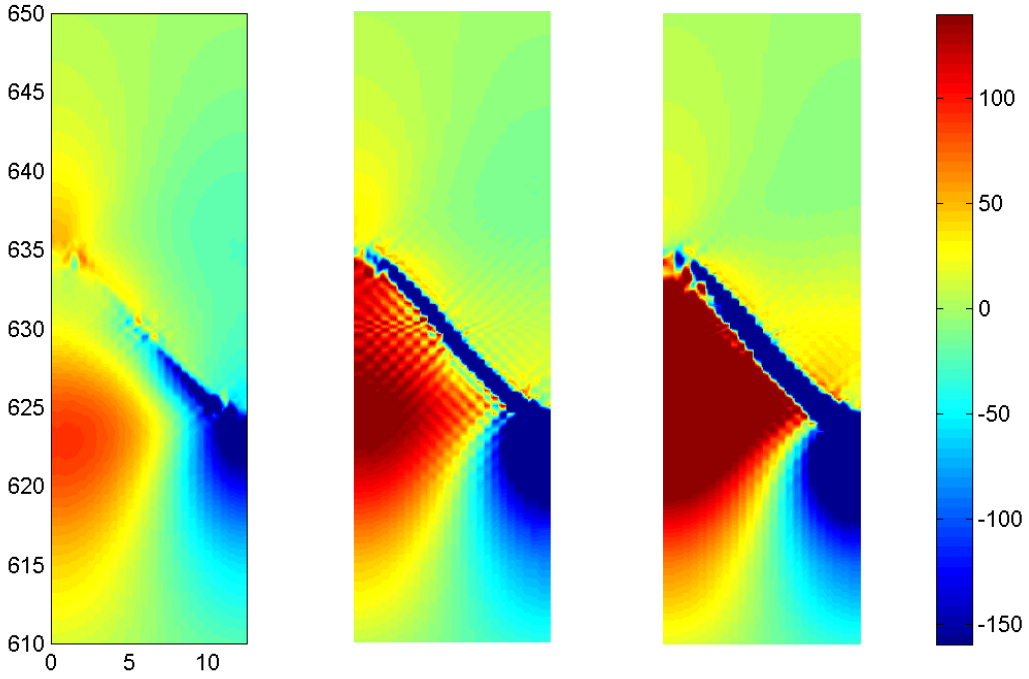

No oxide film (left), 1 micron oxide film (middle), 2 micron oxide film (right)

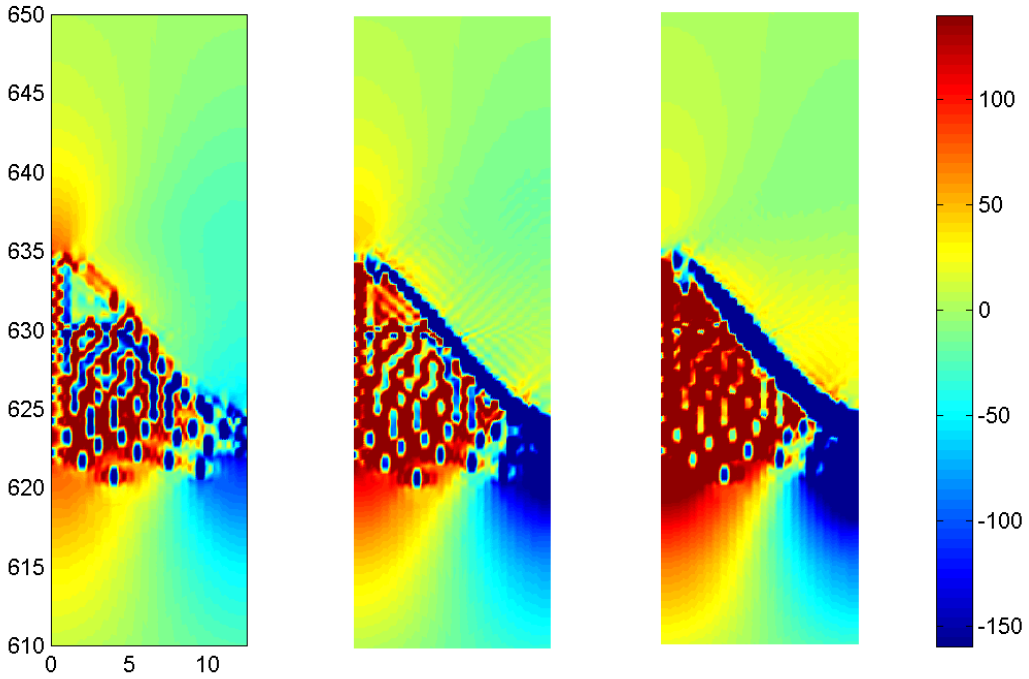

No oxide film (left), 1 micron oxide film (middle), 2 micron oxide film (right)

Figure 10(a). Normal stress σ_{22} distributions in the interfacial region of a graded bond coat TBC, with homogenized (top) and actual (bottom) microstructures, at the end of the first thermal cycle illustrating the oxide film thickness influence (colorbar scale in MPa).

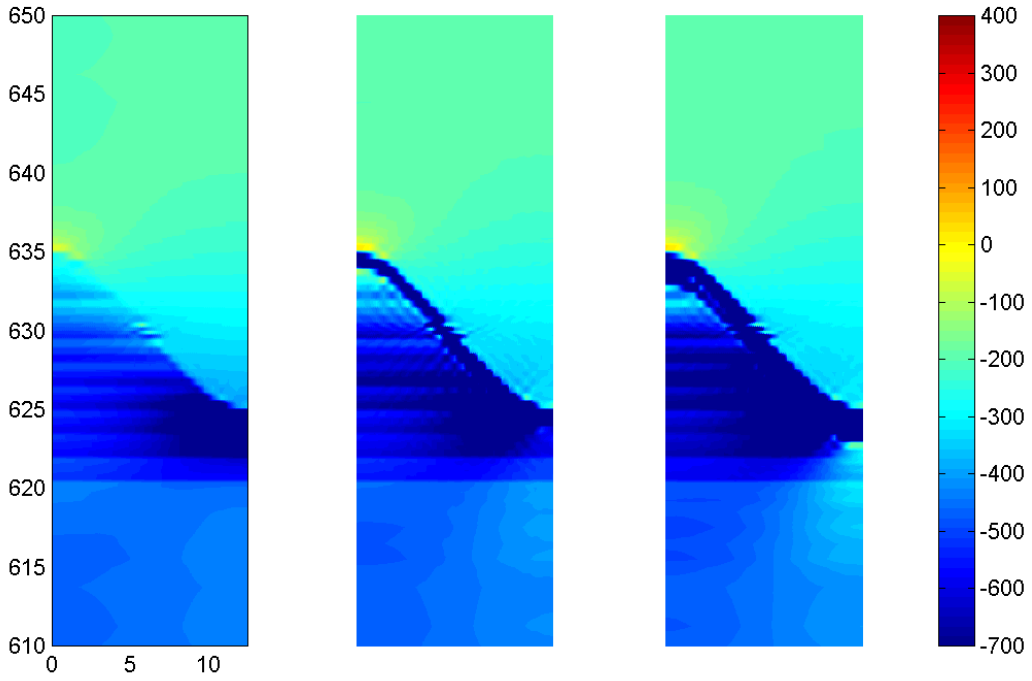

No oxide film (left), 1 micron oxide film (middle), 2 micron oxide film (right)

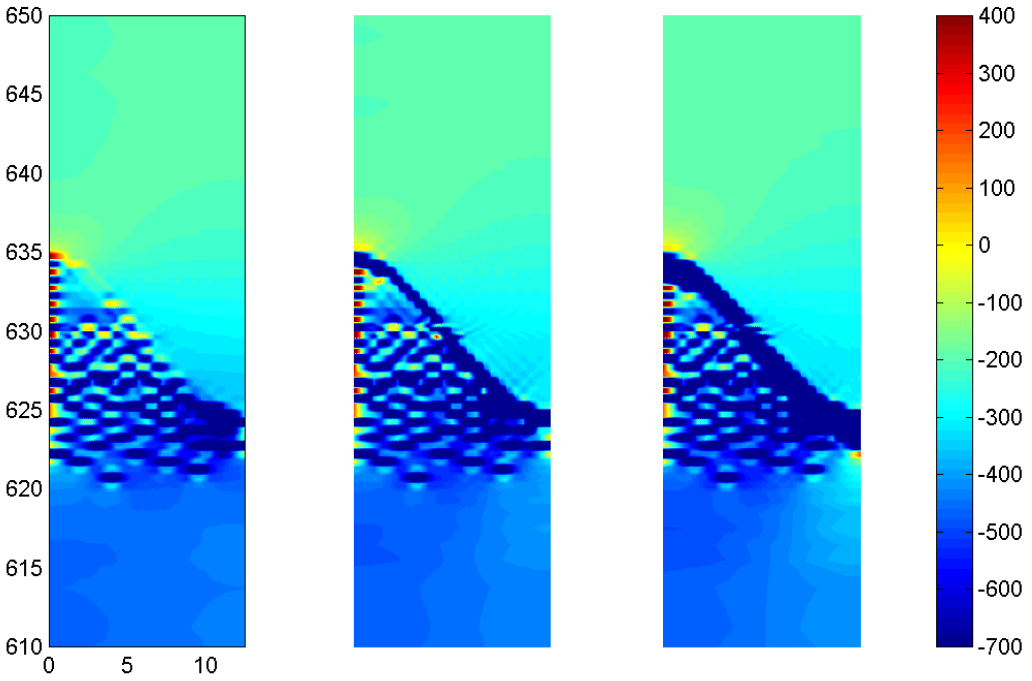

No oxide film (left), 1 micron oxide film (middle), 2 micron oxide film (right)

Figure 10(b). Normal stress σ_{33} distributions in the interfacial region of a graded bond coat TBC, with homogenized (top) and actual (bottom) microstructures, at the end of the first thermal cycle illustrating the oxide film thickness influence (colorbar scale in MPa).

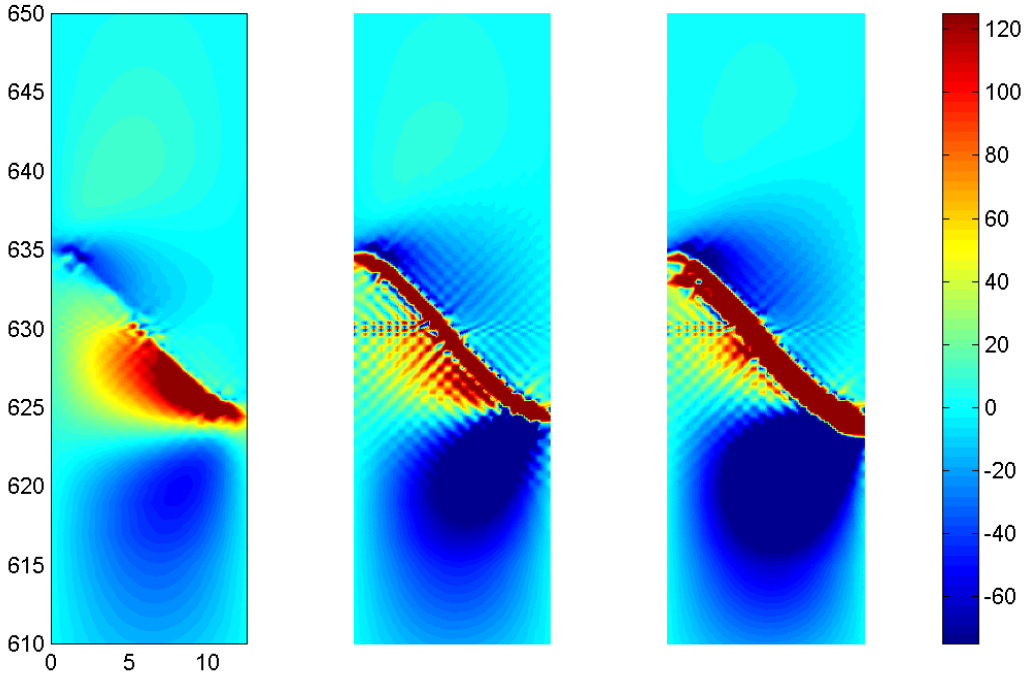

No oxide film (left), 1 micron oxide film (middle), 2 micron oxide film (right)

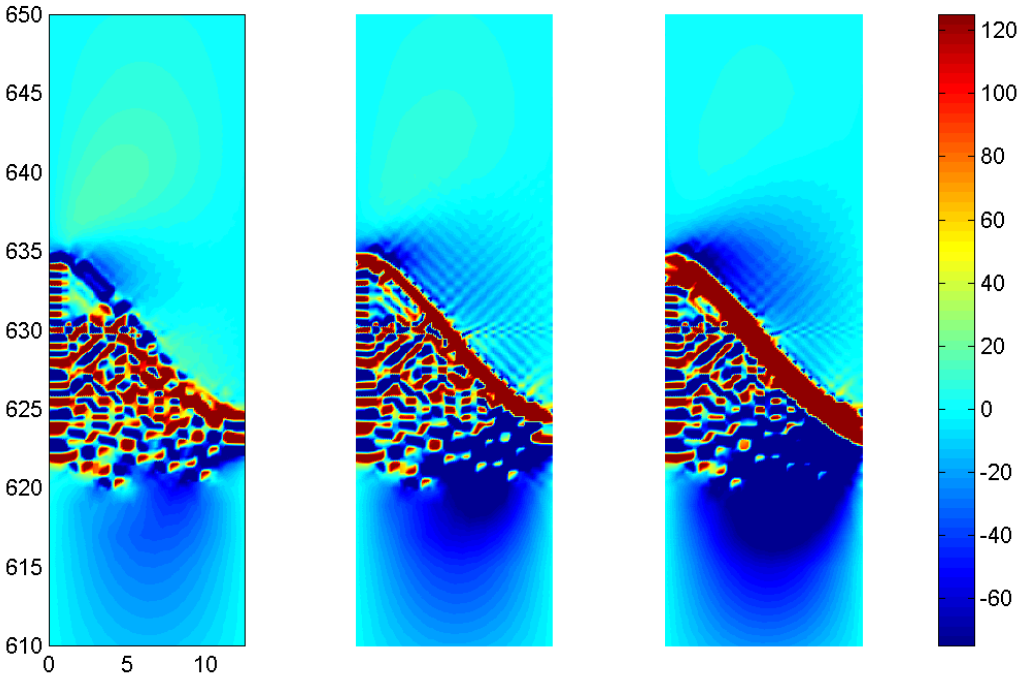

No oxide film (left), 1 micron oxide film (middle), 2 micron oxide film (right)

Figure 10(c). Shear stress σ_{23} distributions in the interfacial region of a graded bond coat TBC, with homogenized (top) and actual (bottom) microstructures, at the end of the first thermal cycle illustrating the oxide film thickness influence (colorbar scale in MPa).

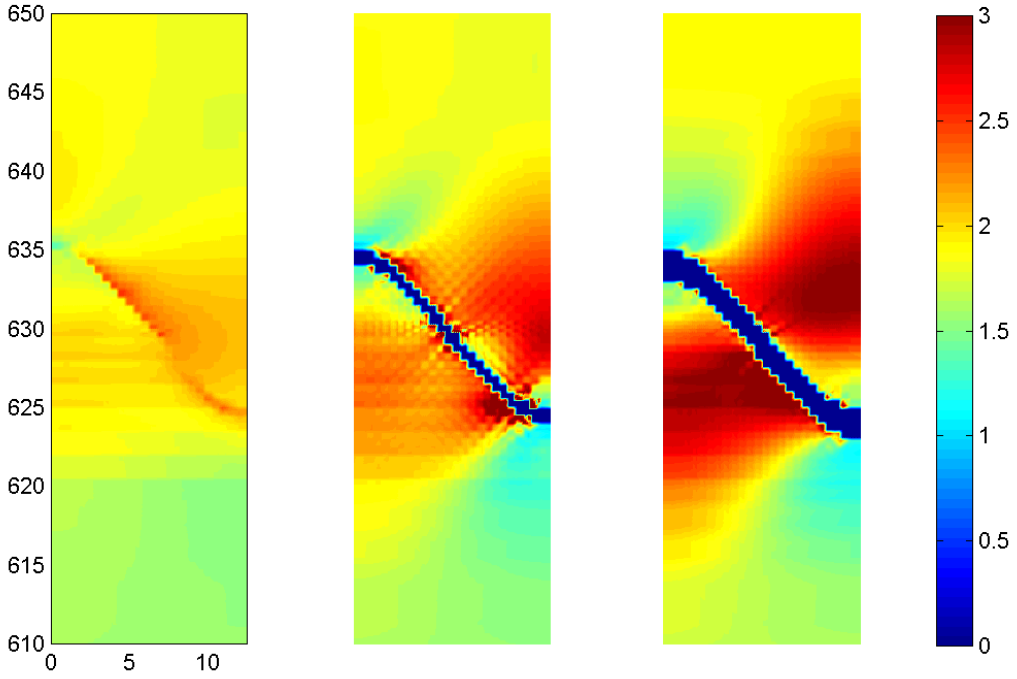

No oxide film (left), 1 micron oxide film (middle), 2 micron oxide film (right)

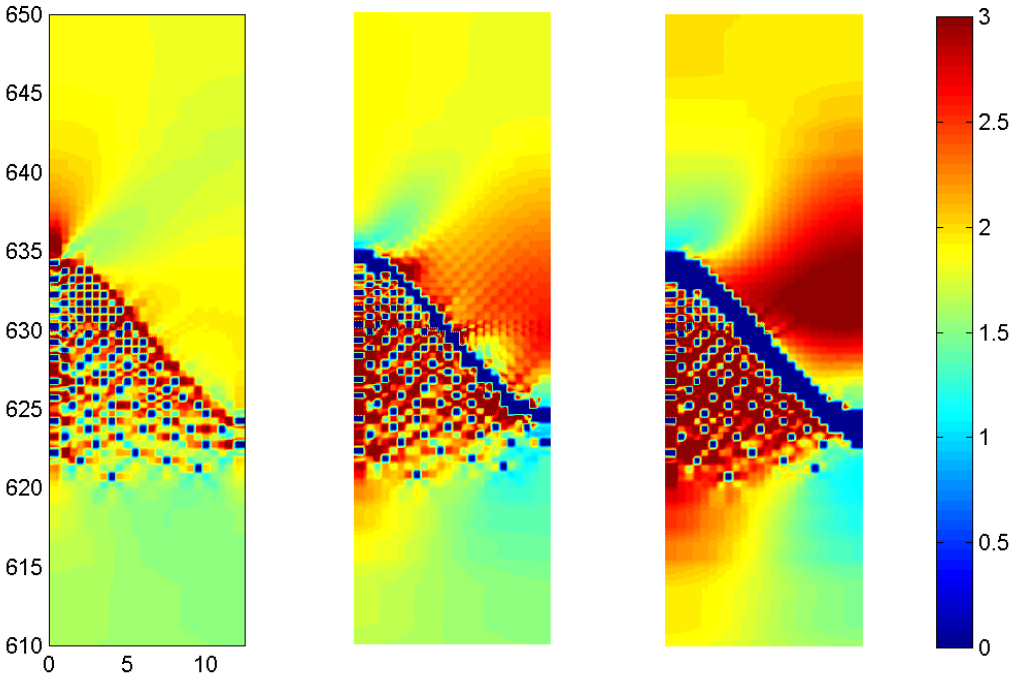

No oxide film (left), 1 micron oxide film (middle), 2 micron oxide film (right)

Figure 10(d). Inelastic strain ε_{eff}^{int} distributions in the interfacial region of a graded bond coat TBC, with homogenized (top) and actual (bottom) microstructures, at the end of the first thermal cycle illustrating the oxide film thickness influence (colorbar scale in % strain).

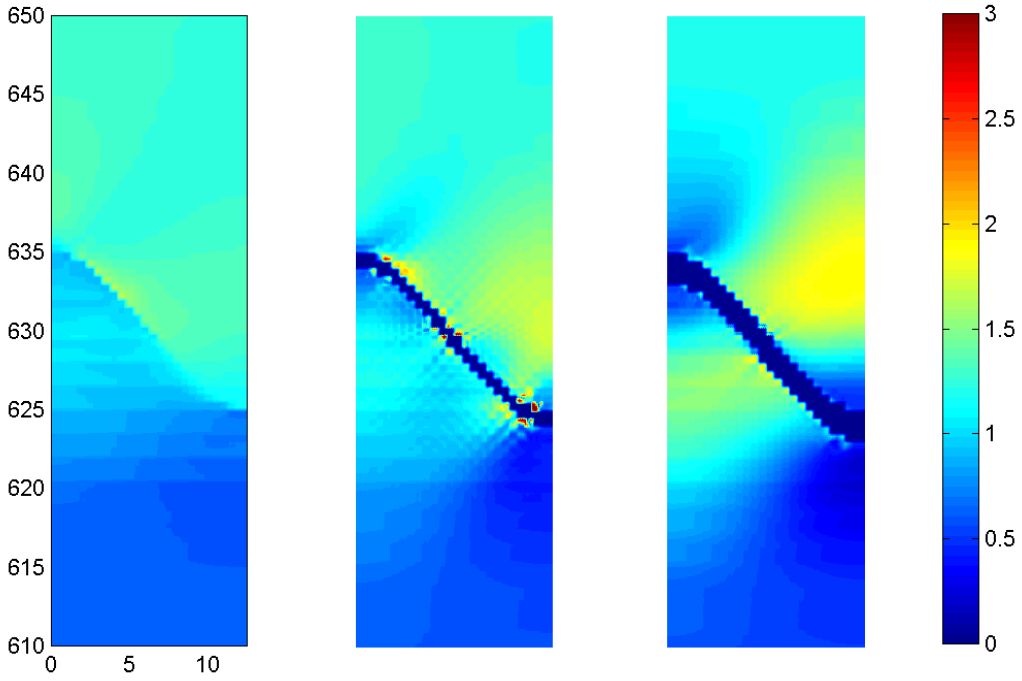

No oxide film (left), 1 micron oxide film (middle), 2 micron oxide film (right)

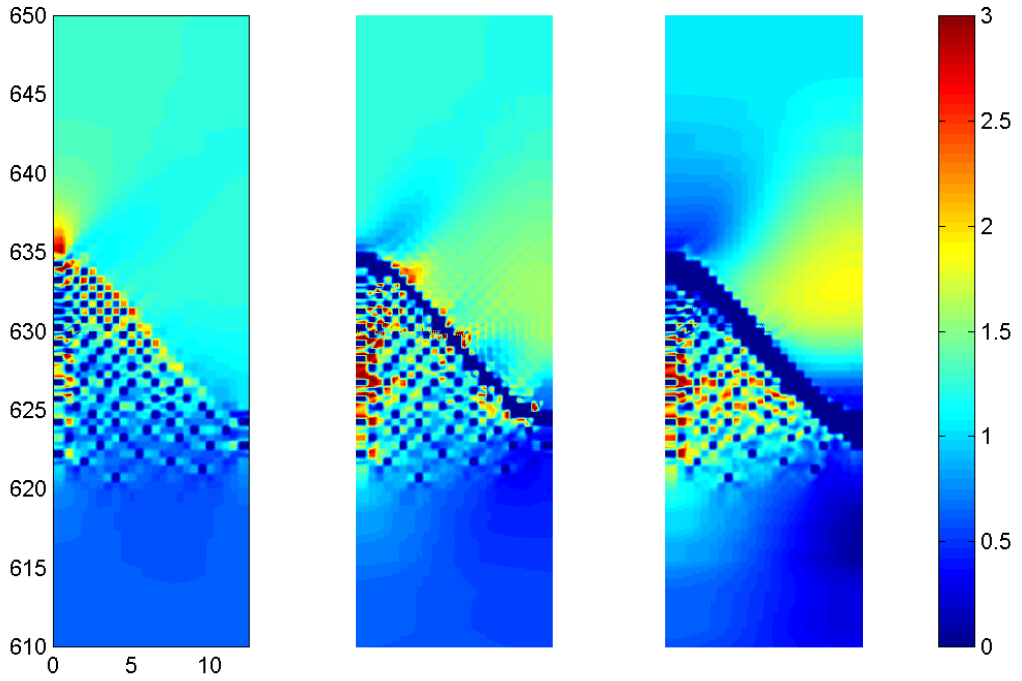

No oxide film (left), 1 micron oxide film (middle), 2 micron oxide film (right)

Figure 10(e). Inelastic strain ε_{eff}^{res} distributions in the interfacial region of a graded bond coat TBC, with homogenized (top) and actual (bottom) microstructures, at the end of the first thermal cycle illustrating the oxide film thickness influence (colorbar scale in % strain).

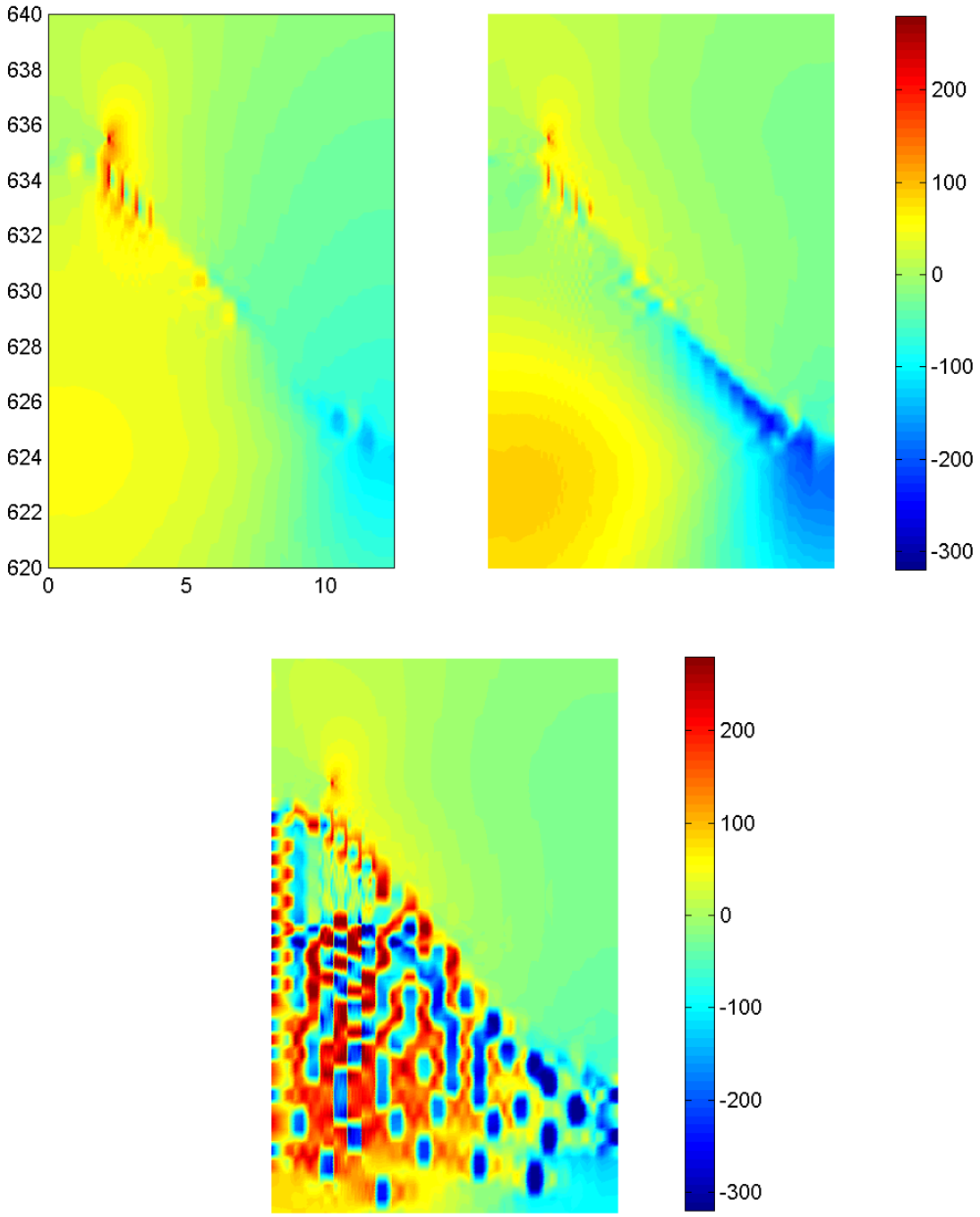

Pure bond coat TBC (top left), homogenized graded bond coat TBC (top right), actual graded bond coat TBC (bottom)

Figure 11(a). Normal stress σ_{22} distributions in the interfacial region of pure and graded bond coat TBCs without an oxide film at the end of the first cycle illustrating the effect of grading on the delamination driving forces (colorbar scale in MPa).

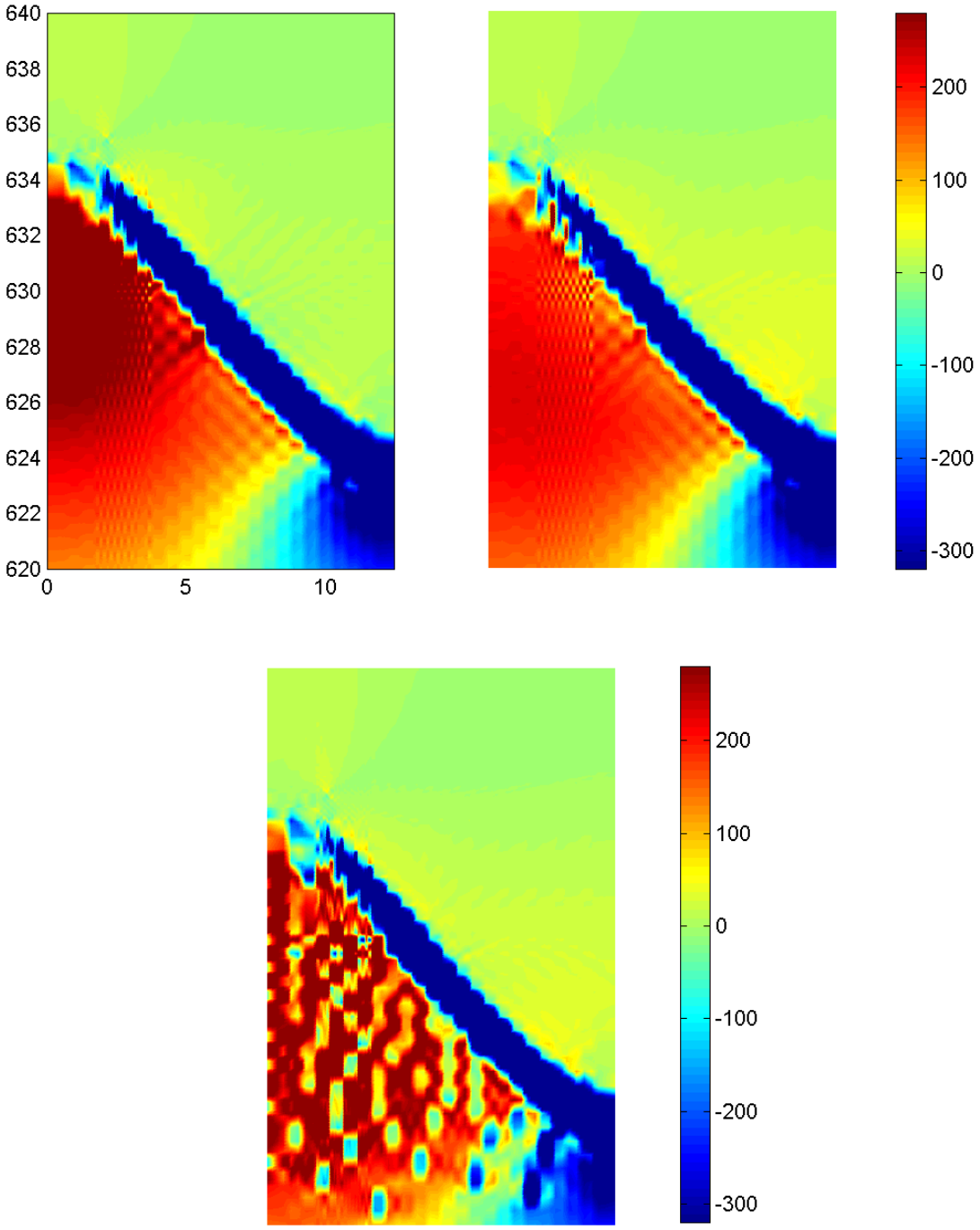

Pure bond coat TBC (top left), homogenized graded bond coat TBC (top right), actual graded bond coat TBC (bottom)

Figure 11(b). Normal stress σ_{22} distributions in the interfacial region of pure and graded bond coat TBCs with a 2 μm oxide film at the end of the first cycle, illustrating the effect of grading on the delamination driving forces (colorbar scale in MPa).

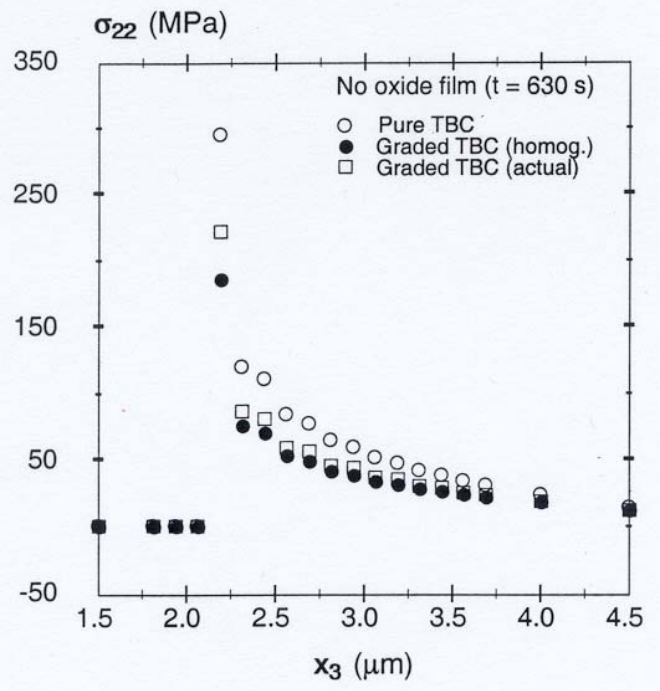

Figure 11(c). Crack-tip σ_{22} distributions along the line coincident with the crack in pure and graded TBCs without an oxide film at the end of the first cycle, illustrating the effect of grading on the delamination driving forces.

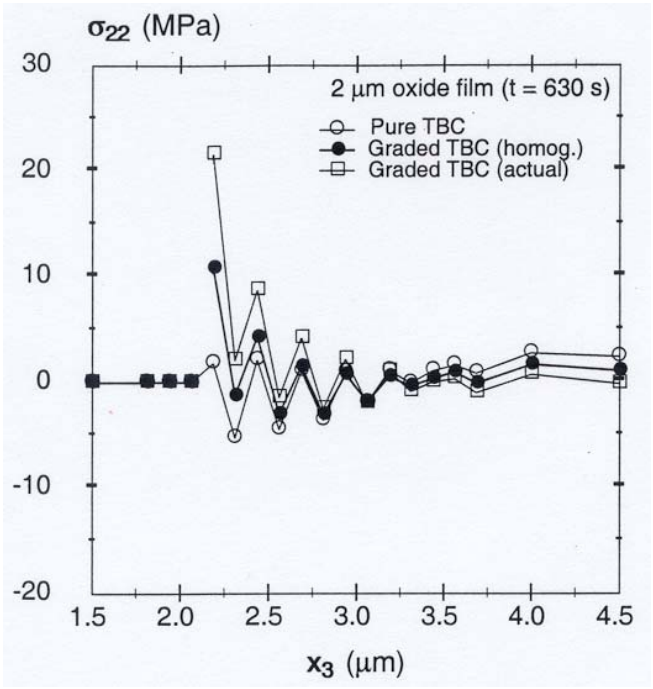

Figure 11(d). Crack-tip σ_{22} distributions along the line coincident with the crack in pure and graded TBCs with a 2 μm oxide film at the end of the first cycle, illustrating the effect of grading on the delamination driving forces.

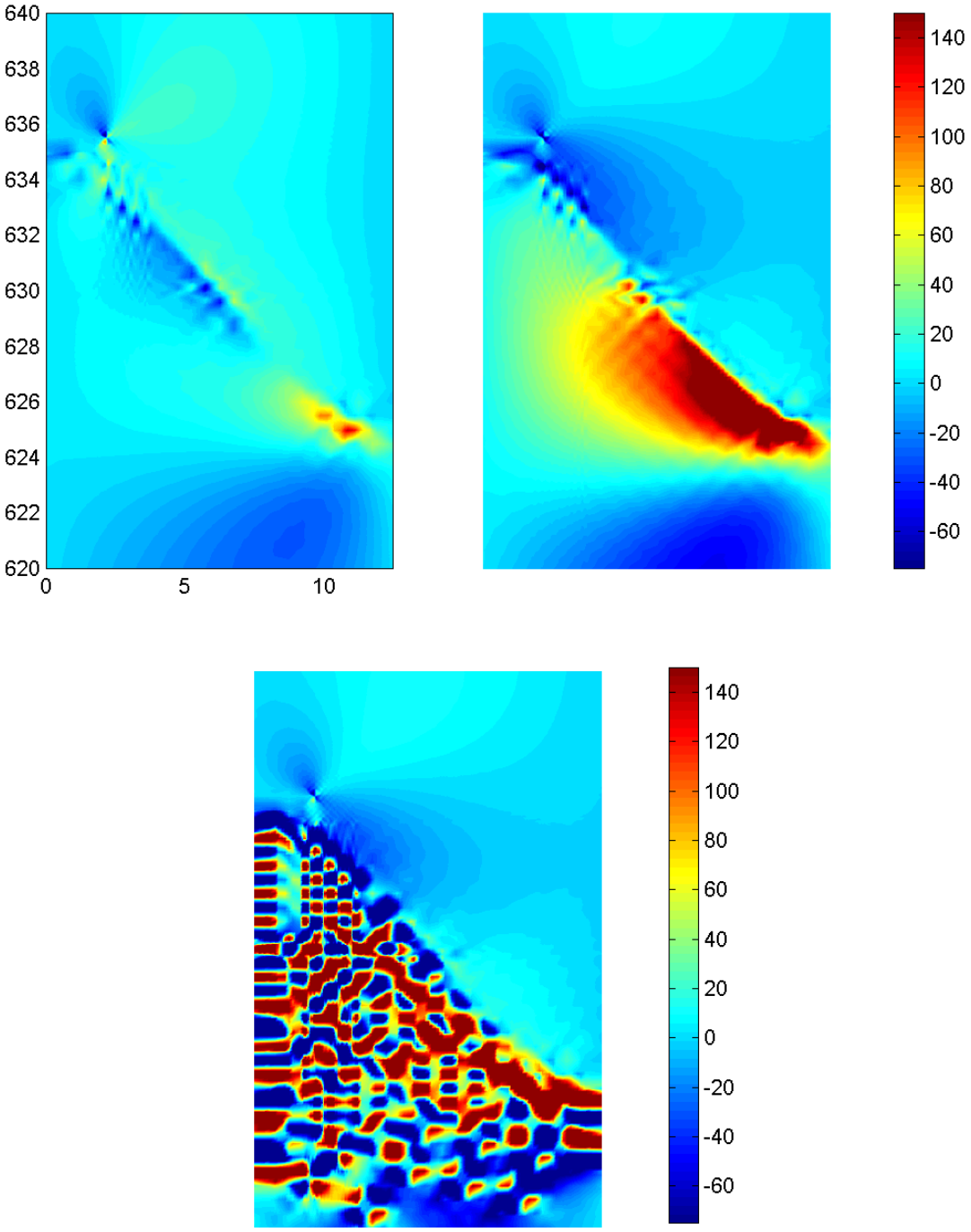

Pure bond coat TBC (top left), homogenized graded bond coat TBC (top right), actual graded bond coat TBC (bottom)

Figure 12(a). Shear stress σ_{23} distributions in the interfacial region of pure and graded bond coat TBCs without an oxide film at the end of the first cycle, illustrating the effect of grading on the delamination driving forces (colorbar scale in MPa).

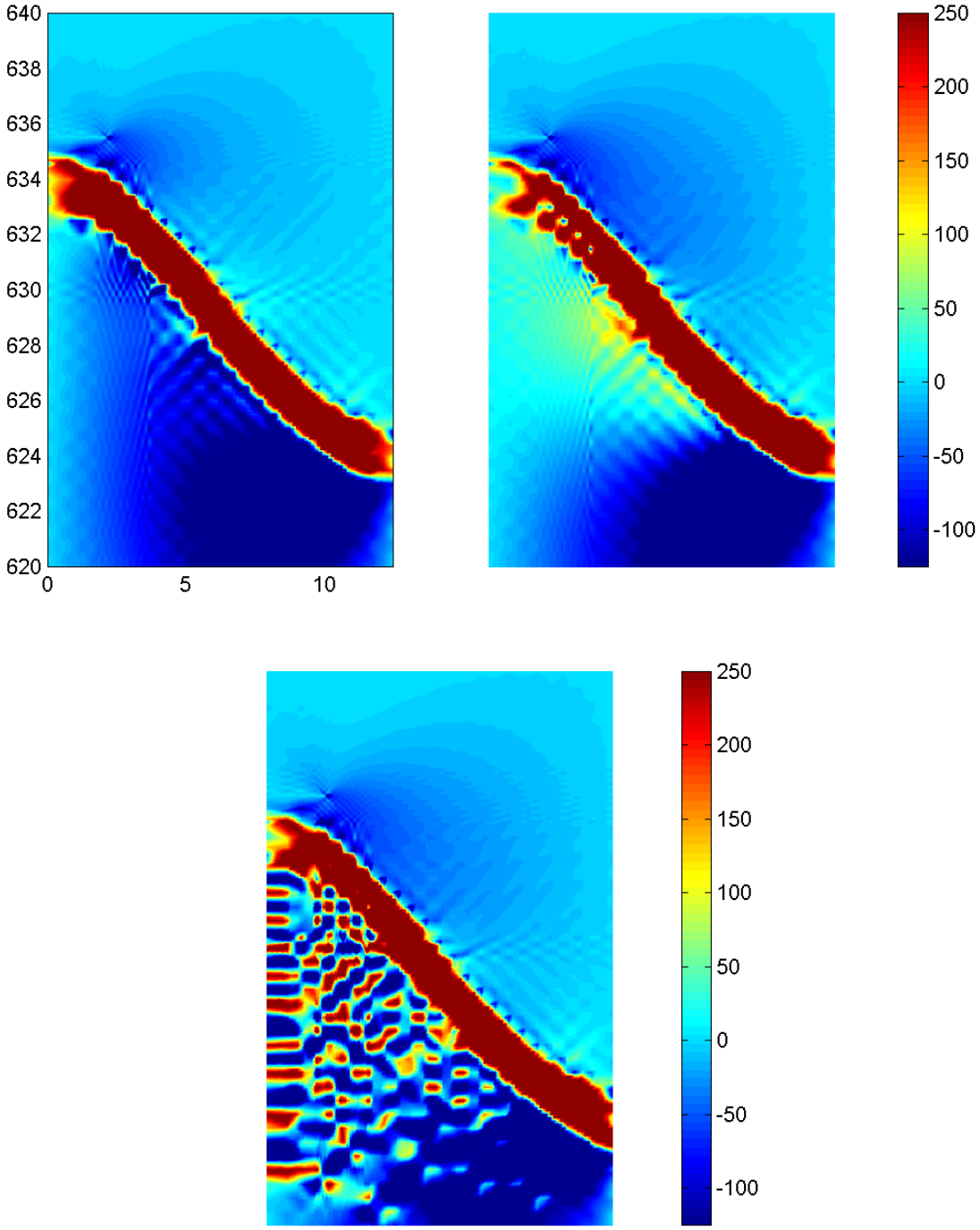

Pure bond coat TBC (top left), homogenized graded bond coat TBC (top right), actual graded bond coat TBC (bottom)

Figure 12(b). Shear stress σ_{23} distributions in the interfacial region of pure and graded bond coat TBCs with a 2 μm oxide film at the end of the first cycle, illustrating the effect of grading on the delamination driving forces (colorbar scale in MPa).

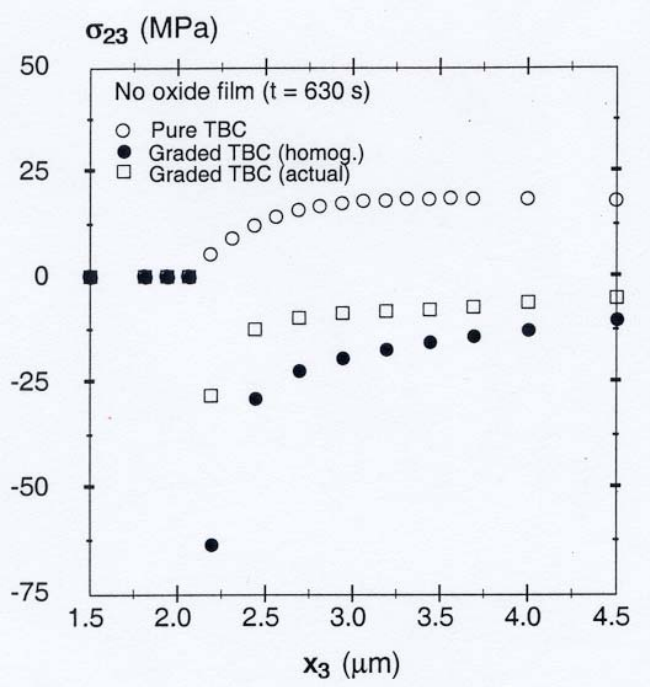

Figure 12(c). Crack-tip σ_{23} distributions along the line coincident with the crack in pure and graded TBCs without an oxide film at the end of the first cycle, illustrating the effect of grading on the delamination driving forces.

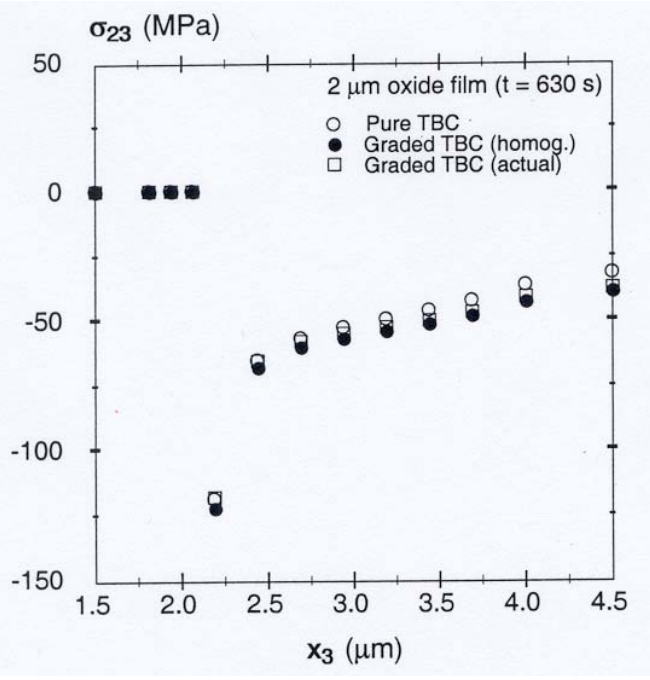

Figure 12(d). Crack-tip σ_{23} distributions along the line coincident with the crack in pure and graded TBCs with a 2 μm oxide film at the end of the first cycle, illustrating the effect of grading on the delamination driving forces.

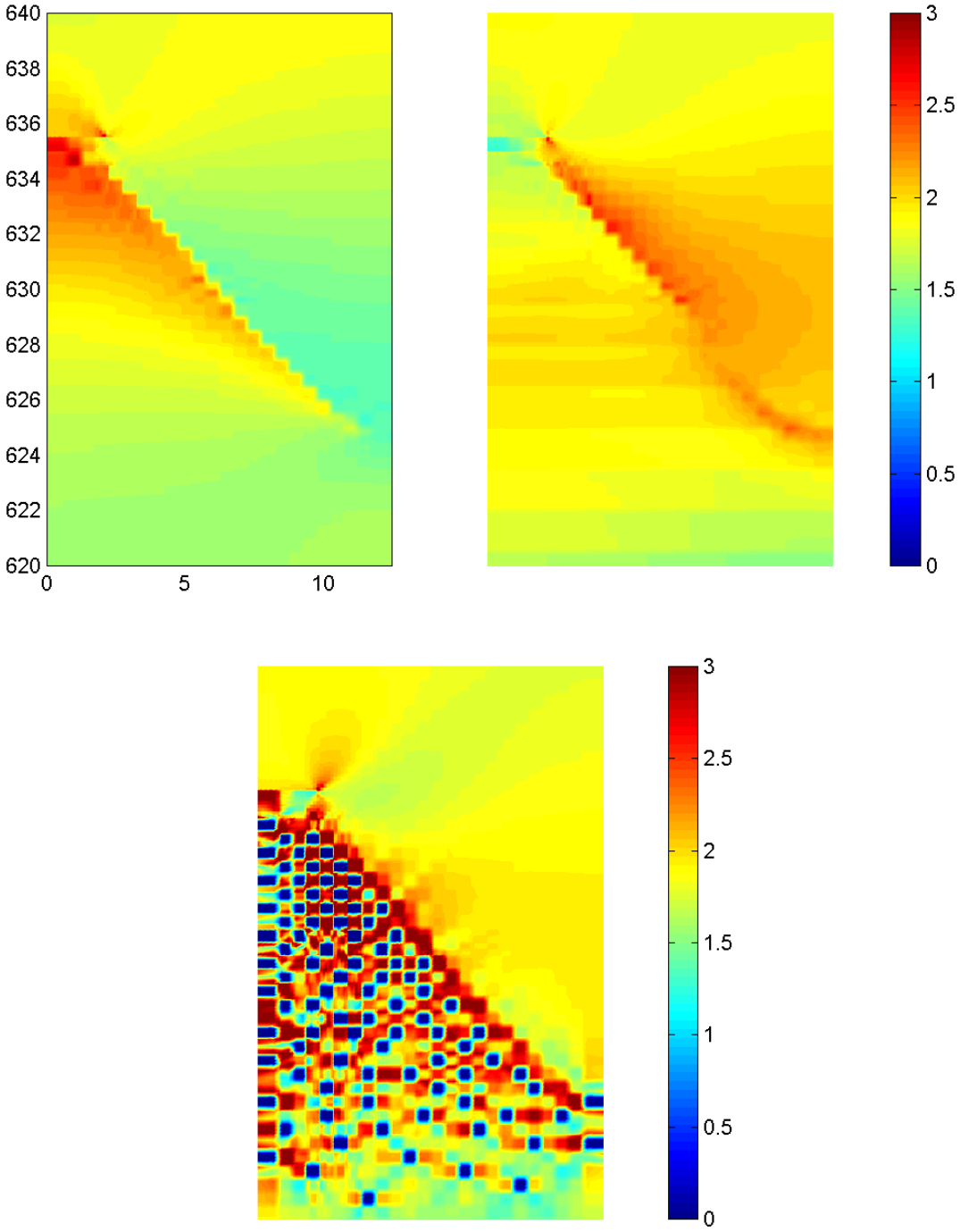

Pure bond coat TBC (top left), homogenized graded bond coat TBC (top right), actual graded bond coat TBC (bottom)

Figure 13(a). Inelastic strain ε_{eff}^{int} distributions in the interfacial region of pure and graded bond coat TBCs without an oxide film at the end of the first cycle illustrating the effect of grading on the crack-tip inelastic strain field (colorbar scale in % strain).

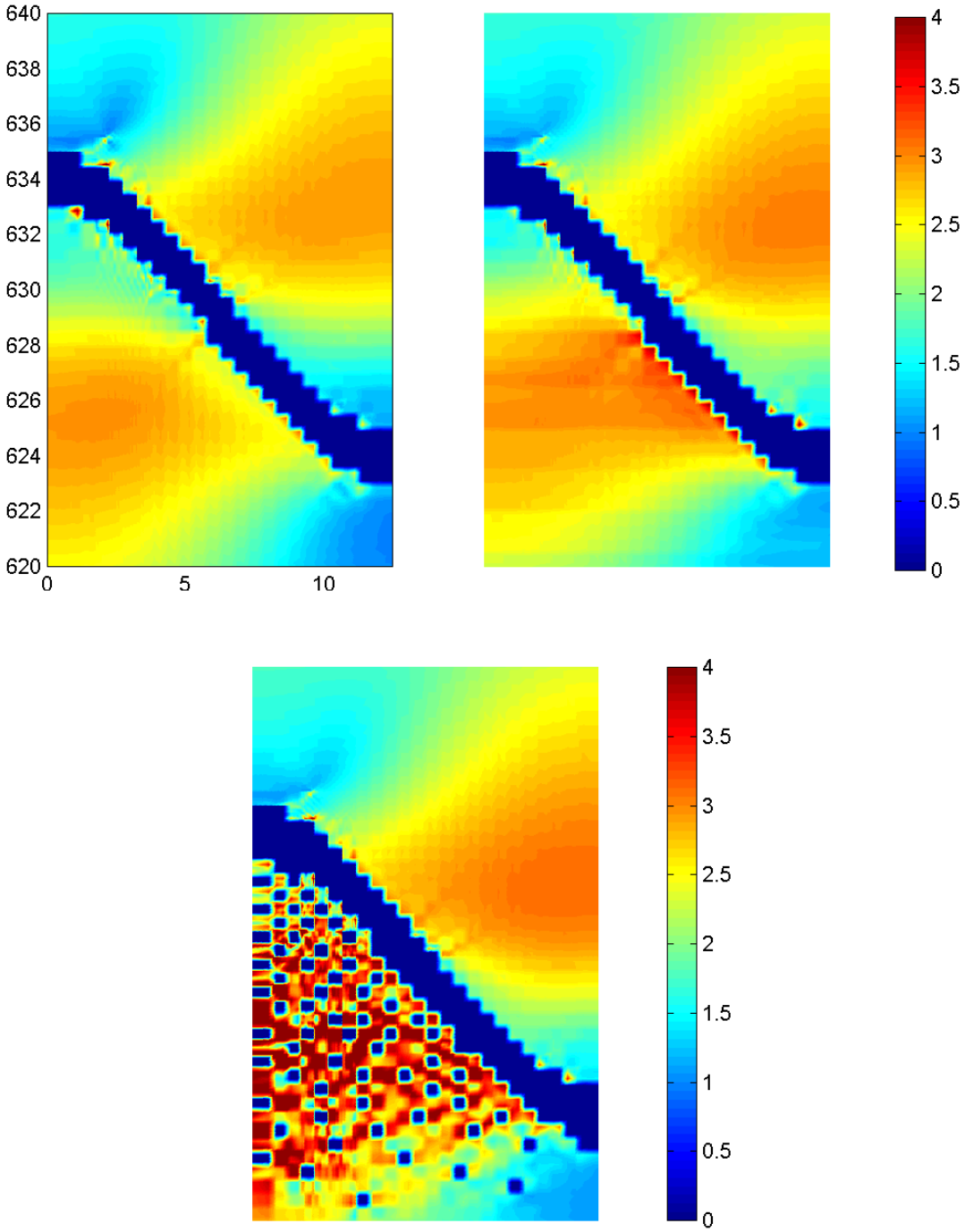

Pure bond coat TBC (top left), homogenized graded bond coat TBC (top right), actual graded bond coat TBC (bottom)

Figure 13(b). Inelastic strain ε_{eff}^{int} distributions in the interfacial region of pure and graded bond coat TBCs with a 2 μm oxide film at the end of the first cycle, illustrating the effect of grading on the crack-tip inelastic strain field (colorbar scale in % strain).

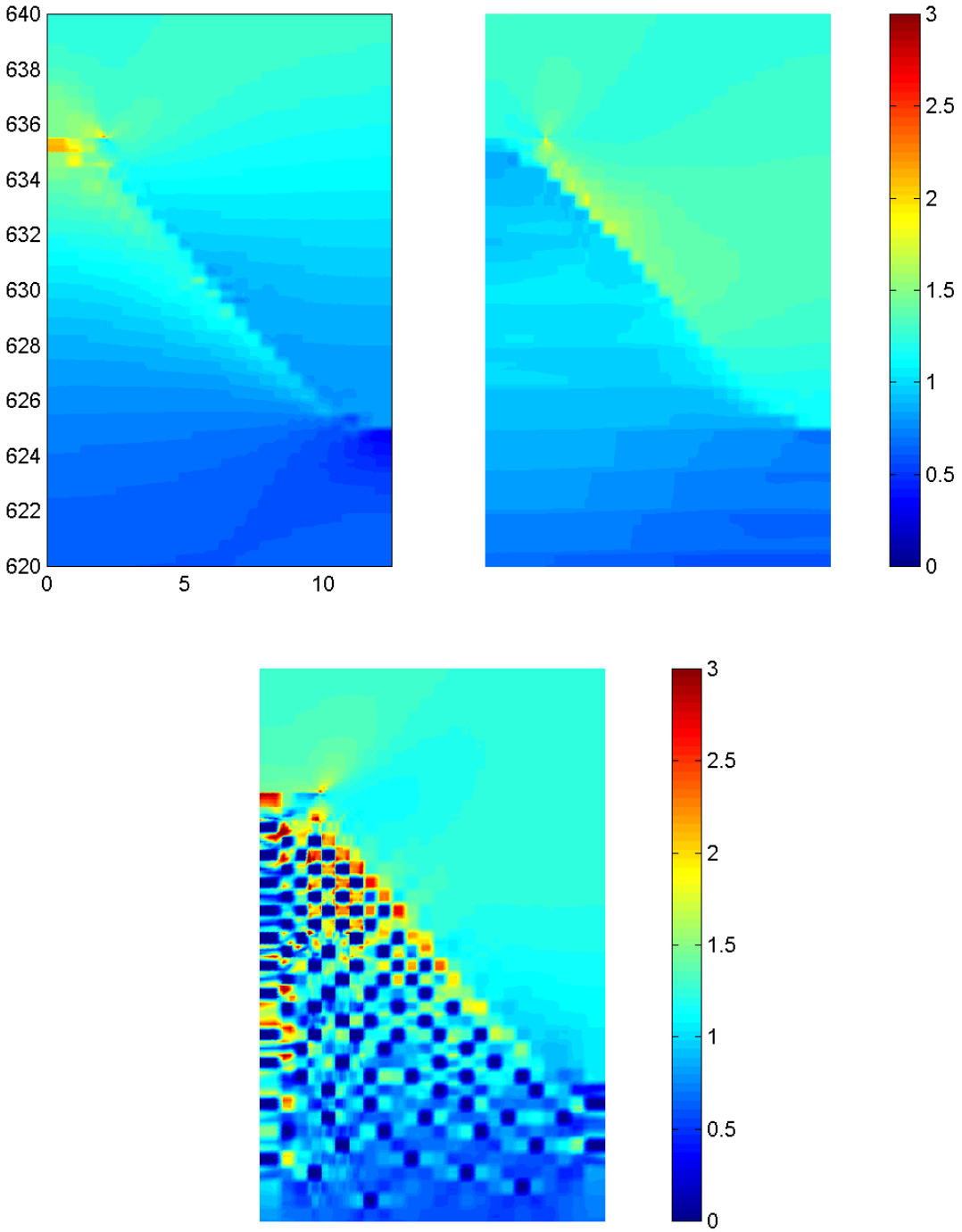

Pure bond coat TBC (top left), homogenized graded bond coat TBC (top right), actual graded bond coat TBC (bottom)

Figure 14(a). Inelastic strain ε_{eff}^{res} distributions in the interfacial region of pure and graded bond coat TBCs without an oxide film at the end of the first cycle, illustrating the effect of grading on the crack-tip inelastic strain field (colorbar scale in % strain).

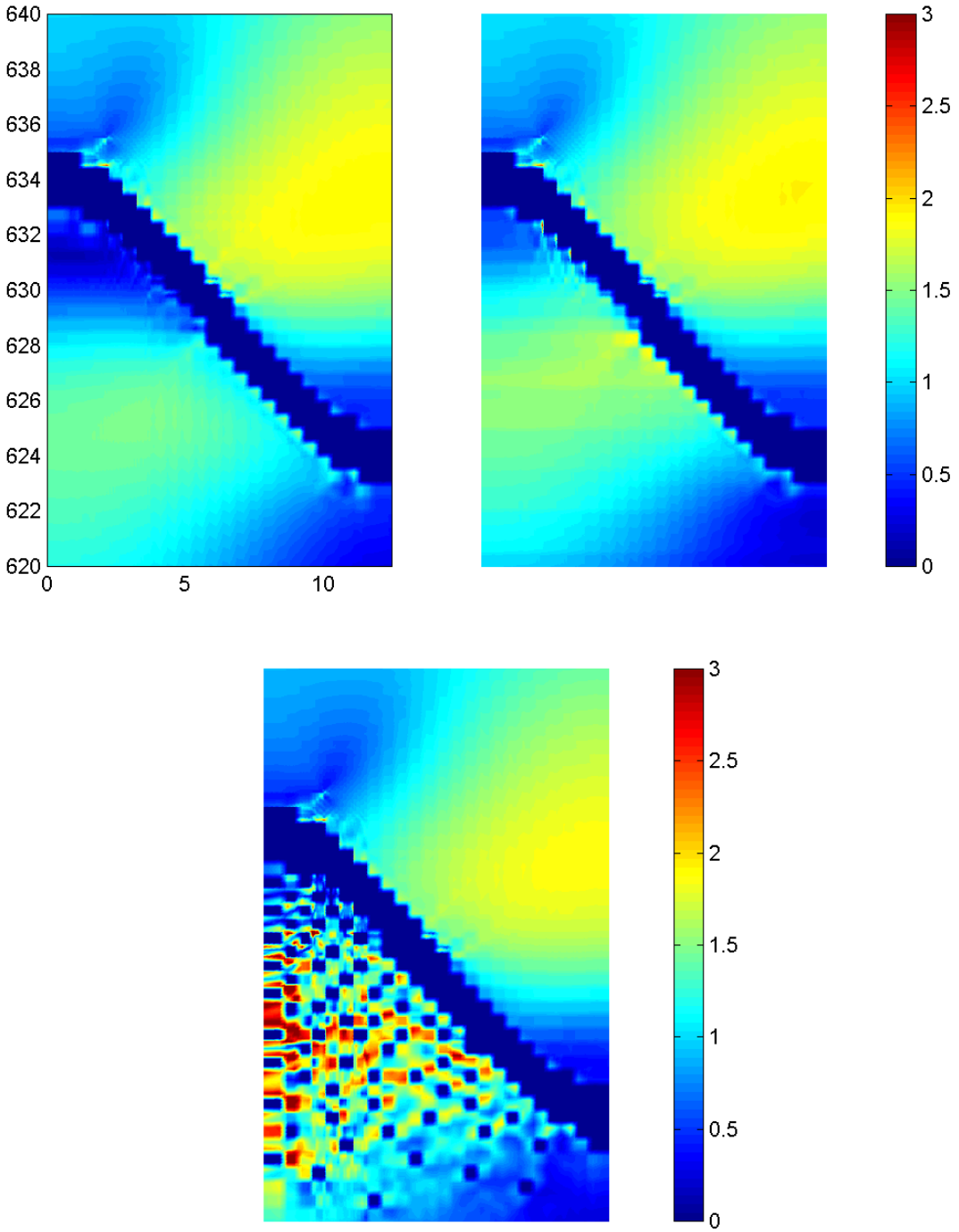

Pure bond coat TBC (top left), homogenized graded bond coat TBC (top right), actual graded bond coat TBC (bottom)

Figure 14(b). Inelastic strain ε_{eff}^{res} distributions in the interfacial region of pure and graded bond coat TBCs with a 2 μm oxide film at the end of the first cycle illustrating the effect of grading on the crack-tip inelastic strain field (colorbar scale in % strain).

REPORT DOCUMENTATION PAGE

Form Approved
OMB No. 0704-0188

1. AGENCY USE ONLY (*Leave blank*)	2. REPORT DATE	3. REPORT TYPE AND DATES COVERED
	December 2003	Technical Memorandum

4. TITLE AND SUBTITLE

Analysis of Plasma-Sprayed Thermal Barrier Coatings With Homogeneous and Heterogeneous Bond Coats Under Spatially Uniform Cyclic Thermal Loading

5. FUNDING NUMBERS

WBS–22–708–31–13

6. AUTHOR(S)

Marek-Jerzy Pindera, Jacob Aboudi, and Steven M. Arnold

7. PERFORMING ORGANIZATION NAME(S) AND ADDRESS(ES)

National Aeronautics and Space Administration
John H. Glenn Research Center at Lewis Field
Cleveland, Ohio 44135–3191

8. PERFORMING ORGANIZATION REPORT NUMBER

E–12700

9. SPONSORING/MONITORING AGENCY NAME(S) AND ADDRESS(ES)

National Aeronautics and Space Administration
Washington, DC 20546–0001

10. SPONSORING/MONITORING AGENCY REPORT NUMBER

NASA TM—2003-210803

11. SUPPLEMENTARY NOTES

Marek-Jerzy Pindera, University of Virginia, Charlottesville, Virginia 22904; Jacob Aboudi, Tel-Aviv University, Ramat-Aviv 69978, Israel; and Steven M. Arnold, NASA Glenn Research Center. Responsible person, Steven M. Arnold, organization code 5920, 216–433–3334.

12a. DISTRIBUTION/AVAILABILITY STATEMENT

Unclassified - Unlimited
Subject Categories: 24 and 26 Distribution: Nonstandard

Available electronically at http://gltrs.grc.nasa.gov

This publication is available from the NASA Center for AeroSpace Information, 301–621–0390.

12b. DISTRIBUTION CODE

13. ABSTRACT ***(Maximum 200 words)***

This report summarizes the results of a numerical investigation into the spallation mechanism in plasma-sprayed thermal barrier coatings observed under spatially-uniform cyclic thermal loading. The analysis focuses on the evolution of local stress and inelastic strain fields in the vicinity of the rough top/bond coat interface during thermal cycling, and how these fields are influenced by the presence of an oxide film and spatially uniform and graded distributions of alumina particles in the metallic bond coat aimed at reducing the top/bond coat thermal expansion mismatch. The impact of these factors on the potential growth of a local horizontal delamination at the rough interface's crest is included. The analysis is conducted using the Higher-Order Theory for Functionally Graded Materials with creep/relaxation constituent modeling capabilities. For two-phase bond coat microstructures, both the actual and homogenized properties are employed in the analysis. The results reveal the important contributions of both the normal and shear stress components to the delamination growth potential in the presence of an oxide film, and suggest mixed-mode crack propagation. The use of bond coats with uniform or graded microstructures is shown to increase the potential for delamination growth by increasing the magnitude of the crack-tip shear stress component.

14. SUBJECT TERMS

Micromechanics; Elastic; Inelastic; Deformation; Thermal barrier coating; Failure; Functionally graded material; Crack growth

15. NUMBER OF PAGES

68

16. PRICE CODE

17. SECURITY CLASSIFICATION OF REPORT	18. SECURITY CLASSIFICATION OF THIS PAGE	19. SECURITY CLASSIFICATION OF ABSTRACT	20. LIMITATION OF ABSTRACT
Unclassified	Unclassified	Unclassified	